Title
Investigation of the interior of Mercury through the study of its gravity, topography, and tidal response

Author
Padovan, Sebastiano

Publication Date
2014

Peer reviewed|Thesis/dissertation

University of California

Los Angeles

Investigation of the interior of Mercury through the study of its gravity, topography, and tidal response

A dissertation submitted in partial satisfaction

of the requirements for the degree

Doctor of Philosophy in Geophysics and Space Physics

by

Sebastiano Padovan

2015

Abstract of the Dissertation

Investigation of the interior of Mercury through the study of its gravity, topography, and tidal response

by

Sebastiano Padovan

Doctor of Philosophy in Geophysics and Space Physics

University of California, Los Angeles, 2015

Professor Jean-Luc Margot, Chair

With the goal of furthering our understanding of the interior structure of Mercury, this work tries to answer the following two questions. What can the response of the planet to solar tides reveal about the interior structure? What is the thickness of the crust and what are the implications for the interior? By comparing the models developed here for the tidal response of Mercury with the response measured by the MErcury Surface Space ENvironment GEochemistry and Ranging spacecraft (MESSENGER), the rheology of the mantle of the innermost planet is investigated. The measured tidal deformation indicates that, unless the rigidity of mantle materials is unexpectedly high, the mantle is relatively cold. Geochemical arguments based on the composition of the surface of Mercury as measured by MESSENGER have been used to put forward the hypothesis of the existence of a solid FeS layer at the bottom of the mantle. The tidal modeling indicates that the presence of the FeS layer is unlikely. To further constrain the interior structure of Mercury the thickness of the crust is calculated by computing geoid-to-topography ratios over the surface of the planet. The inferred crustal

thickness, 35 ± 18 km, has three interesting implications. First, this relatively thin crust allows for the possibility that basin-forming events excavated mantle material from Mercury's mantle. If this material is still exposed on the surface it can potentially be observed by instruments onboard MESSENGER and future missions at Mercury. Second, the volume of silicate materials present in the crust of Mercury represents about 10% of the total silicate materials in the planet, the largest value among the terrestrial planets. This implies that Mercury had the highest efficiency of crustal production. Finally, by combining the estimate of the crustal thickness with the measured abundances of heat-producing elements on the surface of Mercury a lower bound can be placed on the amount of heat production in the mantle at a time following the accretion and differentiation of the planet, approximately 4.45 Ga ago. This information is useful for future models of the thermochemical evolution of the innermost planet.

The dissertation of Sebastiano Padovan is approved.

Michael Jura

Gerald Schubert

Jean-Luc Margot, Committee Chair

University of California, Los Angeles

2015

To Marianna and our ongoing
journey in space and time

Table of Contents

List of Figures

List of Tables

Acknowledgments

This dissertation is the result of a number of years during which I had the luck to interact with a number of people that widened my perspective on science and the world. My advisor Jean-Luc Margot had the patience to let me choose my own path and was supportive all the time, even when the path was rough. He could definitely see farther than me. From my first year at UCLA on many occasions the (now) members of my committee, Michael Jura, Jonathan Mitchell, and Gerald Schubert, through their classes, comments, questions, and in general their approach to science, were a source of extremely stimulating thoughts, which sometimes led to sleepless night hours. For similar reasons I want to thank William Newman, Jon Aurnou, and Abby Kavner, who took the time to discuss with me things that go from wolf packs to the origin of free will. I spent the last year in Paris working with Mark Wieczorek who wisely guided me through the exploration of a new (to me) branch of planetary sciences, dispensing along the way useful tips about "la vie Parisienne" from the point of view of a foreigner. I strongly believe that science is a collaborative and interactive effort, an opinion built over the course of the numerous interactions I had with Steve Hauck, Bill Moore, Sean Solomon, and Nicola Tosi. They were incredibly willing to share their knowledge and expertise with me. Financial support has been provided by MESSENGER Participating Scientist Program under grant NNX009AR45G, by the UCLA Division of Physical Sciences, by the US-Italy Fulbrigth Commission, and by the Embassy of France in the United States (through a Chateaubriand Fellowship). Finally I want to thank Marianna, Marcella, Alessia P., Marina, Giampaolo, Filomena, Renzo, Diego, Carrie, Shantanu, Cristiano, Chiara, Enrico, Paul, Marta, Andrea, Ivano, Jill, Lauri, Daniela, Alessia C., Clement, Karine, Elisabetta, Luigi, Giovanna, Mario, Matteo F., Luca P., Ricky, James, Laura,

Benny, Michael, Lisa, Mika, Igor, Jonathan, Jodie, Matteo D., Fede, Elettra, Gil, Luca F., Alberto, Anna, Nicola, and Marco for all the things that didn't make it into this dissertation but without which this dissertation would probably not exist.

Vita

2007	B.S. (Astronomy), University of Padova, Italy.
2009	Fulbright fellow, UCLA.
2012	M.S. (Geophysics and Space Physics), UCLA.
2014	Chateaubriand Fellow, Institut de Physique du Globe de Paris, Paris, France.

Publications

Padovan, S., M. A. Wieczorek, J.-L. Margot, N. Tosi, and S. C. Solomon, (2014). Thickness of the crust of Mercury from geoid-to-topography ratios. *Geophys. Res. Lett.*. Under revision.

Padovan, S., J.-L. Margot, S. A. Hauck II, W. B. Moore, and S. C. Solomon, (2014). The tides of mercury and possible implications for its interior structure. *J. Geophys. Res. Planets*, 119, 850-866, doi:10.1002/2013JE004459.

Hauck, S. A. II, J-L. Margot, S. C. Solomon, R. J. Phillips, C. L. Johnson, F. G. Lemoine, E. Mazarico, T. J. McCoy, **S. Padovan**, S. J. Peale, M. E. Perry, D. E. Smith, and M. T. Zuber, (2013). The curious case of Mercury's internal structure. *J. Geophys. Res. Planets*, 118, 1204-1220, doi:10.1002/jgre.20091.

Margot J-L., S. J. Peale, S. C. Solomon, I. Hauck, S. A. II, F. D. Ghigo, R. F. Jurgens, M. Yseboodt, J. D. Giorgini, **S. Padovan**, D. B. Campbell, (2012). Mercury's moment of inertia from spin and gravity data, *J. Geophys. Res. Planets*, 117, E00L09, doi:10.1029/2012JE004161.

Introduction

The work presented in this dissertation is concerned with the some of the actual constraints that we can place on the interior structure of Mercury. By actual constraint it is intended a datum that requires as little extra information or assumptions as possible to be interpreted in terms of interior properties. However, even the most basic piece of information, the mean density of a body, provides very little insight on its interior structure unless it is combined with information about the synthesis of elements in stars and the composition of Earth's rocks and of meteorites.

All the theories and applications described in this dissertation are in principle applicable to all the terrestrial bodies. The category of terrestrial bodies here includes all the bodies with a solid surface whose composition is dominated by silicate rocks and metals and that are massive enough for the gravitational forces to dominate over rigid body forces. The planets of the inner solar system and large natural satellites, such as the Moon and the Galilean satellites, are thus included in this category.

Earth is the best characterized terrestrial body, mostly thanks to data collected through seismometers, which are arguably the most informative instruments for the determination of the interior properties of terrestrial bodies. There are only two examples of non-terrestrial seismological experiments. One is the Apollo Lunar Surface Experiment Package (ALSEP), which operated on the surface of the Moon until 1977 and whose data have been reanalyzed and used to infer a rather accurate description of the lunar interior (*Weber et al.*, 2011). The second seismometer is part of an instrument package which will fly onboard the mission InSight to Mars (*Banerdt et al.*, 2013). Because there are no immedi-

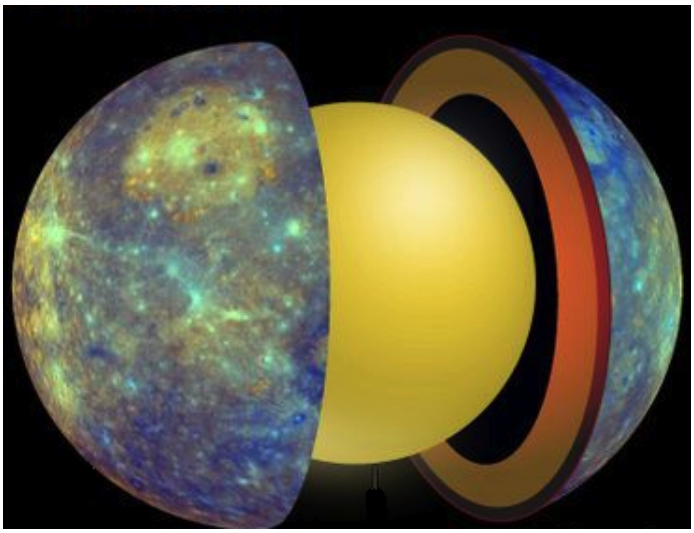

The surface and interior of Mercury. Credit: NASA and Space.com.

ate plans for a geophysical network on Mercury, however, the investigation of its interior structure is currently based on dynamical measurements and on the determination of its gravity field and topography. The figure on top illustrates the current understanding of the interior of Mercury. A large liquid core whose radius is about 80% of the radius of the planet (in yellow) is surrounded by a mantle (orange) and a crust (brown) (*Smith et al.*, 2012; *Margot et al.*, 2012; *Hauck et al.*, 2013; *Rivoldini and Van Hoolst*, 2013).

Organization of the dissertation

The dissertation is organized as follow:

- Chapter 1 describes some basic constraints available for the characterization of terrestrial bodies and the methods used to measure them. Some examples of interior models of Mercury based on these constraints are then illustrated;

- In Chapter 2 we model the response of Mercury to the solar tide and we interpret the measurement of the tidal response in terms of the interior properties of the planet. This chapter represents a verbatim copy of *Padovan et al.* (2014a). The theoretical material behind the models presented in this chapter is found in Appendix A;

- The paper *Padovan et al.* (2014a) was published before an official estimate for the tidal deformation of Mercury was published by the MESSENGER team. Chapter 3 is an update to the conclusions of *Padovan et al.* (2014a), where we reconsider our results in the light of the measurement of the tidal response published in *Mazarico et al.* (2014a);

- Chapter 4 describes our attempt at constraining the thickness of the crust of Mercury from the measurement of the gravitational field and topography of the planet. The work presented in this chapter is currently under revision (*Padovan et al.*, 2014b). A little theoretical background for the material presented in this chapter is found in Appendix D;

- The conclusions and the prospects for future work are presented in Chapter 5.

CHAPTER 1

The interior of terrestrial bodies

1.1 Constraints

1.1.1 Mean density

The mass M and the radius R of a body are directly related to the mean density $\rho \propto M/R^3$. The case of Enceladus provides an instructive example on how this single quantity can provide a large amount of information. Before the Cassini spacecraft reached Saturn and measured the mass of this small natural satellite (whose radius is about 251 km), the mean density was estimated to be about 1100 kg/m^3, indicative of an icy body. The more precise determination made by the Cassini spacecraft, $\rho = 1608$ kg/m^3 (*Porco et al.*, 2006), indicated that silicate rocks and perhaps metals were present in the interior of the body. This opened up the possibility that radiogenic heating, present in the rock component, could sustain the presence of a liquid ocean beneath the icy surface (*Schubert et al.*, 2007). This has been later confirmed by analysis of additional Cassini data (*Iess et al.*, 2014).

The mean densities of Earth and Mercury are equal to 5515 kg/m^3 and 5427 kg/m^3, respectively. These values correspond to the uncompressed densities $\rho \sim$ 4000 kg/m^3 for the Earth and $\rho \sim 5300$ kg/m^3 for Mercury. If we assume that both bodies are made of silicate rocks, with a density of ~ 3000 kg/m^3 and metals,

with a density of ~ 7500 kg/m^3, this implies that Mercury has more metals than the Earth.

1.1.2 Moments of inertia

For a spherically symmetric object of radius R the moment of inertia I is defined as the volume integral

$$I = \int_{\mathrm{V}} \rho(r) r_{\perp}^2 dV = \frac{8\pi}{3} \int_0^{\mathrm{R}} \rho(r) r^4 dr, \tag{1.1}$$

where $r_{\perp}^2$ is the distance with respect to an axis through the center of the body, V is the volume of the body whose radius is R, and the radial coordinate is r. The moment of inertia is sensitive to the radial distribution of matter and therefore gives additional information with respect to the mean density alone. I can be written as $I = \alpha M R^2$, where α is a dimensionless parameter related to the radial distribution of matter. A homogenous sphere corresponds to $\alpha = 0.4$. For the Earth $\alpha = 0.33$, indicating that the mass is concentrated toward the center. For the Moon $\alpha = 0.39$, indicative of a close-to-homogeneous body. No moment of inertia information is available for Venus, and models for its interior structure are usually based on inferences drawn from its similarity with Earth (e.g., *Aitta*, 2012).

Terrestrial bodies are not perfectly spherical, and the value of the moment of inertia will in general depend on the chosen axis. Nevertheless there are only three independent moments, indicated with A, B, and C. A (B, C) is the moment of inertia with respect to the x (y, z) axis. The moment of inertia I of equation (1.1) is here taken as representing the mean moment of inertia,

$$I = \frac{A + B + C}{3}. \tag{1.2}$$

1.1.3 Tidal deformation

The phenomenon of the tides enriches the number of possibilities that can be used in the determination of the internal structure of a planet, since the tidal response is a function of the density, rigidity, and viscosity of the subsurface materials. The theory behind the modeling of the tidal response of a terrestrial body can be found in many sources (e.g., *Alterman et al.*, 1959; *Kaula*, 1968), whose origin are the two works of A. E. H. Love (*Love*, 1911; *Love*, 1927). The problem reduces to the solution of the equations of motion inside the body. The motion includes both material stresses and gravitational forces, the latter originating from a gravitational potential that is the sum of the auto-gravitation and the external tidal potential. The three second-order differential equations of motion are transformed into a system of six first-order linear differential equations in radius (*Alterman et al.*, 1959). A detailed account of the method is given in Appendix A. We report here the key equations. The system of equations to be solved is:

$$\frac{d\mathbf{y}}{dr} = \mathbf{A}\mathbf{y}, \tag{1.3}$$

where $\mathbf{y}$ has six components related to the radial and tangential displacement, radial and tangential stress, incremental gravitational potential (i.e., potential due to the deformation plus external potential), and gravitational potential gradient. Material properties, i.e., density, rigidity, and viscosity, enter both $\mathbf{y}$ and the 6×6 matrix $\mathbf{A}$. The solution can be written as

$$\mathbf{y} = \mathbf{Q}\mathbf{C}. \tag{1.4}$$

Given an interior model for the body, i.e., thickness and material properties for each of its layers, the form of the 6×6 matrix $\mathbf{Q}$ is known (see section A.1.8). The 6×1 vector of constants of integration $\mathbf{C}$ is constrained by the boundary

conditions of the problem. At the center of the planet the radial and tangential displacement and the incremental gravitational potential are zero. At the free surface the radial and tangential stresses are zero and the jump discontinuity in the gravitational potential gradient is known.

We are interested in the gravitational perturbation of the planet induced by the tides, since this has been measured for Mercury (*Mazarico et al.*, 2014a). This is modeled with the Love number k (section 1.2.3 below). From the solution for the incremental gravitational potential (Appendix A) it is possible to calculate the Love number k as[1]

$$k = R\mathsf{y}_5 - 1. \tag{1.5}$$

The modeling of the response to the solar tide has been applied in the past to support the hypothesis of a liquid core in Venus (*Konopliv and Yoder*, 1996) and a global liquid ocean in Titan (*Iess et al.*, 2012). *Yoder et al.* (2003) used the measurement of the tides of Mars to reveal the liquid state of the Martian core and to estimate its radius. We will use the measurement of the response to the solar tide of Mercury to investigate the rheological properties of its outer solid shell.

1.2 Measurable quantities

1.2.1 Gravitational fields

During orbit phase, the main factor affecting the dynamics of an orbiter is the gravitational field of the central body[2]. The analysis of the radio-science segment

[1]Equation (1.5) is consistent with the definition of y_5 given in Appendix A. Different authors define y_5 differently, and the expression for k is accordingly different (e.g., in *Tobie et al.* (2005) $k = \mathsf{y}_5 - 1$).

[2]This situation can be different from case to case, but this is in general true for orbiters around planets.

of an orbiter allows one to derive the parameters used in the description of the gravitational field of the body and then to make inferences about its interior structure. The standard way of representing the gravitational field is by spherical harmonics. The gravitational field U outside a body is (*Kaula*, 1966):

$$U(P) = \frac{GM}{r}\left[1 + \sum_{\mathrm{n}=2}^{\infty}\sum_{m=0}^{\mathrm{n}}\left(\frac{R}{r}\right)^{\mathrm{n}}\left(C_{\mathrm{nm}}\cos m\lambda + S_{\mathrm{nm}}\sin m\lambda\right)P_{\mathrm{nm}}\left(\cos\theta\right)\right]. \tag{1.6}$$

In the previous expression U is evaluated at the position P with coordinates (r, θ, λ) in a body-fixed reference frame. The radial coordinate is r and the pair (θ, λ) represents colatitude and longitude, respectively. G is the gravitational constant, R is the equatorial radius of the body and P_{nm} are the Legendre polynomials. The lack of the $n = 1$ term in the summation implies that the reference frame is centered in the center of mass of the body, whose mass is M. Gravitational fields of Solar System bodies are tabulated in terms of the harmonic (also known as Stokes') coefficients C_{nm} and S_{nm} (available on the NASA planetary data system `http://pds.nasa.gov/`). These are the only terms in equation (1.6) that depend on the interior structure of the body. The formal expression for C_{nm} and S_{nm} is:

$$\begin{Bmatrix} C_{\mathrm{nm}} \\ S_{\mathrm{nm}} \end{Bmatrix} = \frac{2-\delta_{0\mathrm{m}}}{MR^{\mathrm{n}}}\frac{(n-m)!}{(n+m)!}\int_{\mathrm{M}} r'^{\mathrm{n}} P_{\mathrm{nm}}\left(cos\theta'\right)\begin{Bmatrix} \cos m\lambda' \\ \sin m\lambda' \end{Bmatrix} dM', \tag{1.7}$$

where $\delta_{0\mathrm{m}}$ is the Kronecker delta and dM' is the infinitesimal element of mass, $dM' = \rho'\left(r', \theta', \lambda'\right) dV'$. There are simple relations linking the degree 2 coefficients with the moments of inertia of the body. The expression for the moment of inertia

tensor T is (e.g., *Malvern*, 1969):

$$T = \begin{bmatrix} \int\limits_{\mathrm{M}} (y^2+z^2)\, dM' & -\int\limits_{\mathrm{M}} xy\, dM' & -\int\limits_{\mathrm{M}} xz\, dM' \\ -\int\limits_{\mathrm{M}} xy\, dM' & \int\limits_{\mathrm{M}} (x^2+z^2)\, dM' & -\int\limits_{\mathrm{M}} yz\, dM' \\ -\int\limits_{\mathrm{M}} xz\, dM' & -\int\limits_{\mathrm{M}} yz\, dM' & \int\limits_{\mathrm{M}} (x^2+y^2)\, dM' \end{bmatrix}. \tag{1.8}$$

The three diagonal elements correspond to the three moments introduced in equation (1.2), and in a principal axis reference frame the off-diagonal elements are zero. Comparing equation (1.8) with equation (1.7) in a principal axis reference frame the following relations among Stokes' coefficients and moments of inertia are obtained:

$$J_2 = -C_{20} = \frac{1}{MR^2}\left[C - \frac{(A+B)}{2}\right], \tag{1.9}$$

$$C_{22} = \frac{B-A}{4MR^2}. \tag{1.10}$$

The previous equations link two observable quantities, C_{20} and C_{22}, with three quantities that are related to the interior structure of the body: A, B and C. Therefore the measurement of the gravitational field is not sufficient to infer the moment of inertia and an additional relation is required[3].

1.2.2 Dynamical relations

The moment of inertia of a body is related not only to its gravitational field, as illustrated by equations (1.9) and (1.10), but also to how the body responds to an applied external torque. If the torque is known, the modeling of the response to the torque can be used to formulate a third equation, in addition to equations (1.9) and (1.10), and to solve for the moment of inertia.

[3]This holds for a non-principal axis reference frame as well, since to the six independent elements of the inertia tensor correspond only five Stokes' coefficients for $n = 2$.

For rapidly rotating bodies, the precession of the spin pole can be measured. Indicating with $\hat{s}$ the spin pole unit vector, its time evolution (precession) is governed by the equation (e.g., *Bills et al.*, 2009):

$$\frac{d\hat{s}}{dt} = \beta \left(\hat{n} \cdot \hat{s}\right) \left(\hat{s} \times \hat{n}\right), \tag{1.11}$$

where $\hat{n}$ is the orbit pole unit vector and β is a constant that depends on the moments of inertia. Indicating with n the orbital mean motion and ω the spin rate:

$$\beta = \frac{3n^2}{2\omega} \left[\frac{C - (A+B)/2}{C}\right]. \tag{1.12}$$

This relation has been used in combination with equations (1.9) and (1.10) to measure the moment of inertia of Earth and Mars.

In some cases, such as the Galilean satellite Europa, the use of equation (1.11) is impractical because the precession is too slow to be observed (*Bills et al.*, 2009). Furthermore the spin precession and the orbit precession are coupled in bodies that are in Cassini states (as in the case of Europa). However, the theory of Cassini states (*Colombo*, 1966a; *Peale*, 1969) allows one to formulate alternative expressions that can be used to infer the moment of inertia of a terrestrial body.

In the case of Mercury *Peale* (1976) showed that by combining the measurements of the spin parameters (obliquity and amplitude of the forced libration in longitude, which have been inferred for Mercury from radar measurements (*Margot et al.*, 2007, 2012)) with the second harmonic degree components of the gravitational field (J_2 and C_{22}), it is possible to infer the moment of inertia and, in presence of a global liquid layer, the moment of inertia of the outer solid shell with respect to the rotation axis, C_{m} . If this shell extends between the outer radius of the core r_{c} and the surface at radius R, the expression for C_{m} is

$$C_{\mathrm{m}} = \frac{8\pi}{3} \int_{r_{\mathrm{c}}}^{\mathrm{R}} \rho(r) r^4 dr. \tag{1.13}$$

Table 1.1 summarizes the constraints that we currently have on the interior structure of the terrestrial bodies of the inner solar system other than Earth.

1.2.3 Tides

The gravitational field of a body depends on the interior distribution of its mass. Every solar system object is not perfectly rigid and has a finite extent. The latter implies that when the body is under the influence of the gravitational field of another body, gravity force varies inside it. Because of the not perfect rigidity, this variation modifies the shape and as a consequence the distribution of matter inside the body. The gravitational field and the shape are then modified and the extent of these modifications depends on the interior properties.

If an extended body is under the gravitational influence of a tide-raising body of mass $M_{\rm p}$ (where p stands for "perturber"), the gravitational potential W at a point P in the body due to the perturber can be written as:

$$W = \frac{GM_{\rm p}}{l} = \frac{GM_{\rm p}}{r_{\rm p}} \left[\sum_{\rm n=0}^{\infty} \left(\frac{r'}{r_{\rm p}} \right)^{n} P_{\rm n} \left(\cos \psi_{\rm p} \right) \right], \tag{1.14}$$

where l is the distance between P and $M_{\rm p}$. The angle $\psi_{\rm p}$ is the angle between r' and $r_{\rm p}$, the distance of P and $r_{\rm p}$ measured from the center of mass of the body, taken as in Sec. 1.2.1 as the center of the reference frame. The first term of the summation ($n = 0$) represents a constant term ($GM_{\rm p}/r_{\rm p}$) whose gradient is zero. The second ($n = 1$) is a term ($\frac{GM_{\rm p}}{r_{\rm p}^2} r' \cos \psi_{\rm p}$) whose gradient is constant throughout the body. The first term in the expression of W that generates the tide is W_2.

The Love number k is a dimensionless parameter that describes the modification of the gravitational field of the body due to the effect of an external potential. When acted upon by the tidal force, the body will deform. This deformation will

Table 1.1: Measured constraints on the interior of terrestrial bodies.[a]

	Mercury	Venus	Moon	Mars
Mean density ρ [kg/m^3]	5427	5243	3344	3933
Moment of inertia, C/MR^2	0.346 ± 0.014[b]	–	0.392728 ± 0.000012[e]	0.3644 ± 0.0005[g]
Moment of inertia of the outer solid shell, C_m/C	0.431 ± 0.025[b]	–	–	–
Tidal deformation, k_2	0.451 ± 0.014[c]	0.295 ± 0.066[d]	0.02405 ± 0.00018[f]	0.164 ± 0.009[g]

[a] Data for the mean densities are from NASA's planetary fact sheets (`http://nssdc.gsfc.nasa.gov/planetary/planetfact.html`). Unless otherwise noted, errors correspond to one standard deviation. A dash indicates that the value has not been measured.

[b] *Margot et al.* (2012).

[c] This value is indicated as preliminary in *Mazarico et al.* (2014a).

[d] *Konopliv and Yoder* (1996), the error corresponds to two standard deviations.

[e] *Williams et al.* (2014).

[f] *Konopliv et al.* (2013a).

[g] *Konopliv et al.* (2011).

be accompanied by a redistribution of matter. The consequent variation of the gravitational potential of the body, U', is modeled through k, which act as a proportionality constant between U' and W :

$$U'_{\mathrm{n}} = k_{\mathrm{n}} W_{\mathrm{n}}, \tag{1.15}$$

where the subscript n indicates that each harmonic degree of the tide-raising potential will modify the corresponding degree in the potential of the body. In general then the set of parameters k_{n} describes how the gravitational field changes in response to the tide-raising potential[4].

Since in eq. (1.6) the factors that depend on the interior mass distribution of the body are the Stokes' coefficients, it is natural to include the tidal modification by introducing a tidal component in the coefficients. Taking into account the tidal modification, eq. (1.6) for the gravitational field U becomes:

$$U(P) = \frac{GM}{r}\left[1 + \sum_{\mathrm{n}=2}^{\infty}\sum_{\mathrm{m}=0}^{\mathrm{n}}\left(\frac{R}{r}\right)^{\mathrm{n}}\left[C'_{\mathrm{nm}}\cos m\phi + S'_{\mathrm{nm}}\sin m\phi\right]P_{\mathrm{nm}}(\cos\theta)\right], \tag{1.16}$$

where the tidal modification has been modeled through the introduction of time varying Stokes' coefficients,

$$C'_{\mathrm{nm}} = C_{\mathrm{nm}} + \Delta C_{\mathrm{nm}} \quad \text{and} \quad S'_{\mathrm{nm}} = S_{\mathrm{nm}} + \Delta S_{\mathrm{nm}}. \tag{1.17}$$

C_{nm} and S_{nm} represent the static coefficients, while ΔC_{nm} and ΔS_{nm} are the corresponding tidal variations, which are expressed as (*Petit, G. and Luzum, B.*, 2010):

$$\Delta C_{\mathrm{nm}} - i\Delta S_{\mathrm{nm}} = (2-\delta_{0\mathrm{m}})\frac{(n-m)!}{(n+m)!}k_{\mathrm{nm}}\left(\frac{M_{\mathrm{p}}}{M}\right)\left(\frac{R}{r_{\mathrm{p}}}\right)^{\mathrm{n}+1}P_{\mathrm{nm}}\left(\cos\theta_{\mathrm{p}}\right)e^{-\mathrm{im}\phi_{\mathrm{p}}}, \tag{1.18}$$

[4]The expression for W has to be expressed in the same frame of reference used in eq. (1.6), in order to apply expression (1.15).

where the position of the perturber is expressed in the same reference frame used in eq. (1.6). The measurement of the tidal variation of the Stokes' coefficients can be used to infer the magnitude of the Love number k.

1.3 Interior modeling approaches

Modeling the interior structure of a planet with the constraints described in the previous sections is a non-unique problem. Different approaches can be taken and some of them are presented in this section. The most accurate models usually employ the methods of *Sohl and Spohn* (1997), where the mechanical and thermal structures are solved simultaneously (section 1.3.1). We compared the initial results of the MESSENGER mission about the interior structure of Mercury (*Smith et al.*, 2012) with an isothermal model where only the mechanical structure is taken into account (section 1.3.2). There is agreement between the results of this simplified model with those of *Smith et al.* (2012). We also considered the simplest possible model for the interior structure of Mercury, a two constant-density layer model (section 1.3.3). Even in this case there is agreement with the most up-to-date results (*Hauck et al.*, 2013; *Rivoldini and Van Hoolst*, 2013). This represents the motivation to investigate the possible information that would be obtained from the study of the tidal deformation (Chapter 2).

1.3.1 Theory of terrestrial planetary interior modeling

From the mathematical point of view solving for an interior model means solving for a set of partial differential equations with appropriate boundary conditions. The set of equations for a spherically symmetric body in thermal and mechanical

equilibrium are (e.g., *Sohl and Spohn*, 1997):

$$\frac{dm}{dr} = 4\pi\rho r^2, \tag{1.19}$$

$$\frac{dI}{dr} = \frac{8\pi}{3}\rho r^4, \tag{1.20}$$

$$\frac{dg}{dr} = 4\pi G\rho - 2\frac{g}{r}, \tag{1.21}$$

$$\frac{dP}{dr} = -\rho g, \tag{1.22}$$

$$\frac{dq}{dr} = \rho\epsilon - 2\frac{q}{r}, \tag{1.23}$$

$$\frac{dT}{dr} = -\frac{q}{k_r}, \tag{1.24}$$

The equations are:

-(1.19): Continuity equation, where m is the mass, r is the radial coordinate and ρ is the density;

-(1.20): Moment of inertia (I) equation;

-(1.21): Equation for the acceleration of gravity g;

-(1.22): Hydrostatic equilibrium equation, assuming the balance between pressure P and gravitational forces;

-(1.23): Heat flux equation, with q the heat flow density and ϵ the specific heat production rate;

-(1.24): Temperature gradient for boundary layers, with k_r the thermal conductivity.

The temperature profile between boundary layers is assumed to be adiabatic with:

$$\frac{dT}{dr} = T\frac{\gamma}{K_\mathrm{S}}\frac{dP}{dr}, \tag{1.25}$$

where K_S is the adiabatic bulk modulus and γ the Grüneisen parameter. The link between the mechanical properties, Eq. (1.19) to (1.22), and the thermal properties, Eq. (1.23) to (1.24) is provided by the density, which is linked to pressure

and temperature through an equation of state (EoS), $\rho(r) = \rho\left[T\left(r\right), P\left(r\right)\right]$. The solution proceeds by applying boundary conditions at the center (where every variable is zero except for P_{c} and T_{c}) and at the surface.

The application of the previous set of equations to the interior structure of Mercury can be found in *Rivoldini et al.* (2009), *Hauck et al.* (2013), and *Rivoldini and Van Hoolst* (2013). Given the limited amount of constraints available for many terrestrial bodies (Table 1.1), it is instructive to approach the interior modeling using simplified models. Even if they rest on assumptions that are not valid for real bodies, they can often provide useful insights into the interior structure.

1.3.2 Compressible isothermal models

In the system of equations presented in Sec. 1.3.1 the mechanical properties can be separated if an isothermal model is assumed. Radial profiles for mass, density, gravity and pressure can then be obtained by integrating Eq. (1.19), (1.21) and (1.22), along with an isothermal equation of state, which is a relation $P = P\left(\rho\right)$ between pressure and density.

This section presents radial profiles obtained for a two-layer body (core plus mantle) with the mass M and radius R of Mercury. The mantle is assumed to be homogeneous, while the core is modeled as a homogeneous mixture of Fe and FeS. Physical parameters used in the models are listed in Table 1.2. Two third-order isothermal Birch-Murnaghan equations of state relate pressure and density in the mantle and the core (e.g., *Van Hoolst and Jacobs*, 2003). Indicating with ρ_0 the reference density and with K and K' the isothermal bulk modulus and its

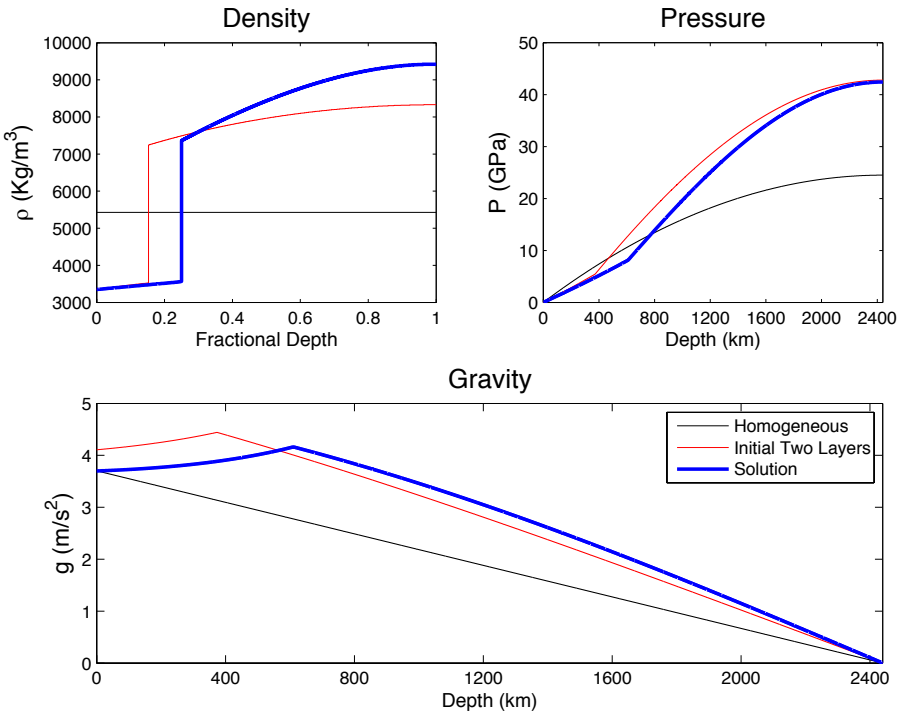

Figure 1.1: Example of an isothermal model of Mercury obtained with the procedure described in Section 1.3.2.

pressure derivative, the equation of state reads

$$P = \frac{3K}{2}\left[\left(\frac{\rho}{\rho_0}\right)^{7/3} - \left(\frac{\rho}{\rho_0}\right)^{5/3}\right]\left\{1 + \frac{3}{4}\left(K' - 4\right)\left[\left(\frac{\rho}{\rho_0}\right)^{2/3} - 1\right]\right\}. \qquad (1.26)$$

An example of the density, pressure, and gravity profiles obtained with this procedure is shown in Fig. 1.1. Black lines represent the profiles for a constant density planet. Red profiles represent the initial solution for a two-layer planet obtained by using as initial guess for the radius of the core the value

$$r_{\rm c} = \left[\frac{\rho - \rho_{\rm m}}{\rho_{\rm c} - \rho_{\rm m}}\right]^{1/3} R, \qquad (1.27)$$

where ρ is the mean density of the planet, and $\rho_{\rm m}$ and $\rho_{\rm c}$ are the densities for the mantle and the core, respectively. The final solution, shown in blue, is obtained

Table 1.2: Material parameters for isothermal models[a].

Parameter[b]	Value$\pm 1\sigma$	Parameter[b]	Value$\pm 1\sigma$
FeS content [wt%]	20 ± 20	Bulk modulus K [GPa]	
Density ρ [kg/m^3]		K_{Fe}	127 ± 12
ρ_{m}	3350 ± 250	K_{FeS}	54 ± 6
ρ_{Fe}	7225 ± 75	$K' = \partial K/\partial P$	
ρ_{FeS}	4940 ± 50	K'_{m}	4.25 ± 0.5
Bulk modulus K [GPa]		K'_{Fe}	2.2 ± 0.2
K_{m}	120 ± 30	K'_{FeS}	4.0 ± 0.2

[a] These models have been calculated before the paper by *Smith et al.* (2012) was published. Therefore the values for the parameters are from *Harder and Schubert* (2001).

[b] The subscripts m, Fe, and FeS refer to mantle, Fe and FeS.

by iteratively adjusting the value of the radius of the core and recalculating the density profile with the equation of state. The convergence criterion chosen is that the mass of the model is accurate to within 1% of M (a value that represents a good balance between accuracy and computation time). Once the model is converged, the values of C/MR^2 (the normalized moment of inertia) and C_{m}/C (the ratio of the moment of inertia of the mantle to the total moment of inertia of the planet) are calculated through integration of Eq. (1.20). Our model is spherically symmetric and we can identify C with I. These values can then be compared with the observed values of $C/MR^2 = 0.353 \pm 0.017$ and $C_{\mathrm{m}}/C = 0.454 \pm 0.035$ (*Smith et al.*, 2012). The solution for the radius of the core r_{c} can be compared with the value of 2030 ± 37 km (*Smith et al.*, 2012).

Since the combined measurement of C/MR^2 and C_{m}/C represents one of the best constraints on the interior structure, it is informative to see how the isothermal models here constructed are sensitive to the parameters listed in Table

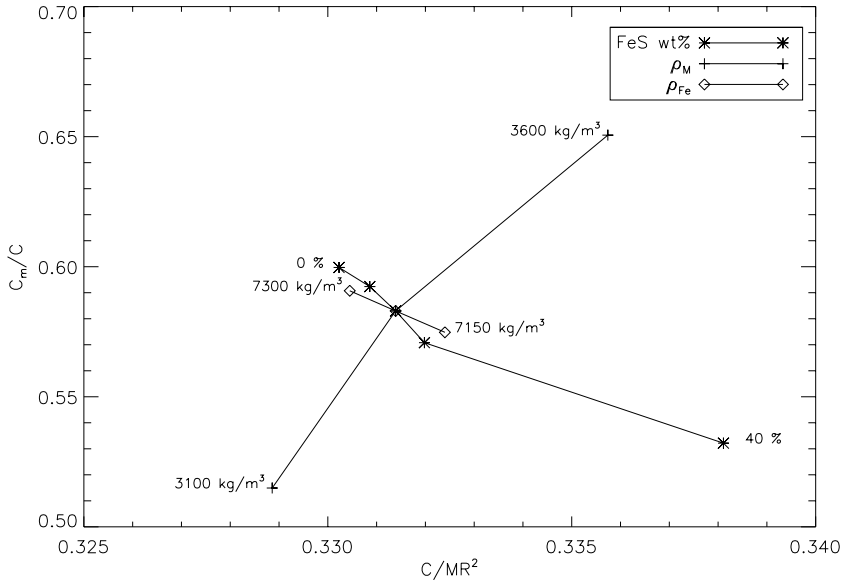

Figure 1.2: Values for C/MR^2 and $C_{\rm m}/C$ for different sets of isothermal models. The central point, where the lines intersect, corresponds to the *nominal model* ($FeS = 20\%$, $\rho_M = 3350\ kg/m^3$ and $\rho_{Fe} = 7225\ kg/m^3$). The other points are obtained by varying the parameter listed in the legend by an amount equal to the *uncertainty* in Table 1.2 (the FeS wt% set has four data points since it goes from 0% to 40% in 10% steps).

1.2. In the following the *nominal model* is defined as the outcome obtained by setting the values of the parameters in Table 1.2 at their *Value*. Different models are then obtained by changing the value of one parameter by an amount equal to the 1σ listed in Table 1.2. Figures 1.2 and 1.3 show the result of this process, where the FeS content in the core and the density of the mantle and of the Fe component of the core are varied. In Figure 1.2 data points are labeled with the value of the varied parameter, while in Figure 1.3 they are labeled with the solution for the radius of the core $r_{\rm c}$ of the model.

From Figures 1.2 and 1.3 the following effects of the variation of the parameters on the solution appear: increasing the light element in the core causes the

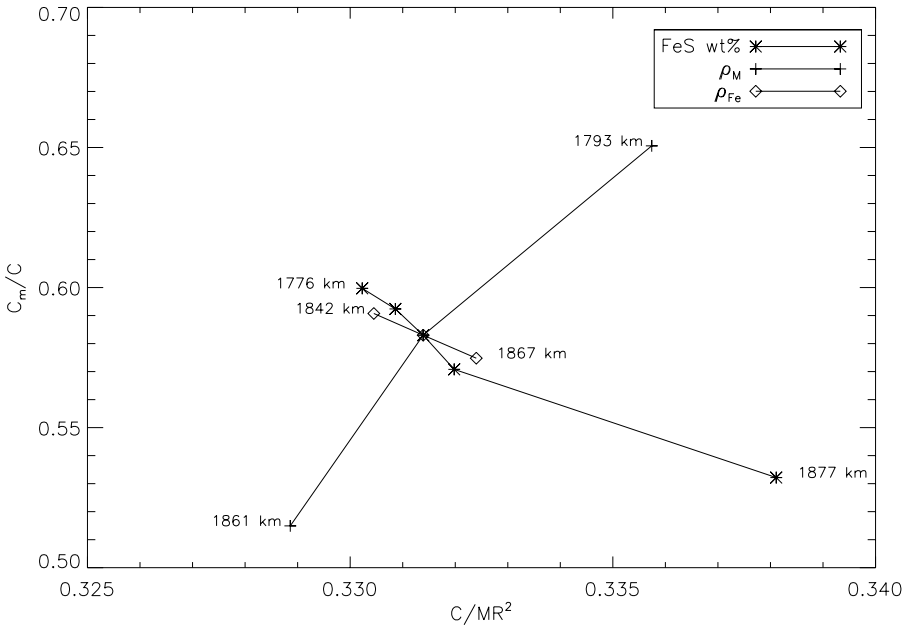

Figure 1.3: Same data sets as in Fig. 1.2. Here the labels show the solution for the radius of the core for the model.

core to expand (since the total mass M and the other parameters are kept fixed), while increasing the total moment of inertia and decreasing the mantle moment of inertia. Given that the core expands, there is more heavy material far from the axis (thus C increases) and at the same time the mass of the mantle, which contributes to $C_{\rm m}/C$, decreases. Varying the density of the Fe component of the core has similar effects both in the moments of inertia values and in the radius of the core, since the variation of this parameter is qualitatively similar to a variation of the amount of the light component. The variation of the density of the mantle has a "perpendicular" effect. A positive variation in the density of the mantle increases both the moment of inertia of the mantle and the total moment of inertia. If the mantle is heavier, than it takes a larger fraction of the mass M, and as a consequence the radius of the core $R_{\rm c}$ is smaller. In Figure 1.4 the mod-

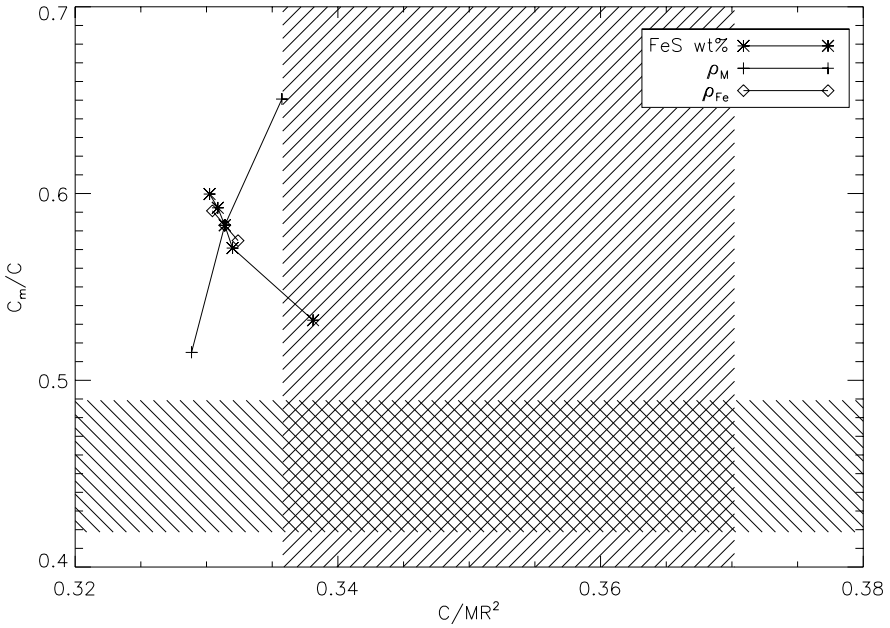

Figure 1.4: Same date sets as in Figure 1.2 and 1.3. This plot allows to compare the solutions obtained with the isothermal models with the values determined with MESSENGER data, which are represented by the lined bands.

els here described are compared with the values for C/MR^2 and $C_{\rm m}/C$ published in *Smith et al.* (2012). There is only marginal match for the value of C/MR^2 for models with a high content of FeS or a heavy mantle. On the other hand all the models are systematically overestimating the ratio $C_{\rm m}/C$. Nevertheless, even with these simple models both the values of the density of the outer shell and the radius of the core are compatible with a subset of the more detailed models appearing in *Smith et al.* (2012), which are shown in Figure 1.5 for comparison. Further parallels are difficult to make since *Smith et al.* (2012) do not describe the values of all the parameters.

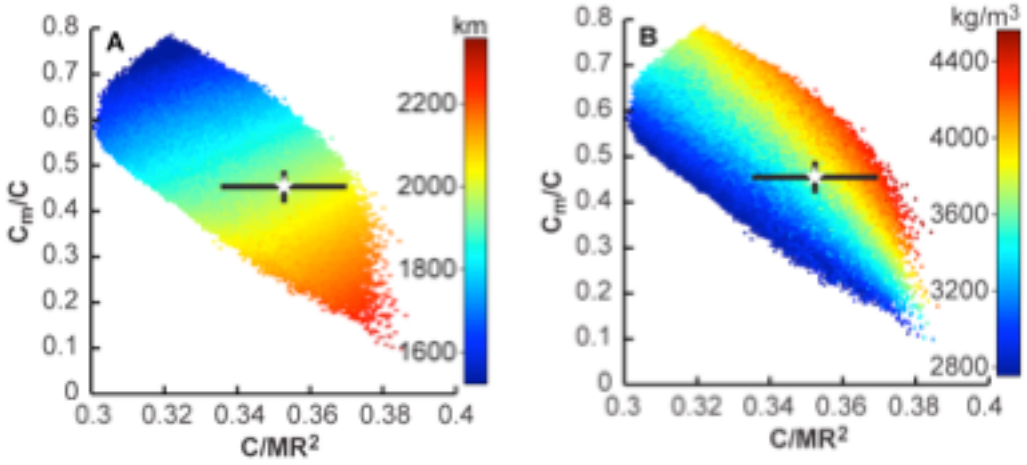

Figure 1.5: A) Radius of the core. B) Average density of the shell overlying the core. The star represents the central values for C/MR^2 and $C_{\rm m}/C$, the black bars are $1-\sigma$ values. From Figure 2 of *Smith et al.* (2012).

1.3.3 Constant-density layer models

Earth is divided into a metal rich core (itself comprised of a solid inner core and a liquid outer core) and a rocky outer envelope which is divided into a mantle surrounded by a crust. The simplest model for a differentiated body is based on this compositional dichotomy, i.e., it assumes a constant-density core and a constant-density mantle. The parameters of this model are the core density and radius, $\rho_{\rm c}$ and $r_{\rm c}$, and the mantle density $\rho_{\rm m}$. The equations for the mean density and moment of inertia of this model are

$$\rho = \rho_{\rm c}\left(\frac{r_{\rm c}}{R}\right)^3 + \rho_{\rm m}\left[1-\left(\frac{r_{\rm c}}{R}\right)^3\right], \tag{1.28}$$

$$I = \frac{8\pi}{15}\left[\rho_{\rm c} r_{\rm c}^5 + \rho_{\rm m}\left(R^5 - r_{\rm c}^5\right)\right]. \tag{1.29}$$

If only the two observables ρ and I are available, the system is underdetermined and one has to make at least one assumption, for example the density of the

mantle rocks, to retrieve the density and radius of the core.

In the case of Mercury the moment of inertia of the outer solid shell has been measured (*Margot et al.*, 2012). In the 2-layer model, I_m has the expression

$$I_\mathrm{m} = \frac{8\pi}{15}\rho_\mathrm{m}\left(R^5 - r_\mathrm{c}^5\right). \tag{1.30}$$

The three equations (1.28),(1.29), and (1.30) can then be solved for the three unknowns r_c, ρ_c, and ρ_m. The resulting solutions are $\rho_\mathrm{m} = 3203\,\mathrm{kg/m^3}$, $\rho_\mathrm{c} = 7254\,\mathrm{kg/m^3}$, and $r_\mathrm{c} = 1998\,\mathrm{km}$. These are all within one standard deviation of the results of the more elaborate models of *Hauck et al.* (2013), $\rho_\mathrm{m} = 3380 \pm 200\,\mathrm{kg/m^3}$, $\rho_\mathrm{c} = 6980 \pm 280\,\mathrm{kg/m^3}$, $r_\mathrm{c} = 2020 \pm 30\,\mathrm{km}$, and of *Rivoldini and Van Hoolst* (2013), $\rho_\mathrm{c} = 7233 \pm 267\,\mathrm{kg/m^3}$ and $r_\mathrm{c} = 2004 \pm 39\,\mathrm{km}$. It is important to note that these results are consistent with a wide variety of core compositions (*Hauck et al.*, 2013) and mantle mineralogies (*Rivoldini et al.*, 2009; *Rivoldini and Van Hoolst*, 2013). Therefore the mean density and the two moments of inertia C and C_m are not very sensitive to the different compositions of the interior.

CHAPTER 2

The tides of Mercury and possible implications for its interior structure[1]

2.1 Abstract

The combination of the radio tracking of the MESSENGER spacecraft and Earth-based radar measurements of the planet's spin state gives three fundamental quantities for the determination of the interior structure of Mercury: mean density ρ, moment of inertia C, and moment of inertia of the outer solid shell $C_{\rm m}$. This work focuses on the additional information that can be gained by a determination of the change in gravitational potential due to planetary tides, as parametrized by the tidal potential Love number k_2. We investigate the tidal response for sets of interior models that are compatible with the available constraints (ρ, C, and $C_{\rm m}$). We show that the tidal response correlates with the size of the liquid core and the mean density of material below the outer solid shell, and that it is affected by the rheology of the outer solid shell of the planet, which depends on its temperature and mineralogy. For a mantle grain size of 1 cm, we calculate that the tidal k_2 of Mercury is in the range 0.45 to 0.52. Some of the current models for the interior structure of Mercury are compatible with the existence of a solid FeS layer at the top of the core. Such a layer, if present, would increase the tidal

[1] ***Padovan et al.* (2014a), reproduced by permission of Wiley (©2014. American Geophysical Union. All Rights Reserved).**

response of the planet.

2.2 Introduction

In the absence of an in situ geophysical network, what we know of the interior of Mercury is based on a combination of Earth-based observations, spacecraft exploration, and theoretical insight. Earth-based radar observations provide measurements of the obliquity of Mercury and the amplitude of its forced libration (*Margot et al.*, 2007, 2012). Through radio tracking of the MErcury Surface, Space ENvironment, GEochemistry, and Ranging (MESSENGER) spacecraft, the gravitational field of the planet has been determined (*Smith et al.*, 2012). Given that Mercury is in a Cassini state (*Colombo*, 1966b; *Peale*, 1969), the spin parameters (obliquity θ and angle of libration γ), when combined with the second harmonic degree components of the gravity field (J_2 and C_{22}), provide two important integral constraints for the interior of Mercury, the moment of inertia C (*Peale*, 1969) and, in the presence of a global liquid layer, the moment of inertia of the outer solid shell C_{m} (*Peale*, 1976). These two moments, along with the mean density ρ, are three constraints that any model of the interior of Mercury must satisfy (*Hauck et al.*, 2013).

The measurement of the deformation of a planet due to periodic tidal forcing can be used to place additional bounds on the interior structure, because the tidal response is a function of the density, rigidity, and viscosity of the subsurface materials. This property has been applied in the past to support the hypothesis of a liquid core in Venus (*Konopliv and Yoder*, 1996) and a global liquid ocean in Titan (*Iess et al.*, 2012). *Yoder et al.* (2003) used the measurement of the tides to reveal the liquid state of the Martian core and to estimate its radius. It is interesting to note that the interior structures of Venus and Mars are currently

less well-characterized than that of Mercury, since for Mars the moment of inertia of the outer solid shell is not known, and for Venus only the mean density and k_2 tidal deformation are known, but no moment of inertia information is available.

The motivation for this paper is to explore the information that can be gained about the interior of Mercury by the combination of the determinations of ρ, C, and $C_{\rm m}$ with the measurement of k_2, which will indicate the 88-day annual tidal k_2.

We model the tidal response of Mercury for a range of interior structures that are compatible with the mean density ρ and the moments of inertia C and $C_{\rm m}$ (*Hauck et al.*, 2013). The formalism that we employ is described in section 2.3, and section 2.4 describes the interior models that we use and the assumptions that we make in the evaluation of the tidal response. The rheology of the outer solid shell is discussed in section 2.5. The results of our simulations are presented in section 2.6 (the minor effects of the properties of the inner core on the tidal response are explored in Appendix C). We discuss the implications of the detection of the tidal response for the physical characterization of the interior of Mercury in section 2.7.

2.3 Planetary Tidal Deformation

Mercury's solar tides are caused by the difference in the gravitational attraction of the Sun across the planet. Denoting the mass of the Sun by $M_{\rm S}$, the expression for the solar tide-generating potential Φ at a point P inside the planet is

$$\Phi = \frac{GM_{\rm S}}{d} = \frac{GM_{\rm S}}{r_{\rm S}} \left[\sum_{\rm n=2}^{\infty} \left(\frac{r'}{r_{\rm S}} \right)^{\rm n} P_{\rm n} \left(\cos \psi_{\rm P} \right) \right] = \sum_{\rm n=2}^{\infty} \Phi_{\rm n}, \tag{2.1}$$

where the summation follows from the expansion for $(1/d)$, and d is the distance between P and the Sun (e.g., *Arfken and Weber*, 2005). The angle $\psi_{\rm P}$ is the

angle between r' and $r_{\rm S}$, the distances from the center of mass of the body to P and to the Sun, respectively. $P_{\rm n}$ indicates the Legendre polynomial of degree n. G is the gravitational constant. We introduce $\Phi_{\rm n}$ to highlight the dependence of Φ on the $n^{\rm th}$ power of the factor $(r'/r_{\rm S}) \ll 1$. For a point on the surface, we set $r' = R_{\rm M}$, the radius of Mercury, and $r_{\rm S}$ equal to $a_{\rm M}$, the semimajor axis of Mercury's orbit, and we can express the largest component of the potential as $g\zeta P_2(\cos\psi_{\rm P})$, where $g = (GM_{\rm M}/R_{\rm M}^2)$ is the gravitational acceleration at the surface, $M_{\rm M}$ is the mass of Mercury, $\zeta P_2(\cos\psi_{\rm P})$ is the height of the equilibrium tide (*Murray and Dermott*, 1999), and where

$$\zeta = \frac{M_{\rm S}}{M_{\rm M}} \left(\frac{R_{\rm M}}{a_{\rm M}}\right)^3 R_{\rm M}. \tag{2.2}$$

Among the terrestrial planets ζ is the largest for Mercury, with a value of ~ 1.10 m (for comparison $\zeta_{\rm Venus} \sim 0.43$ m, $\zeta_{\rm Earth} \sim 0.16$ m, and $\zeta_{\rm Mars} \sim 0.03$ m).

The harmonic expansion of the tide-generating potential in equation (2.1) can be used to identify all the different tidal components (in period and amplitude) generated by the Sun at Mercury (*Van Hoolst and Jacobs*, 2003). The largest component has a timescale equal to the orbital period of Mercury around the Sun ($\sim$ 88 days). This annual tidal perturbation periodically modifies the shape of Mercury, and thus the distribution of matter inside the planet, with an accompanying modification of its gravitational field. This modification is parameterized with the potential Love number k_2, which relates the additional potential $\phi_{\rm 2t}$ due to the deformation of the planet to the tide-generating potential Φ_2 due to the Sun:

$$\phi_{\rm 2t} = k_2\,(\omega)\ \Phi_2. \tag{2.3}$$

The subscript 2 indicates that the main deformation is generated by the largest term of the expansion, which corresponds to $n = 2$. The frequency ω indicates that the response of the body, described by k_2, depends on the period (i.e., frequency)

of the applied forcing, which for the case considered here is the 88-day-period solar tide.

The study of the deformation of a planet under the perturbation of an external potential requires the solution of the equations of motion inside the body. Using a spherical harmonic decomposition in latitude and longitude, we transform these three second-order ordinary differential equations into six first-order linear differential equations in radius (*Alterman et al.*, 1959). The motion is controlled both by material stresses (elastic or viscoelastic) and gravitational forces, the latter originating from a gravitational potential that is the sum of the self-gravitation of the planet and the external tidal potential. The framework for the solution is formally the same both for elastic rheologies and for viscoelastic rheologies, thanks to the correspondence principle (*Biot*, 1954). The results presented in the following sections are obtained by modeling Mercury as a series of homogeneous incompressible layers. Each layer is characterized by thickness, density, rigidity, and viscosity (*Wolf*, 1994). In evaluating the tidal response, we use the formalism developed by *Moore and Schubert* (2000).

The possible values for the k_2 of a planet range between 0 for a perfectly rigid body that does not deform, and 1.5, the value for a homogeneous fluid body (for these idealized bodies the limits are independent of the forcing frequency). Values for k_2 have been determined for Venus (*Konopliv and Yoder*, 1996), the Moon (*Konopliv et al.*, 2013b; *Lemoine et al.*, 2013), Mars (*Konopliv et al.*, 2011), and Titan (*Iess et al.*, 2012). The k_2 of the Moon is uncertain at the $\sim 0.5\%$ level, a result of the high-quality data obtained with the Gravity Recovery and Interior Laboratory (GRAIL) mission (*Zuber et al.*, 2013). For Mars the estimate is uncertain at the $\sim 5\%$ level, a result obtained by combining data from a large number of spacecraft missions, including a lander and two years of tracking data from the

low-altitude, nearly circular orbital phase of the Mars Reconnaissance Orbiter. For Venus and Titan the estimates have an uncertainty $\gtrsim 10\%$. A numerical simulation of the determination of Mercury's k_2 with BepiColombo, the future dual orbiter mission to Mercury by the European Space Agency and the Japan Aerospace Exploration Agency, indicates an expected accuracy of $\sim 1\%$ (*Milani et al.*, 2001). This figure represents a lower bound for MESSENGER, because its eccentric orbit makes the detection of k_2 more challenging. The uncertainty on the determination of the k_2 of Mercury as obtained from MESSENGER is expected to be $\sim 10\%$ (*Mazarico et al.*, 2014a).

2.3.1 Rheological Models of the Interior

The mantle of Earth responds elastically on the short timescales associated with the waves generated by earthquakes but flows like a fluid on the geologically long timescales of mantle convection. The Maxwell rheological model is the simplest model that captures this short- and long-timescale behavior. It is completely defined by two parameters, the unrelaxed (infinite-frequency) rigidity $\mu_{\rm U}$ and the dynamic viscosity ν. The Maxwell time, defined as

$$\tau_{\rm M} = \frac{\nu}{\mu_{\rm U}}, \tag{2.4}$$

is a timescale that separates the elastic regime (forcing period $\ll \tau_{\rm M}$) from the fluid regime (forcing period $\gg \tau_{\rm M}$). This simple rheological model is sufficiently accurate for the crust, which is cold and responds elastically, and the liquid core, which has zero rigidity and therefore a fluid response. The inner core, if present, has a negligible effect on the tidal response (Appendix C), so for simplicity we use a Maxwell model to describe its rheology. Nevertheless the Maxwell model does not provide a good fit to laboratory and field data in the low-frequency seismological range, and thus it should not be used to model the response of the

mantle at tidal frequencies (e.g., *Efroimsky and Lainey*, 2007; *Nimmo et al.*, 2012).

Jackson et al. (2010) explored three different parameterizations (Burgers, extended Burgers, and Andrade pseudo-period) to fit torsional oscillation data from a set of melt-free olivine samples. Both the Burgers models and the Andrade model provide a good fit for the low-frequency data. The small number of parameters required for the Andrade model makes it more attractive to model the rheology of Mercury, for which we lack any ground-truth data. Note, however, that both the Burgers models and the Andrade model have not been tested at periods longer than 10^3 s, so when applied to the study of planetary tidal deformation (period $> 10^6$ s) they both need to be extrapolated (for an application of the extended Burgers model to the mantle of the Moon and Mars see *Nimmo et al.* (2012) and *Nimmo and Faul* (2013), respectively).

We report here the expressions for the real and imaginary part of the dynamic compliance $J(\omega)$ for the Andrade-pseudoperiod model, as described by *Jackson et al.* (2010):

$$J_{\mathrm{R}}(\omega) = \frac{1}{\mu_{\mathrm{U}}}\left\{1+\beta^{*}\Gamma(1+n)\omega^{-\mathrm{n}}\cos\left(\frac{n\pi}{2}\right)\right\}, \tag{2.5}$$

$$J_{\mathrm{I}}(\omega) = \frac{1}{\mu_{\mathrm{U}}}\left\{\beta^{*}\Gamma(1+n)\omega^{-\mathrm{n}}\sin\left(\frac{n\pi}{2}\right)+\frac{1}{\omega\tau_{\mathrm{M}}}\right\} \tag{2.6}$$

The unrelaxed rigidity is μ_{U} and $\beta^{*} = \beta\mu_{\mathrm{U}}$. The coefficient β, along with n, appear in the expression of the Andrade creep $J(t) = 1/\mu_{\mathrm{U}} + \beta t^{\mathrm{n}} + t/\nu$, where Γ is the gamma function and τ_{M} the Maxwell time. The frequency ω is obtained from $\omega = 2\pi/X_{\mathrm{B}}$, where X_{B} is the pseudo-period master variable introduced by *Jackson et al.* (2010):

$$X_{\mathrm{B}} = T_0\left(\frac{d}{d_{\mathrm{R}}}\right)^{-\mathrm{m}}\exp\left[\left(\frac{-E_{\mathrm{B}}}{R}\right)\left(\frac{1}{T}-\frac{1}{T_{\mathrm{R}}}\right)\right]\exp\left[\left(\frac{-V}{R}\right)\left(\frac{P}{T}-\frac{P_{\mathrm{R}}}{T_{\mathrm{R}}}\right)\right], \tag{2.7}$$

which takes into account the effects of pressure P, temperature T, and grain-size d. The subscript R indicates reference value. T_0 is the forcing period (for Mercury ~ 88 days). The exponent m characterizes the dependence on the grain size, which in principle can be different for anelastic processes (m_a) and for viscous relaxation (m_v). We tested that at the frequency of the Mercury tide, the effect is minor, and we assumed $m_a = m_v = m$. The other quantities are defined in Table 2.1. The dynamic compliance was evaluated by setting the value of $\tau_{\rm M}$ in equation (2.6) equal to the reference value reported by *Jackson et al.* (2010, Table 2, $\tau_{{\rm M}R} = 10^{5.3}$ s), and including the effects of T, P, and d through the pseudo-period master variable defined in equation (2.7). The dynamic compliance is related to the inverse quality factor Q^{-1} and the rigidity μ by

$$Q^{-1}(\omega) = \frac{J_{\rm I}(\omega)}{J_{\rm R}(\omega)}, \tag{2.8}$$

$$\mu(\omega) = \left[J_{\rm R}^2(\omega) + J_{\rm I}^2(\omega)\right]^{-1/2}. \tag{2.9}$$

To illustrate the importance of choosing a realistic rheological model, in Figure 2.1 we show how the rigidity of a material with $\mu_{\rm U} = 65$ GPa varies as a function of the forcing frequency for two temperatures, at a pressure of 5.5 GPa, representative of conditions at the base of the mantle of Mercury (*Hauck et al.*, 2013). Both the Maxwell rheological model and the Andrade model are plotted. They both predict a fluid response (i.e., zero rigidity) at high temperatures and/or long forcing frequencies, but the Maxwell model underestimates non-elastic effects at forcing periods that are shorter than the Maxwell time. This effect is particularly relevant for Mercury, for which the core-mantle boundary temperature may be above 1600 K (*Rivoldini and Van Hoolst*, 2013; *Tosi et al.*, 2013).

Table 2.1: Rheological Models for the Interior of Mercury[a].

Layer	Model	Parameter	Definition	Value
Crust	Maxwell			
		μ_{U}	Unrelaxed rigidity	55 GPa
		ν	Dynamic viscosity	10^{23} Pa s
Mantle	Andrade[b]			
		μ_{U}	Unrelaxed rigidity	$59 - 71$ GPa
		T_{b}	Mantle basal temperature[c]	$1600 - 1850$ K
		n	Andrade creep coefficient	0.3
		β^*	Andrade creep parameter	0.02
		P_{R}	Reference pressure	0.2 GPa
		T_{R}	Reference temperature	1173 K
		d_{R}	Reference grain-size	3.1 μm
		d	Grain size	1mm – 1cm
		m	Grain size exponent	1.31
		V	Activation volume	10^{-5} $\mathrm{m^3 mol^{-1}}$
		E_{B}	Activation energy	303×10^3 kJ $\mathrm{mol^{-1}}$
FeS	Andrade[d]			
Outer core	Maxwell			
		μ_{U}	Unrelaxed rigidity	0 Gpa
		ν	Dynamic viscosity	0 Pa s
Inner core	Maxwell			
		μ_{U}	Unrelaxed rigidity	10^{11} GPa
		ν	Dynamic viscosity	10^{20} Pa s

[a] The models are introduced in Section A.2.2.

[b] The fixed parameters of the Andrade model are based on the results of *Jackson et al.* (2010).

[c] Here we report T_{b} because the temperature T in equation (2.7) depends on the temperature profile, which is controlled by T_{b}.

[d] The FeS layer is assumed to have the same rheology as that of the base of the mantle.

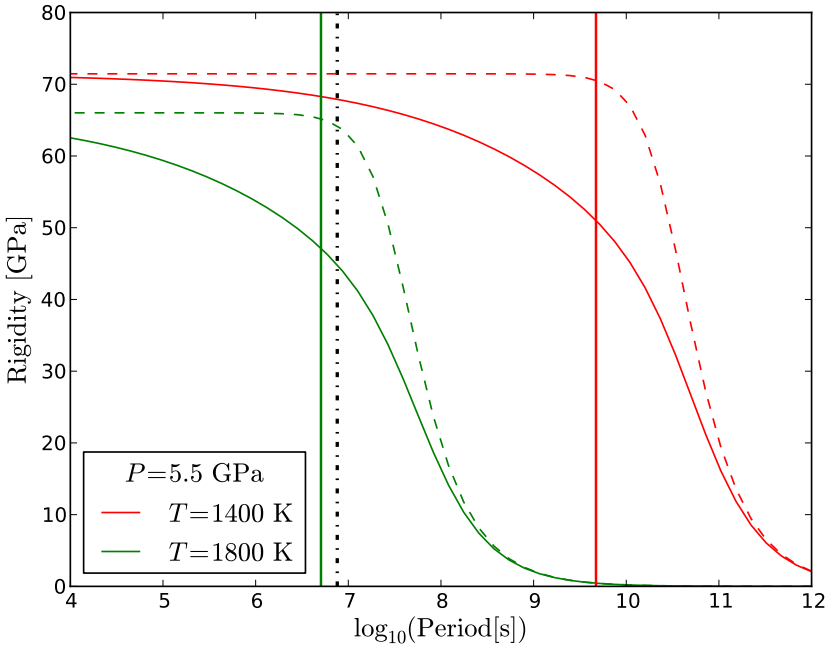

Figure 2.1: Comparison of the Andrade (solid lines) and Maxwell (dashed lines) rheological models at a pressure of 5.5 GPa for two different temperatures, $T = 1400$ K (red) and $T = 1800$ K (green). The solid colored vertical lines represent the Maxwell times. The dash-dotted line indicates the forcing frequency of Mercury's tide. Note that at $T = 1800$ K the Maxwell model over-estimates the rigidity at the tidal frequency by about 35% compared with the Andrade model. The unrelaxed modulus used in these example is 65 GPa.

2.4 Methods

Throughout this work (except section 2.4.1) we use models compatible with the available constraints, i.e., mean density ρ, moment of inertia C, and moment of inertia of the solid outer shell $C_{\rm m}$ (section 2.2). By compatible we mean that the distributions of ρ, C, and $C_{\rm m}$ in the set of interior models considered here

are approximately Gaussian with means and standard deviations that match the nominal values of the observables and their one-standard-deviation errors. The mean density ρ has a Gaussian distribution with mean and standard deviation equal to 5430 kg/m^3 and 10 kg/m^3, respectively. For C and $C_{\rm m}$, we choose Gaussian distributions with means and standard deviations defined by the observed values and errors reported by *Margot et al.* (2012). Accordingly $C/M_{\rm M}R_{\rm M}^2 = 0.346 \pm 0.014$ and $C_{\rm m}/C = 0.431 \pm 0.025$ (*Margot et al.*, 2012).

The small abundance of Fe and relatively large abundance of S at the surface of Mercury imply strongly reducing conditions within the planet (*Nittler et al.*, 2011). Under these conditions both silicon and sulfur likely partitioned into the core during Mercury's formation and differentiation (*Hauck et al.*, 2013). Of the five compositional models for the interior of Mercury analyzed by *Hauck et al.* (2013), we focus on two sets that have a Si-bearing core, because they are consistent with the inferred reducing conditions. The major difference between the two sets is the presence or absence of a solid FeS layer at the top of the core. We label these two sets the FeS-set and NoFeS-set, respectively.

The possible presence of an FeS layer was initially predicated on the basis of the inferred highly reducing conditions and the then-best estimate of the high mean density of the outer solid shell (*Smith et al.*, 2012). Improved values of the obliquity θ (*Margot et al.*, 2012) led to a revised value for the mean density of the outer solid shell (*Hauck et al.*, 2013) and made the density argument for the presence of the FeS layer less compelling. Nevertheless, the geochemical argument supporting the presence of the FeS layer is still valid (*Hauck et al.*, 2013), and a conductive layer above the convective liquid core is one of the possible explanations for Mercury's weak magnetic field (*Christensen*, 2006; *Anderson et al.*, 2012).

2.4.1 Radial Density Profile

The radial density profiles that we used as input (*Hauck et al.*, 2013) are given as series of constant-property layers, going from the center to the surface. The crust, mantle, and FeS layer are modeled as constant-density shells. This simplification is justified by the small thickness of the outer solid shell of Mercury and by the relatively low surface gravitational acceleration but does not affect the characterization of the interior of the planet on the basis of the measured values of ρ, C, and $C_{\rm m}$ (*Hauck et al.*, 2013). The core (inner+outer) is represented with $\sim$ 1000 layers in order to take into account the effects of self-compression and temperature in the equation of state for core materials, as was done by *Hauck et al.* (2013). However, the Love number k_2 is a global parameter, summarizing the response of the planet to tidal forcing, and it is not very sensitive to the fine density structure. We verified that k_2 calculations can be performed accurately with simplified, 4- or 5-layer models instead of the original $\sim$ 1000-layer models. In order to establish this point, we used a random sample of 100 models drawn from the FeS-set and constrained only by the mean density ρ of Mercury. For this test we did not apply the moment of inertia constraints (C and $C_{\rm m}$), as this allowed us to explore a larger parameter space and resulted in a more robust test. For each one of the 100 models we computed an averaged version, characterized by five constant-density layers. Computed k_2 values for the $\sim$1000-layer models and the corresponding 5-layer models are shown in the top panel of Figure 2.2. Their ratio (Figure 2.2, bottom panel) indicates that errors introduced by using the simplified models are $\lesssim 2\%$. In view of this result and of the $\sim 10\%$ expected accuracy of MESSENGER's k_2 determination (section 2.3), in what follows we show results obtained with the simplified 4- or 5-layer models. This approach reduces the computational cost by $\sim$ three orders of magnitude.

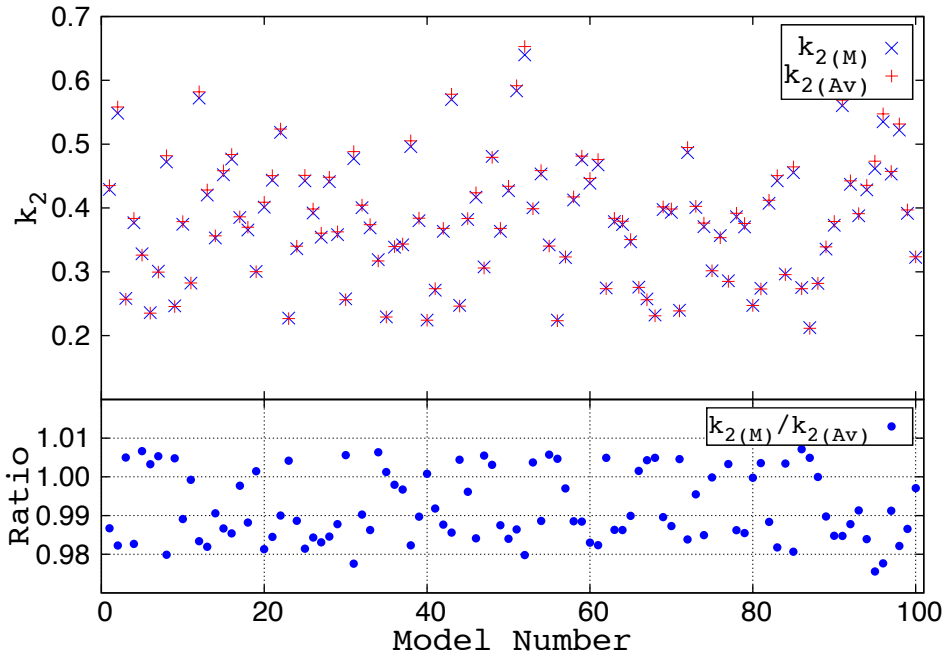

Figure 2.2: Effect of the radial density profile on the magnitude of k_2. For each of a set of 100 models, the value of k_2 has been calculated both for the ∼1000-layer version ($k_{2(\mathrm{M})}$) and for the 5-layer version ($k_{2(\mathrm{Av})}$). (Bottom) The ratio of the two determinations, which in most cases is within 2% of unity. The models used for this plot are constrained only by the mean density of Mercury.

2.4.2 Pressure and Temperature Profiles in the Mantle

To calculate a rheological profile for the mantle of Mercury with the Andrade rheological model described in Section 2.3.1, the pressure and temperature as a function of depth must be calculated.

At the radius r in the mantle the pressure is simply obtained as an overburden load $P(r) = g[\rho_{\mathrm{c}} h_{\mathrm{c}} + \rho_{\mathrm{m}} h_{\mathrm{m}}(r)]$, where the subscripts "c" and "m" refer to the crust and mantle, respectively. h_{c} is the crustal thickness, and $h_{\mathrm{m}}(r)$ is the thickness of the mantle above r (i.e., $r + h_{\mathrm{m}}(r) + h_{\mathrm{c}} = R_{\mathrm{M}}$).

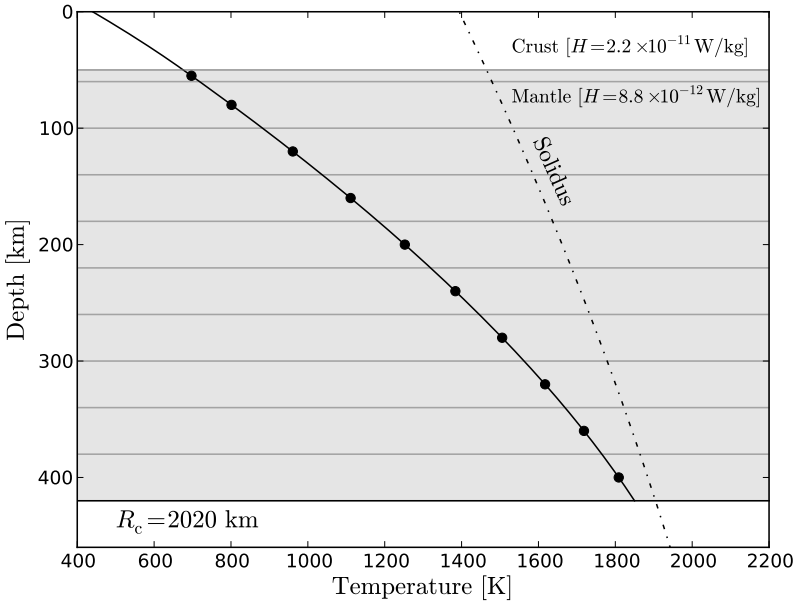

Figure 2.3: Temperature (solid line) as a function of depth for a model with a 2020-km radius core and a 50-km-thick crust. The values for the heat production rate in the crust and mantle are indicated. The dots represent the midpoint of each mantle sublayer, for which the temperature and pressure are used to derive a rheology for the sublayer. The peridotite solidus of *Hirschmann* (2000) is also shown.

We obtained the temperature profile by solving the static heat conduction equation with heat sources in spherical coordinates (e.g., *Turcotte and Schubert*, 2002) in the mantle and crust:

$$k\frac{1}{r^2}\frac{d}{dr}\left(r^2\frac{dT}{dr}\right)+\rho H=0. \tag{2.10}$$

In equation (2.10) k is the thermal conductivity, ρ is the density, and H is the heat production rate.

We assumed a homogeneous distribution of heat sources in the crust and in the mantle. The distribution in the crust might be exponential as in the crust of the Earth, but we verified that this would only marginally affect the deep-mantle

temperature profile. The value of H at the surface, H_0, has been inferred from MESSENGER measurements and is equal to $H_0 = 2.2 \times 10^{-11}$ W kg^{-1} (*Peplowski et al.*, 2012). We adopted the surface value H_0 for the heat production rate in the crust, $H_c = H_0$. For the distribution of heat sources in the mantle we used $H_m = H_0/2.5$, which is compatible with the enrichment factor derived by *Tosi et al.* (2013). The value of k is set to 3.3 Wm^{-1}K^{-1}.

As boundary conditions we applied the surface temperature T_S and the temperature at the base of the mantle T_b. T_S is set to 440 K, a value obtained with a simple equilibrium temperature calculation. Therefore in our models the temperature profile is controlled by the temperature T_b. There are currently few constraints on T_b, but two independent sets of workers (*Rivoldini and Van Hoolst*, 2013; *Tosi et al.*, 2013) point to the range 1600-1900 K. We defined two end-members profiles: a cold mantle with $T_b = 1600$ K, and a hot mantle with $T_b = 1850$ K. We consider $T_b = 1850$ K as our hot mantle case, since, from the peridotite solidus of *Hirschmann* (2000), $T_b = 1900$ K would result in partial melting at the base of the mantle (Figure 2.3). We did not consider in this work the presence of partial melting.

The rheological models described in section 2.3.1 strongly depend on the temperature. Our end-member temperature profiles are obtained under the assumption of a conductive mantle. This assumption is consistent with the results of *Tosi et al.* (2013), which indicate that the mantle of Mercury is most likely conductive at the present time. Nevertheless, a present-day convective mantle is not excluded (*Michel et al.*, 2013; *Tosi et al.*, 2013). A convective mantle for the $T_b = 1850$ K case would result in partial melting (Figure 2.3). A convective profile with $T_b = 1600$ K would be more dissipative and deformable than the conductive case (since in the convective envelope the temperature is approximately

constant and equal to T_b), but this effect is similar to a conductive case with a higher T_b. Our two end-member temperature profiles thus capture the possible effects of temperature variations in the mantle of Mercury, under the assumption that there is no partial melting in the mantle.

To model the rheology of the mantle as a function of depth, we divided it into sublayers. Starting from the core-mantle boundary, we divided the mantle in 40-km-thick sublayers, as illustrated in Figure 2.3. For each sublayer the pressure and the temperature at the midpoint were calculated. The complex compliance for each sublayer was obtained with equations (2.5) and (2.6) of Section 2.3.1. The rigidity was calculated with equation (2.9). The viscosity is then given by the expression $\nu = 1/(J_I\omega)$. It is the viscosity of a Maxwell model with the same complex compliance, i.e., with the same rheology. The value of rigidity and viscosity so calculated were taken as representative of the full sublayer.

The Andrade rheological model has been successfully applied to the description of dissipation in rocks, ices, and metals (i.e., *Efroimsky*, 2012, and references therein). The model described in Section 2.3.1 currently represents the best available Andrade model parameterization that incorporates the effects of temperature, pressure, and grain size on the rheology. However the parameters that are kept fixed in the model (listed in Table 2.1) are based on laboratory data on olivine (*Jackson et al.*, 2010). In what follows we apply the Andrade model of Section 2.3.1 to different mineralogical models for the mantle of Mercury. We thus assume that the fixed parameters of olivine can be applied to other minerals. This assumption is not strictly correct, especially for mantle models in which olivine is not the dominant phase, but the broad applicability of the Andrade model to describe materials as chemically and physically different as ices and silicates indicates that the model we use should provide a good description of the

rheology of silicate minerals.

2.5 Assessment of the Rheology of the Outer Solid Shell

The unrelaxed rigidity is a parameter required to characterize the rheology and thus the response to the tidal forcing. Different minerals have different rigidity values, so the mineral assemblages of the mantle and crust determine their rigidities. In this section we assess the impact of the composition on the rigidity of the mantle and the crust. Table 2.2 contains data for minerals that are be used below in modeling the rigidity of the mantle and crust of Mercury. In addition, we describe our assumptions in modeling the response of the FeS layer.

2.5.1 Mineralogical Models for the Mantle

For the mineralogy of the mantle, we use the works of *Rivoldini et al.* (2009) and *Malavergne et al.* (2010) as references. *Malavergne et al.* (2010) calculated the expected mineralogy of the mantle of Mercury as a function of pressure, given two different assumed bulk compositions for the whole planet, an enstatite chondrite (EH) and a Bencubbin-like chondrite (CB). The EH chondrite provides a good compositional and mineralogical match to the data of the X-Ray Spectrometer (XRS) on MESSENGER (*Weider et al.*, 2012), which are compatible with the data from the Gamma-Ray Spectrometer (GRS) (*Evans et al.*, 2012). The XRS and the GRS are sensitive to the top tens of micrometers and centimeters of near-surface material, respectively, and the consistency between the results of the two instruments indicates that the top tens of centimeters of Mercury's regolith are vertically homogeneous (*Evans et al.*, 2012). Despite the apparent good agreement between XRS and GRS results and enstatite chondrite compositions, the

Table 2.2: Minerals Relevant to the Mantle and Crust of Mercury[a].

	Abbr.	ρ_0 [kg/m^3]	μ_0 [GPa]	$\mu'_P\|_0$	$\mu'_T\|_0$ [GPa/K]
Garnet	Grt	$3565+760\chi_{Fe}$	$92+7\chi_{Fe}$	1.4	-0.010
Orthopyroxene	Opx	$3194+799\chi_{Fe}$	$78+10\chi_{Fe}$	1.6	-0.012
Clinopyroxene	Cpx	$3277+380\chi_{Fe}$	$67-6\chi_{Fe}$	1.7	-0.010
Quartz	Qtz	2650	44.5	0.4	-0.001
Spinel	Spl	$3580+700\chi_{Fe}$	$108-24\chi_{Fe}$	0.5	-0.009
Plagioclase	Pl	2750	40.4	2.5	-0.002
Merwinite	Mw	3330	81	1.4	-0.014
Olivine	Ol	$3222+1182\chi_{Fe}$	$81-31\chi_{Fe}$	1.4	-0.014

[a] Notes: Abbr. denotes mineral abbreviation (*Siivola and Schmid*, 2007). A subscript "0" indicates standard ambient temperature and pressure ($298\,\mathrm{K}, 10^5\,\mathrm{Pa}$). Density is ρ. μ, μ'_P, and μ'_T are the rigidity and its pressure and temperature derivatives, respectively. χ_{Fe} is the mole fraction of iron. Data in this table are taken from the compilations of *Sobolev and Babeyko* (1994), *Vacher et al.* (1998), *Cammarano et al.* (2003), *Verhoeven et al.* (2005), and *Rivoldini et al.* (2009).

metal fraction in EH chondrites is lower than the bulk value for Mercury. The CB chondrites analyzed by *Malavergne et al.* (2010) have a higher metallic component, and thus might represent another possible building block for Mercury. *Rivoldini et al.* (2009) calculated the expected mineralogy for a set of five models of the mantle of Mercury. These included: an enstatite chondrite model (EC), similar to the EH case of *Malavergne et al.* (2010); a model in which the building blocks for Mercury are matched compositionally by the chondrules of two metal-rich chondrites (MC) (*Taylor and Scott*, 2005); a model based on fractionation

processes in the solar nebula (MA) (*Morgan and Anders*, 1980); the refractory-volatile model (TS) of *Taylor and Scott* (2005); and the evaporation model of *Fegley and Cameron* (1987). The latter is not consistent with the high abundance of sulfur, potassium, and sodium in Mercury's surface materials (*Nittler et al.*, 2011; *Peplowski et al.*, 2012; *Evans et al.*, 2012). We used the composition of these six models to estimate a range for the rigidity of the mantle of Mercury. The mineralogical composition of these models is listed in Table 2.3.

2.5.2 Rigidity of the Mantle

MESSENGER confirmed that the surface of Mercury has an extremely low iron abundance (*Nittler et al.*, 2011; *Evans et al.*, 2012) and showed that a substantial fraction of the surface is volcanic in origin (*Denevi et al.*, 2013). The low surface abundance of FeO is an indication that the source regions of volcanic material are also FeO poor, since FeO does not undergo major fractionation during partial melting (*Taylor and Scott*, 2005). However, under the highly reducing conditions inferred for Mercury, part of the iron in the silicate shell is present as sulfides and metal (*Zolotov et al.*, 2013). In calculating the rigidity of the mantle, we assume that the silicate minerals contain no iron. In other words we assume that $\chi_{\mathrm{Fe}} = 0$ in Table 2.2. The effects of small amounts of iron-rich minerals are small compared with the uncertainties introduced by the unknown mineralogy of the mantle of Mercury. It should be noted, however, that at least for olivine the rheological properties show a strong dependence on the iron content (*Zhao et al.*, 2009).

For each mineralogical model of the mantle in Table 2.3 we calculate the composite rigidity at the reference conditions of $T_{\mathrm{R}} = 1173$ K and $P_{\mathrm{R}} = 0.2$ GPa, required for the Andrade model [equation (2.7)]. First, for each mineral

Table 2.3: Mineralogical models for the Mantle of Mercury.[a]

Model	Grt	Opx	Cpx	Qtz	Spl	Pl	Mw	Ol	μ_c [GPa]
CB	–	66	4	22	4	4	–	–	59
EH	–	78	2	8	–	12	–	–	65
MA	23	32	15	–	–	–	–	30	69
TS	25	–	–	–	8	–	2	65	71
MC	15	50	9	–	–	–	–	26	68
EC	1	75	7	17	–	–	–	–	60

[a] Notes: Two capital letters identify the model (details in section 2.5.1). CB and EH: *Malavergne et al.* (2010). MA: *Morgan and Anders* (1980). TS and MC: *Taylor and Scott* (2005). EC: *Wasson* (1988). The central part of the table gives the mineralogical content in terms of the vol.% of its components (after *Malavergne et al.* (2010) and *Rivoldini et al.* (2009)). Mineral abbreviations are defined in Table 2.2. A dash indicates that the mineral is absent. The composite rigidity μ_c is evaluated as the Hill rigidity at $T = 1173$ K and $P = 0.2$ GPa.

the rigidity at $T_{\rm R}$ and $P_{\rm R}$ is obtained from the parameters in Table 2.2 with the expression

$$\mu_{\rm U}(T_{\rm R}, P_{\rm R}) = \left[\mu_0 + (T - T_{\rm R})\frac{d\mu}{dT} + (P - P_{\rm R})\frac{d\mu}{dP}\right]. \qquad (2.11)$$

The composite rigidity is obtained with Hill's expression, which is an average between the Reuss and the Voigt rigidities (*Watt et al.*, 1976). Table 2.3 lists the composite rigidities so derived for the mantle models. The range is $59 - 71$ GPa.

2.5.3 Rigidity and Viscosity of the Crust

The surface of Mercury presents a compositional and morphological dichotomy between the younger smooth plains (SP) and the older intercrater plains and heavily cratered terrain (IcP-HCT) (*Peplowski et al.*, 2012; *Weider et al.*, 2012). The majority of the SP, which cover $\sim 27\%$ of the surface of Mercury, are volcanic in origin (*Denevi et al.*, 2013). From the surface compositional data returned by MESSENGER, *Stockstill-Cahill et al.* (2012) modeled the expected mineralogy of the IcP-HCT and the northern volcanic plains (NVP). The NVP are a large contiguous area of volcanic smooth plains (*Head et al.*, 2011) that show similar composition to other smooth plains (i.e., Caloris basin interior) (*Weider et al.*, 2012). Therefore the mineralogy of the NVP can be taken as representative of other smooth plains areas. The results of *Stockstill-Cahill et al.* (2012) are summarized in Table 2.4. The table also includes the mineralogy for smooth plains when the effect of uncertainties in the Na abundance are taken into account (SP_{Na}). These three mineralogies are used to estimate the rigidity of the crust of Mercury.

Variations in the temperature and pressure of the crust with depth have negligible effects on the rigidities of the individual minerals. Therefore the composite rigidity is obtained with Hill's expression using μ_0 (Table 2.2) as the rigidity for each mineral.

The range in crustal rigidity is $51 - 60$ GPa, and will likely encompass the actual rigidity of the crust if the IcP-HCT represents the older crust and the SP are representative of the younger crust produced by the most recent widespread episodes of partial melting of the mantle. We use the central value of 55 GPa as the rigidity of the crust. Its viscosity is set at 10^{23} Pa s. This choice is not critical since the crust is cold and responds elastically at the forcing frequency of

Table 2.4: Composition and Rigidity of the Crust of Mercury.[a]

Model	Ol	Opx	Pl	Spl	Qz	μ_c (GPa)
SP	2	44	26	6	22	53-58
SP_{Na}	8	30	57	5	–	51-53
IcP-HCT	2	59	29	1	9	57-60

[a] Notes: "Model" column: SP stands for smooth plains, and IcP-HCT stands for intercrater plains and heavily cratered terrain. SP_{Na} takes into account the difference that might arise with a different Na abundance (see *Stockstill-Cahill et al.*, 2012). The central part of the table gives the mineralogical composition in weight percent. In the last column the composite rigidity is calculated with Hill's expression. The range in μ_c for each model is given by the different amounts of end-members (i.e., forsterite and fayalite in the olivine solid-solution series).

the tide.

2.5.4 Rheology of the FeS layer

The procedure used to calculate the rigidity of the mantle minerals cannot be used for the FeS layer because of a lack of laboratory data. At the relevant pressures and temperatures of the outer core of Mercury, the FeS would be in the

FeS V phase (*Fei et al.*, 1995). For FeS V the bulk modulus and its pressure and temperature derivatives have been measured (*Urakawa et al.*, 2004). There is no rigidity determination, however. Even the rigidity of troilite (or FeS I, the phase at standard pressure and temperature) has never been measured (*Hofmeister and Mao*, 2003). Nevertheless, an argument illustrated by *Hofmeister and Mao* (2003, see their Figure 7) sets $\mu_{\mathrm{FeS\,I}} = 31.5$ GPa. From the phase diagram of FeS (*Fei et al.*, 1995), the conditions at the base of the mantle ($P \sim 5.5$ GPa) are close to the melting curve for FeS V. The corresponding homologous temperature T_{H}, the ratio of the temperature of the material to the solidus temperature, is $T_{\mathrm{H}} > 0.85$. It is often assumed that the viscosity is proportional to the exponential of the inverse of the homologous temperature (e.g., *Borch and Green II*, 1987). Therefore the viscosity of the FeS layer at the top of the core would be close to the low viscosity of the melt. These considerations indicate that the FeS layer, if present, is weak.

We consider the effects of the FeS layer only in the cold-mantle case ($T_{\mathrm{b}} = 1600$ K), since for higher temperatures the FeS would be liquid (see the phase diagram in *Fei et al.*, 1995). We assume that the FeS will have the same rheological properties as the base of the mantle. This assumption is conservative because at $T = 1600$ K the T_{H} of FeS is larger than T_{H} of the silicates and, from the value of $\mu_{\mathrm{FeS\,I}}$, the unrelaxed rigidity of FeS V is likely to be smaller than that for the silicates.

2.6 Results: Tidal Response and Interior Properties

The results illustrated below show that models of Mercury with a liquid outer core have $k_2 \gtrsim 0.3$. For a completely solid model of Mercury (i.e., a model devoid of a liquid outer core), the value of k_2 would be reduced by approximately

an order of magnitude. Given this variation in the magnitude of k_2 between a completely solid interior and one with a liquid (outer) core, a measurement of the tidal response would provide a confirmation of the presence of a liquid (outer) core. Its existence has already been inferred from Earth-based radar measurements (*Margot et al.*, 2007) and also from the interpretation of the magnetic field detected by the MESSENGER Magnetometer (*Anderson et al.*, 2012). Therefore the results presented below focus on the models of Mercury with a liquid (outer) core that have been described in section 2.4.

2.6.1 The Main Parameters Controlling the Tidal Deformation

The tidal response of Mercury is largely controlled by the strength and thickness of the outer solid shell (OSS), much like the similar case for Europa's ice shell (*Moore and Schubert*, 2000). This result is a consequence of the presence of a liquid (outer) core, which decouples the shell from the deformation of the deeper interior. Due to the combined mass and moments of inertia constraints, the thickness of the OSS depends on the density of the core. This outcome is shown in the left panel of Figure 2.4, where the tradeoff between core density and liquid core radius (i.e., OSS thickness) is seen in the color scale that strongly correlates both with the radius of the liquid core and k_2. For these models, $\mu_{\mathrm{U}} = 65$ GPa and $T_{\mathrm{b}} = 1725$ K. A modification of the rheological properties of the OSS, through a variation of the temperature at the base of the mantle T_{b} and/or of the unrelaxed rigidity μ_{U}, would modify the response as indicated by the arrows in the figure. Note, however, that there is only a weak dependence on the density of the OSS itself, as seen in the right panel of Figure 2.4, where the colors show the density of the OSS and span nearly the entire range of the response. The small effects of a solid inner core on the tidal response are discussed in Appendix C.

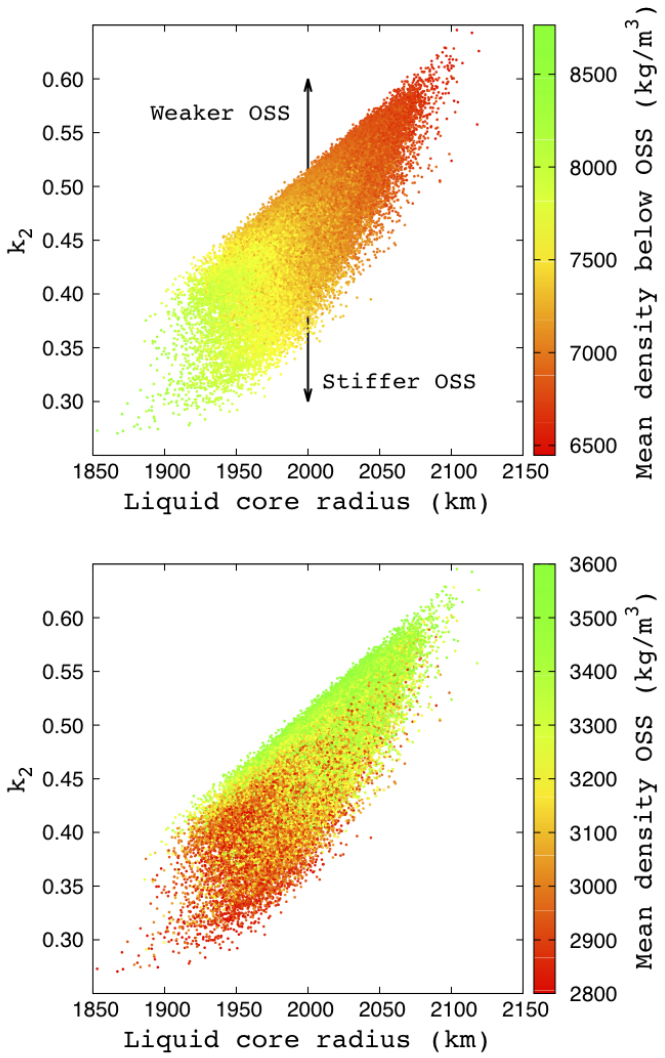

Figure 2.4: k_2 as a function of the radius of the liquid core for the NoFeS set. For these data the temperature at the base of the core is $T_\mathrm{b} = 1725$ K and the mantle unrelaxed rigidity is $\mu_\mathrm{U} = 65$ GPa. Top: Colors indicate the mean density of material below the outer solid shell (OSS). The arrows indicate how the data points would shift with a change in the rheological properties of the OSS. Bottom: Same as for the top panel, but here colors indicate the mean density of the OSS.

The same set of models used in Figure 2.4 are shown in Figure 2.5 in the form of a plot showing how the compatible models (section 2.4) are distributed.

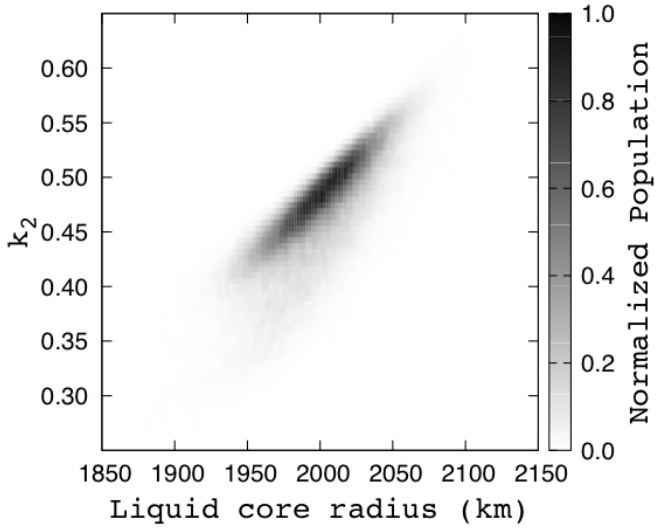

Figure 2.5: Same data as in Figure 2.4, here plotted using the normalized population based on the C and $C_{\rm m}$ determinations.

The availability for Mercury of the three constraints ρ, C, and $C_{\rm m}$ results in a distribution of the data that is relatively narrow, which makes the determination of k_2 in principle very useful. It has the potential for improving the determination of the location of the radius of the outer liquid core and the mean density of the material below the outer solid shell, and of providing insights into the rheological properties (temperature and rigidity) of the outer solid shell. This improved knowledge will depend both on the precision of the k_2 determination and on the effects of the uncertainties in the temperature and rigidity of the outer solid shell.

2.6.2 Effects of the Mantle Rheology on the Tidal Response

In our models the rheology of the outer shell is controlled by the temperature at the base of the mantle $T_{\rm b}$ and the unrelaxed rigidity of the mantle $\mu_{\rm U}$. Figure 2.6

illustrates the effects on the tidal response of a variation in T_b between 1600 K and 1850 K. For this case we assumed an unrelaxed mantle rigidity of $\mu_U = 65$ GPa. As expected, on the basis of the influence of temperature on rheology (Figure 2.1), a higher T_b corresponds to a weaker outer solid shell, which in turn has a larger tidal response. In terms of the central values of the model populations, k_2 varies in the range $0.47 - 0.50$.

Basal mantle temperature and unrelaxed rigidity have similar, if opposite, effects on the tidal response, which is enhanced by a higher T_b and/or lower μ_U and is diminished by a lower T_b and/or higher μ_U. Therefore, there is a tradeoff between these two parameters. The full range of tidal responses for the NoFeS models is illustrated in Figure 2.7. The variation in k_2 is in the range $0.45 - 0.52$, the former value corresponding to the stiff mantle ($T_b = 1600$ K and $\mu_U = 71$ GPa) and the latter to the weak mantle ($T_b = 1850$ K and $\mu_U = 59$ GPa). The values of μ_U that we use, 59 GPa and 71 GPa, represent the largest and smallest values derived from the mantle mineralogies analyzed in section 2.5.1 and listed in Table 2.3.

A solid FeS layer can exist only in the $T_b = 1600$ K case (Section 2.5.4). Under the assumptions for the rheology of solid FeS at the base of the mantle of Mercury described in Section 2.5.4, we tested for the effect of the presence of an FeS layer on the tidal response for the case of $T_b = 1600$ K. Results are shown in Figure 2.8. The effect of the weak FeS layer is to increase the tidal response. In other words, it has the same effect as a higher T_b or a lower μ_U. In terms of the central k_2 values of the model populations, the presence of the FeS layer increases the tidal response by $\sim 6\%$.

The models presented are for a mantle grain size $d = 1$ cm. A smaller grain size, $d = 1$ mm, corresponds to a more dissipative rheology, which induces a larger

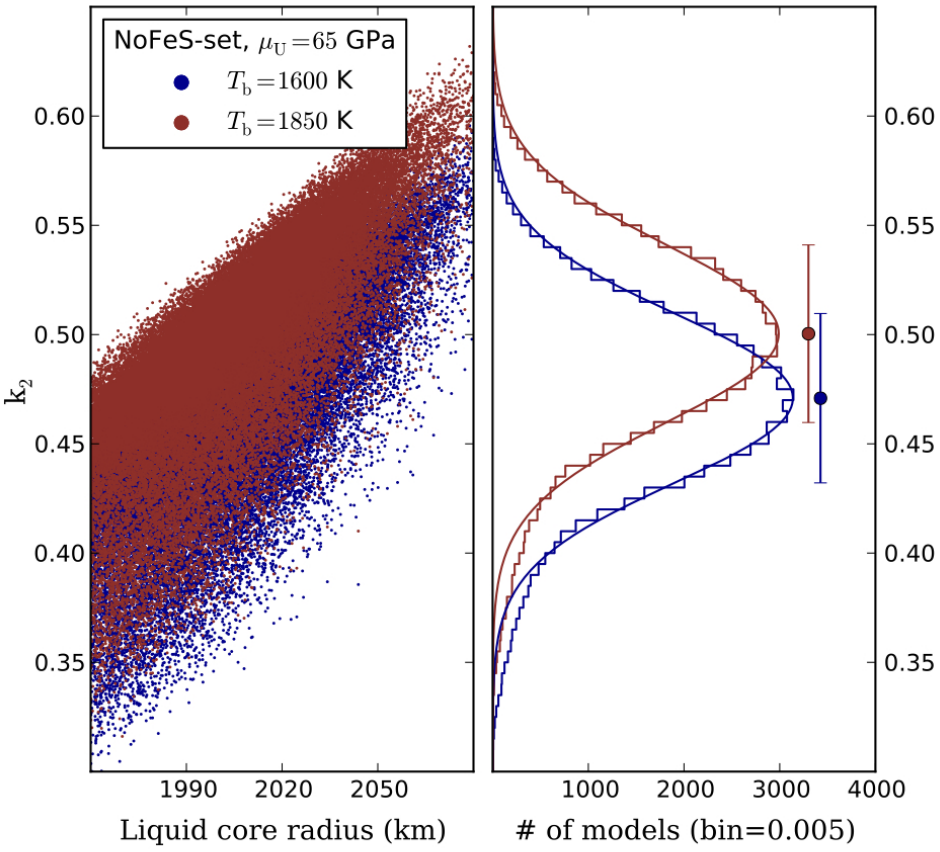

Figure 2.6: Effect of the mantle basal temperature on the tidal response. Predicted values of k_2 for models with unrelaxed rigidity $\mu_U = 65$ GPa and two different values of temperature at the base of the mantle $T_b = 1600$ K (dark blue) and $T_b = 1850$ K (brown). Left: k_2 as a function of the radius of the liquid core. Right: histogram of k_2 for the two sets of models.

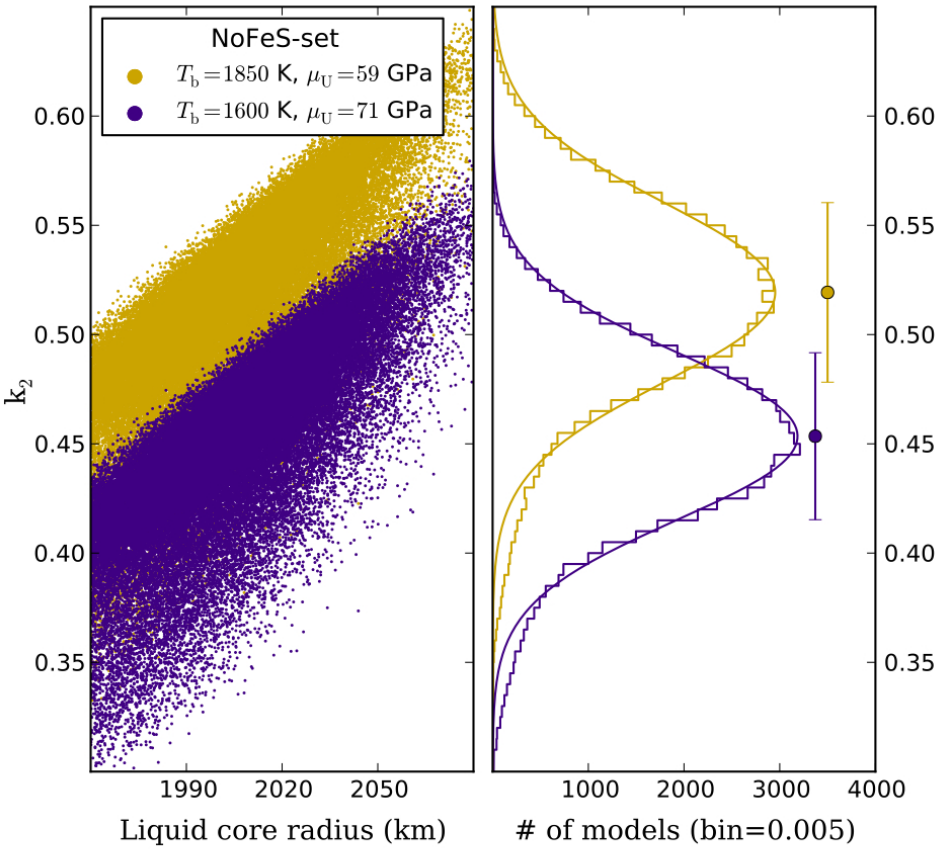

Figure 2.7: Predicted values of k_2 for the two end-member NoFeS sets of models. Golden: weak outer solid shell with mantle basal temperature T_b = 1850 K and unrelaxed rigidity μ_U = 59 GPa. Indigo: stiff outer solid shell with T_b = 1600 K and μ_U = 71 GPa. Left: k_2 as a function of the radius of the liquid core. Right: histogram of k_2 for the two sets of models.

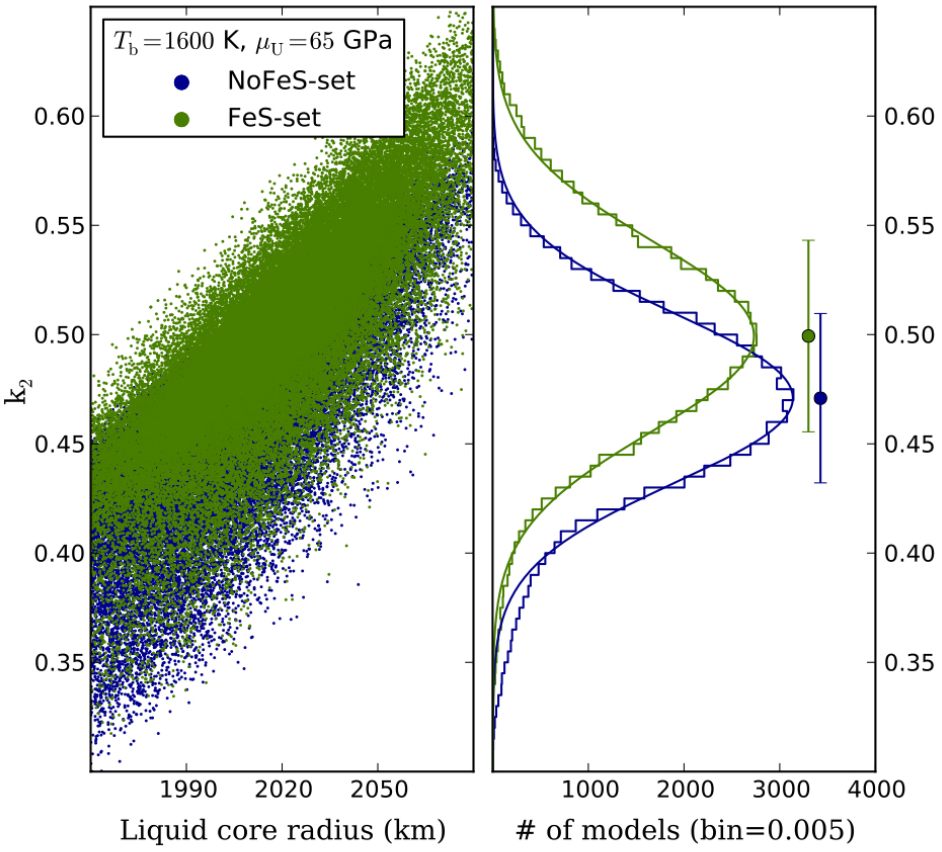

Figure 2.8: Effect of a solid FeS layer on the tidal response. Predicted values of k_2 for models with mantle basal temperature $T_b = 1600$ K and unrelaxed mantle rigidity $\mu_U = 65$ GPa, with (green) and without (dark blue) an FeS layer at the base of the mantle. Left: k_2 as a function of the radius of the liquid core. Right: histogram of k_2 for the two sets of models.

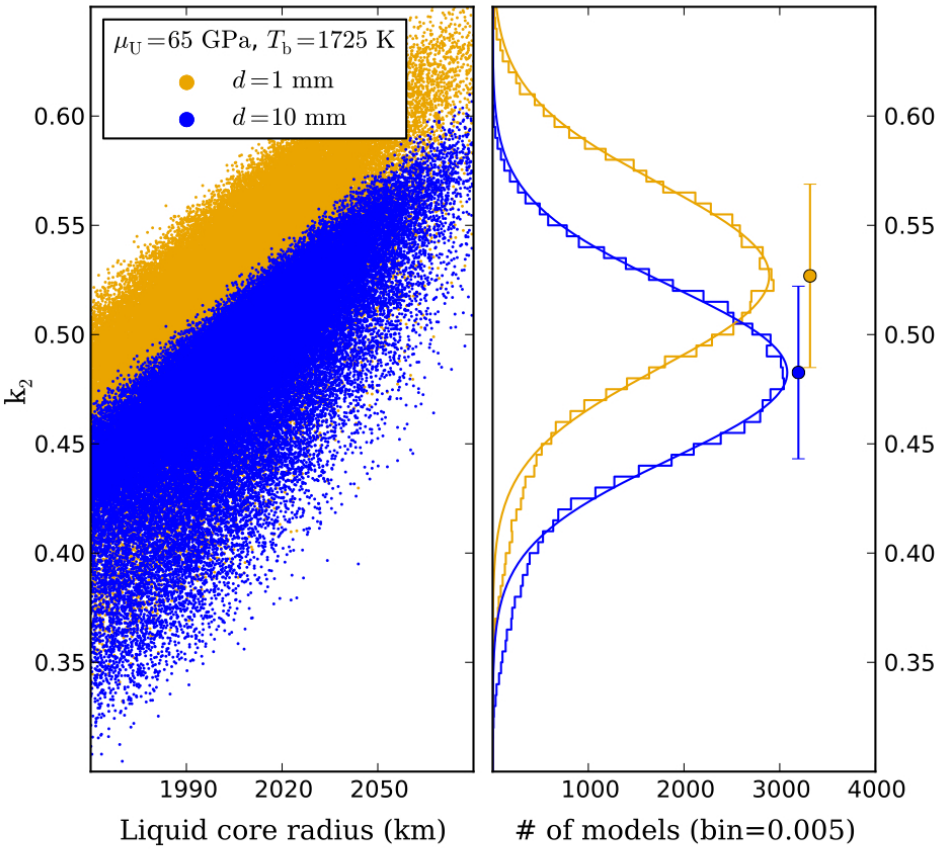

Figure 2.9: Predicted values of k_2 for two sets of NoFeS models with the same mantle basal temperature $T_b = 1725$ K and the same mantle unrelaxed rigidity $\mu_U = 59$ GPa. The two sets differ in the assumed mantle grain size d. Blue: $d = 1$ cm. Orange: $d = 1$ mm. Left: k_2 as a function of the radius of the liquid core. Right: histogram of k_2 for the two sets of models.

tidal response. This effect is illustrated in Figure 2.9 . The effect is substantial, since in this case k_2 varies between 0.48 and 0.52, a larger range than the one resulting from the variation of $T_{\rm b}$ illustrated in Figure 2.6.

2.7 Summary and Conclusions

We performed simulations of the tidal response of Mercury, as parameterized by the tidal Love number k_2, for two sets of models of Mercury that are compatible with the currently available constraints on the interior structure of the planet, i.e., the mean density ρ, the moment of inertia C, and the moment of inertia of the outer solid shell $C_{\rm m}$. The two sets of models differ in the presence or absence of a solid FeS layer at the top of the core (section 2.4). The response of the materials is modeled with viscoelastic rheologies (section 2.3.1). The Maxwell rheological model is used for the crust, the liquid outer core, and the solid inner core. The Andrade rheological model is used for the mantle, where the high temperature and relatively low pressure induce large non-elastic effects (Figure 2.1 and Table 2.1). For the FeS layer we assumed an Andrade rheology that matches the basal mantle layer. We investigated the effects on the tidal response of the unknown mantle mineralogy (which determines the unrelaxed rigidity $\mu_{\rm U}$), temperature profile in the outer solid shell (controlled by the mantle basal temperature $T_{\rm b}$), and mantle grain size.

The main findings of the paper can be summarized as follows:

1. The presence of a liquid outer core makes the value of k_2 dependent mainly on three parameters: the radius of the liquid core (Figure 2.5), the mean density of material below the outer solid shell (Figure 2.4, left panel), and the rheology of the outer solid shell (Figures 2.6 to 2.9). Since the first two

have been determined with a precision of better than 5% from ρ, C, and $C_{\rm m}$ (*Hauck et al.*, 2013; *Rivoldini and Van Hoolst*, 2013), a measurement of k_2 is informative with regard to the rheology of the outer solid shell;

2. With available estimates for the temperature at the base of the mantle $T_{\rm b}$ (*Rivoldini and Van Hoolst*, 2013; *Tosi et al.*, 2013), for an unrelaxed rigidity $\mu_{\rm U}$ of the mantle appropriate for mineralogical models compatible with MESSENGER observations (Table 2.3), and with a mantle grain size $d =$ 1 cm, we find that for the NoFeS-set k_2 varies in the range $0.45 - 0.52$. This range is expressed in terms of the central values of the model populations shown in the right panel of Figure 2.7 and corresponds to models with $(T_{\rm b}, \mu_{\rm U}) = (1600\ {\rm K}, 71\ {\rm GPa})$ and $(T_{\rm b}, \mu_{\rm U}) = (1850\ {\rm K}, 59\ {\rm GPa})$, respectively. An order of magnitude reduction in the grain size would result in a $\gtrsim 10\%$ increase in the tidal response (Figure 2.9);

3. The presence of a solid FeS layer is possible only if $T_{\rm b} \lesssim 1600$ K (Section 2.5.4). Its effect is to increase the tidal response by $\sim 6\%$ (Figure 2.8). This result is obtained under the conservative assumption that the FeS layer has the same rheological properties as the base of the mantle (Section 2.5.4). The solid FeS may be weaker, in which case its effect would be larger than the estimate shown in Figure 2.8.

The possibility of improving our understanding of the interior of Mercury through the interpretation of a measurement of k_2 depends on the precision of the determination obtained by the radio tracking of the MESSENGER spacecraft (or BepiColombo in the future), and on the uncertainties in the parameters that affect the tidal response of the planet.

As mentioned in section 2.3, the highly eccentric orbit of MESSENGER makes

the determination of k_2 very challenging. Nevertheless, there are indications that the solution will converge to a value of $\sim 0.45 \pm 0.05$ (*Mazarico et al.*, 2014a). If confirmed, such a result would fall in the lower range of our model responses. With the preliminary estimate of $k_2 = 0.45$, Figures 2.6 to 2.8 suggest that a cold mantle model, without an FeS layer, is preferred. For the results presented in these figures a mantle grain size $d = 1$ cm was assumed, a value compatible with the estimated grain size for the mantles of the Moon and Mars (*Nimmo et al.*, 2012; *Nimmo and Faul*, 2013). A smaller grain size would result in an increased tidal deformation (Figure 2.9) and would strengthen the preference for a cold mantle model, without and FeS layer. Nevertheless, the uncertainties associated both with the k_2 determination and with the modeled distributions are too large to make a conclusive statement.

Future improvements in the interpretation of k_2 can be expected. Our modeling of the tidal response would benefit from improvements in the mineralogical models of the silicate part (which would reduce the range in the unrelaxed rigidity μ_{U}). No meteorites from Mercury have yet been identified, and there are currently no plans for a lander or sample return mission to Mercury, so improvements in compositional models will be based on additional remote sensing measurements, cosmochemical analogues, experimental petrological observations (e.g., *McCoy et al.*, 1999; *Charlier et al.*, 2013), and numerical simulations (e.g., *Stockstill-Cahill et al.*, 2012). Updates in the estimates of the amount of global contraction of Mercury will inform thermal history models, which in turn put constraints on the basal mantle temperature (e.g., *Tosi et al.*, 2013).

CHAPTER 3

Updates on the tides of Mercury

The discussion section in our paper on the modeling of the tides of Mercury (section 2.7) was based on the preliminary determination of the k_2 of the planet reported in *Mazarico et al.* (2014b), $k_2 = 0.45 \pm 0.05$. An official estimate based on the analysis of three years of radio tracking data from the MESSENGER spacecraft has been subsequently published in *Mazarico et al.* (2014a). A "preliminary value" of k_2 of 0.451 ± 0.014, which would correspond to an uncertainty of $\sim 3\%$, is reported in the abstract of *Mazarico et al.* (2014a). We refer to this estimate as Abstract Value (AV). However, in the main body of the article, it is stated that "accounting for possible systematic effects and biases, a wider range of $k_2 = 0.43 - 0.50$ can thus not be ruled out", which corresponds to an uncertainty of $\sim 7.5\%$. We refer to this estimate as Text Value (TV). In light of this new estimate(s) of k_2 we reassess the conclusions of section 2.7.

3.1 k_2 and the rheology of the mantle

In Figure 3.1 we illustrate the trade-off between temperature and rigidity of the mantle in the tidal response for the NoFeS models. In the left panel we show the effect of mantle basal temperature on the value of k_2 for the stiff mantle case ($\mu = 71$ GPa, see Table 2.3). In the right panel we show the effect of the mantle rigidity on the value of k_2 for the cold mantle case ($T_\mathrm{b} = 1600$ K). The AV

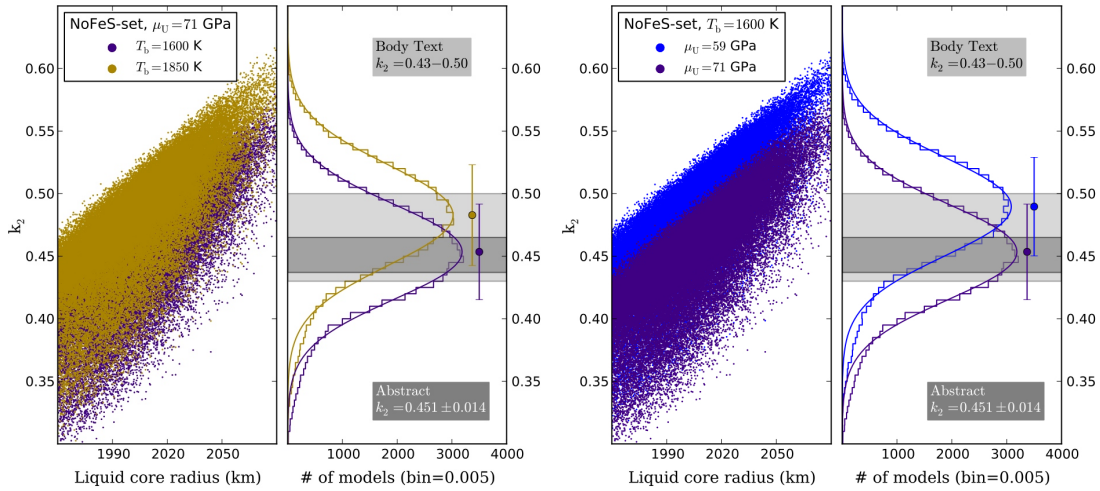

Figure 3.1: (Left) Predicted values of k_2 for two sets of models with the same mantle rigidity (μ_U = 71 GPa) and different mantle basal temperature T_b. Golden: T_b = 1850 K. Indigo: T_b = 1600 K. (Right) Predicted values of k_2 for two sets of models with the same mantle basal temperature (T_b = 1600 K) and different mantle rigidity μ_U. Indigo: μ_U = 71 GPa. Blue: μ_U = 59 GPa. The values of k_2 reported in the abstract and body text of *Mazarico et al.* (2014a) are shown.

estimate (dark gray band) suggests a better match to the cold and stiff mantle case, even if it is also partially compatible both with a hot and stiff mantle (golden curve) and a weak and cold mantle (blue curve). However, when the TV estimate (light gray band) is considered, it is clear that a measurement of k_2 uncertain at the 7.5% level is not able to discriminate between temperature and rigidity effects.

3.2 k_2 and the presence of a solid FeS layer

In Figure 3.2 we show again the effect on the value of k_2 of the presence of a solid FeS layer for a mantle basal temperature T_b = 1600 K and an unrelaxed

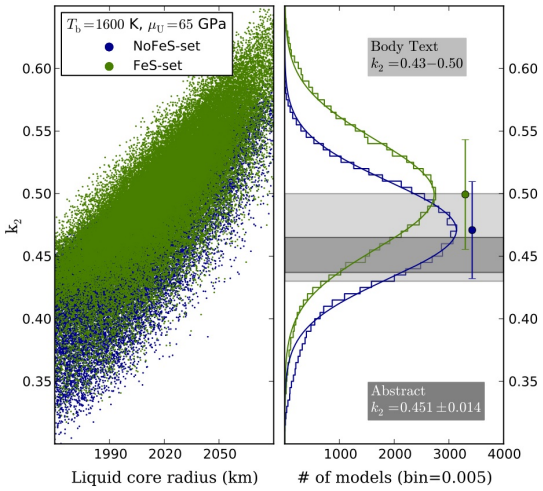

Figure 3.2: Effect of a solid FeS layer on the tidal response. Predicted values of k_2 for models with mantle basal temperature $T_b = 1600$ K and unrelaxed mantle rigidity $\mu_U = 65$ GPa, with (green) and without (dark blue) an FeS layer at the base of the mantle. Left: k_2 as a function of the radius of the liquid core. Right: histogram of k_2 for the two sets of models. The values of k_2 as reported in the abstract and body text of *Mazarico et al.* (2014a) are shown.

mantle rigidity $\mu_U = 65$ GPa. A lower bound of $T_b = 1600$ K for the basal mantle temperature has been obtained independently and with different methods by *Tosi et al.* (2013) and *Rivoldini and Van Hoolst* (2013). Since the FeS layer can be present only if $T_b \lesssim 1600$ K, in considering the possible presence of the FeS layer the temperature is fixed at $T_b = 1600$ K. We model the rheology of the FeS layer under very conservative assumptions (section 2.5.4), and the mean value of the histogram for the FeS set would shift upwards with less conservative assumptions. The AV estimate of *Mazarico et al.* (2014a) is then indicative of a standard silicate mantle, without an FeS layer. However, the TV estimate is partially compatible with an FeS layer at the bottom of the mantle.

3.3 Conclusions

The comparison of our models with the estimates of k_2 presented in *Mazarico et al.* (2014a) highlights the informative potential of an accurate measurement of k_2. The expected accuracy in the k_2 determination as obtained by the ESA's BepiColombo mission to Mercury (scheduled to be launched in July 2016) is better than 1% (*Milani et al.*, 2001). If this expectation is met the European mission will have the potential to make an important contribution to the understanding of the interior of Mercury.

CHAPTER 4

Thickness of the crust of Mercury from geoid-to-topography ratios

To gain insight into the thickness of the crust of Mercury we use gravity and topography data acquired by the MESSENGER spacecraft to calculate geoid-to-topography ratios over the northern hemisphere of the planet. For an Airy model for isostatic compensation of variations in topography, we infer an average crustal thickness of 35 ± 18 km. Combined with the value of the radius of the core of Mercury, this crustal thickness implies that Mercury had the highest efficiency of crustal production among the terrestrial planets. From the measured abundance of heat-producing elements on the surface we calculate that the heat production in the mantle from long-lived radioactive elements 4.45 Ga ago was greater than 5.4×10^{-12} W/kg. By analogy with the Moon, the relatively thin crust of Mercury allows for the possibility that major impact events, such as the one that formed the Caloris basin, excavated material from Mercury's mantle.

4.1 Introduction

Planetary crusts are formed and shaped during major igneous events such as magma ocean solidification and large-scale volcanism. These processes affect the thermo-chemical evolution of the interior through a number of processes (e.g.,

Elkins-Tanton, 2012), including the partitioning of incompatible heat-producing elements, which during episodes of partial melting concentrate into the melt and accumulate in the crust; the modification of the bulk volatile content, given that volatile elements in near-surface magmas tend to escape to the atmosphere; and the modification of the internal temperature profile by the transport of hot material from the deep interior to shallow depths. Characterization of the crust thus provides information on the origin, differentiation, and subsequent geologic evolution of a planetary body. For Mercury, in particular, the crust may hold clues to the still poorly understood processes of formation of this planet.

There have been a number of attempts to constrain the thickness of the crust of Mercury. *Anderson et al.* (1996) compared the magnitude of the spherical harmonic second-degree sectorial gravitational coefficient C_{22} obtained by radio tracking of the Mariner 10 spacecraft with the value inferred from the equatorial ellipticity in elevation, measured with Earth-based radar observations, and concluded that the topography of Mercury at degree 2 is compensated. Under the assumption of Airy isostasy, they inferred that the thickness of the crust lies in the range 100 to 300 km.

Lobate scarps observed on the surface of Mercury are interpreted to be the surface manifestations of large thrust faults (e.g., *Strom et al.*, 1975). Topographic profiles across thrust faults constrain the deepest extent of faulting to be 35 to 40 km (*Watters et al.*, 2002). By analogy with thermal limits to brittle behavior on Earth, the depth of faulting provides a constraint on the subsurface thermal structure, and therefore heat flux, at the time of fault formation (*Nimmo*, 2002; *Watters et al.*, 2002). Combining this information with a model for the viscous relaxation of topography and its compensation at the crust-mantle boundary constrains the crustal thickness to be < 200 km (*Nimmo*, 2002). This

value is an upper bound since it was obtained without taking into account the secular cooling of the planet, which would increase the estimate of early heat flux and thereby reduce the maximum thickness of the crust (*Nimmo*, 2002).

Nimmo and Watters (2004) inferred an upper limit of 140 km on the crustal thickness by combining the inferred maximum depth of faulting with the requirement that the base of the crust does not remelt. The latter requirement was enforced by using a reference melting temperature for crustal materials of 1800 K. For a more likely value of 1500 K, the upper bound on the crustal thickness would be about 90 km (*Nimmo and Watters*, 2004).

A joint analysis of gravity and topography data can be used to characterize the subsurface structure of rocky planets (e.g., *Wieczorek*, 2007). *Smith et al.* (2012) combined the gravity and topography of Mercury measured by the MErcury, Surface, Space ENvironment, GEochemistry, and Ranging (MESSENGER) spacecraft to produce a map of crustal thickness for the northern hemisphere. This map was obtained with an assumed value for the mean crustal thickness, and the uncertainty in this mean value represents the largest uncertainty in the model (*Smith et al.*, 2012). In this work we calculate spatially localized geoid-to-topography ratios (GTRs) over the surface of Mercury and interpret these ratios with the method of spectrally weighted admittances (*Wieczorek and Phillips*, 1997). This method has been previously applied to infer the thickness of the crust of the Moon (*Wieczorek and Phillips*, 1997; *Wieczorek et al.*, 2006), Mars (*Wieczorek and Zuber*, 2004), and Venus (*James et al.*, 2013).

4.2 Data and Methods

We calculated the geoid of Mercury from the spherical harmonic model HgM005 for the gravitational potential, a model complete to degree and order 50 (*Mazarico et al.*, 2014a). The shape of the planet was obtained from a spherical harmonic model of the topography (*Neumann*, 2014). Since the analysis used here is based on the relation between gravity and topography, the topographic expansion was truncated at the same degree as the geoid.

We computed the value of the geoid N and topography h over a global grid with a constant spacing of about $1.5° \times 1.5°$, resulting in almost 20300 grid points. Both the geoid heights and surface topography were referenced to the same radius, which we chose to be the mean planetary radius $R = 2440$ km, and the geoid was calculated from Brun's equation, which is a first-order approximation that gives rise to an error of less than 1 m for Mercury (*Wieczorek*, 2007, 2015). The GTRs for each grid point were computed from regressions of geoid and topography data within spherical caps of radius r according to the equation

$$N = \mathrm{GTR}\, h + b_0, \tag{4.1}$$

where b_0 is a constant. Our results are insensitive to variations in cap radius from $r = 1250$ km to $r = 2000$ km, though the uncertainty in the GTR from the regression decreases with increasing cap dimension. From the tradeoff between spatial resolution and GTR uncertainty, $r = 2000$ km is our preferred choice for the radius of the spherical cap. If the geoid signal were due only to lateral variations in the thickness of a crust of constant density, the b_0 term in equation (4.1) would be zero if all elevations were referenced to the mean planetary radius. A non-zero b_0 is included to account for possible contributions from regional variations in crustal density, density anomalies in the mantle, or spherical harmonic

degree 1 topography (which does not have an expression in the geoid in coordinates for which the origin is at the center of mass). With different statistical tests (adjusted coefficient of determination, F–test, and Akaike information criterion; see, e.g., *Feigelson and Babu* (2012)) we established that a two-parameter model (GTR and b_0) is to be preferred over a one-parameter model with $b_0 = 0$.

The calculated GTR is interpreted in the framework of spectrally-weighted admittances (*Wieczorek and Phillips*, 1997). If the GTR is spatially stationary over the analyzed region, it can be expressed as

$$\mathrm{GTR} = \sum_{\mathrm{l_{min}}}^{\mathrm{l_{max}}} W_{\mathrm{l}} Z_{\mathrm{l}}, \tag{4.2}$$

where W_{l} is a weighting function that depends on the topographic power spectrum and is given by

$$W_{\mathrm{l}} = \frac{S_{\mathrm{hh}}(l)}{\sum_{\mathrm{l_{min}}}^{\mathrm{l_{max}}} S_{\mathrm{hh}}(l)}, \tag{4.3}$$

and where S_{hh} is the topographic power at degree l. Z_{l} is a degree-dependent admittance function that relates the harmonic coefficients of the geoid to those of the topography. In the summations of equations (4.2) and (4.3), the lower limit l_{min} is chosen on the basis of consistency with the assumed compensation mechanism (section 4.3). The upper limit l_{max} is dictated by the quality of the measured fields, and it is set to 50, the nominal resolution of the gravitational field. Note, however, that since the power in planetary topography decreases with increasing degree (*Bills and Rubincam*, 1995), the function W_{l} assigns more weight to the lowest degrees and the choice of l_{max} is not crucial. We confirmed this inference by finding no important difference between results obtained with l_{max} equal to 50 and those with l_{max} equal to 20.

The analytical expression for Z_{l} in equation (4.2) depends on the assumed compensation model. The differentiated nature of terrestrial planets indicates

that early in their evolution the temperature of the interior was sufficiently high for the silicates to be separated from a metallic component that settled to the core. The temperature of the early crust would have been close to the solidus, if the crust formed through the solidification of a magma ocean (*Elkins-Tanton*, 2012) or if it was later modified as a result of giant impacts (e.g., *Benz et al.*, 1988). Because high temperatures decrease the elastic strength of the lithosphere (e.g., *Kampfmann and Berckhemer*, 1985), long-wavelength topographic loads are not likely to be supported by lithospheric strength (*Turcotte et al.*, 1981). Therefore we assume that a local compensation mechanism, Airy isostasy, is the principal mechanism of support of the long-wavelength variations in crustal thickness, which probably formed early in planetary evolution. In the Airy isostatic compensation model, the excess of surface relief is balanced by a crustal root. Though the use of a geoid-to-topography ratio cannot prove that Airy isostasy has been achieved, we note that the same assumption has been used in studies of the ancient crusts of other terrestrial bodies (*Wieczorek and Phillips*, 1997; *Wieczorek and Zuber*, 2004; *James et al.*, 2013). Regions on Mercury where this assumption might be invalid are excluded from the analysis (section 4.3). For Airy isostatic compensation the thickness of the crust H under a surface with topography h is (e.g., *Lambeck*, 1988)

$$H = H_0 + h \left[1 + \frac{\rho_\mathrm{c}}{\rho_\mathrm{m} - \rho_\mathrm{c}} \left(\frac{R}{R - H_0} \right)^2 \right], \tag{4.4}$$

where H_0 is the zero-elevation crustal thickness, the radius of the planet is R, and ρ_c and ρ_m are the densities of the crust and the mantle, respectively, each assumed to be uniform. The corresponding admittance function Z_l is given by the expression (e.g., *Lambeck*, 1988)

$$Z_\mathrm{l} = \frac{3}{2l+1} \frac{\rho_\mathrm{c}}{\rho} \left[1 - \left(\frac{R - H}{R} \right)^\mathrm{l} \right], \tag{4.5}$$

with ρ the mean density of the planet. Equations (4.2) and (4.5) show that, under the assumption of a given compensation mechanism and for a given choice of the crustal density ρ_c, measurements of the GTR can be inverted for the crustal thickness H.

By calculating the normative mineralogy from the elemental abundance measurements of *Weider et al.* (2012), we estimated the grain density of the northern volcanic plains material and the material in Mercury's heavily cratered terrain and intercrater plains to be 3014 kg/m^3 and 3082 kg/m^3, respectively. Our calculated mineralogies for these two units compare favorably with those from the petrological modeling of *Stockstill-Cahill et al.* (2012). Allowing for a porosity of up to 12% that might extend down to the mantle, as has been demonstrated for the Moon (*Wieczorek et al.*, 2013), we consider a conservative range in crustal densities of 2700–3100 kg/m^3. For comparison, *Anderson et al.* (1996) assumed a crustal density ρ_c of 3000 kg/m^3, *Nimmo* (2002) and *Nimmo and Watters* (2004) adopted $\rho_c = 2800$ kg/m^3, and *Smith et al.* (2012) assumed a value for ρ_c of 3100 kg/m^3. Our range in crustal density, derived from data returned by MESSENGER and the possibility of a Moon-like porosity for the crust, encompasses all of these values.

4.3 Results

The orbit of MESSENGER is highly eccentric, and the periapsis latitude has varied between 60° and 85°N. The reconstructed gravitational field in the southern hemisphere, where MESSENGER is at high altitudes, is thus of low resolution. This result is exemplified by the degree strength of the gravitational field, which describes the location-dependent harmonic degree at which the signal-to-noise ratio of the data is equal to one (*Konopliv et al.*, 1999). A map of the degree

strength for Mercury shows that the degree strength increases as a function of latitude, from about 15 on the equator to 36 near the north pole (*Mazarico et al.*, 2014a). Over the southern hemisphere there is little altimetry data, so in our analysis we considered data only from Mercury's northern hemisphere.

Large areas on the surface of Mercury are covered by smooth plains, the majority of which are inferred to be volcanic in origin (*Denevi et al.*, 2013). If the lavas that formed these plains erupted when the lithosphere was sufficiently thick to support surface loads, these regions might not satisfy our assumption of Airy isostasy. Moreover, a number of large impact craters and basins have been identified on Mercury (*Fassett et al.*, 2012) and, as is the case on the Moon and Mars, these features might depart from local isostasy (e.g., *Melosh et al.*, 2013). We excluded from the analysis all data within the rims of impact basins having diameters greater than 490 km and all regions covered by mapped expanses of smooth plains, as illustrated in Figure 4.4, in the Supplementary Materials, or SM (section 4.7). We tested that a smaller cutoff diameter for large basins did not modify the derived crustal thickness.

In the calculation of the value of the GTR within a given spherical cap, all points on smooth plains, inside large craters, or located in the southern hemisphere were discarded. If the fraction of discarded points within the cap exceeded 50%, the GTR value for that cap was discarded. (The error in the GTR value for each cap is typically smaller than 10%.) The calculated GTR as a function of the high-pass filter l_{min} for remaining areas on Mercury's surface is plotted in Figure 4.1; the error shown for each degree corresponds to the standard deviation of the population of GTRs obtained from the analysis. For $l_{\mathrm{min}} = 2$ the GTR is about 38 m/km. This value is much larger than the GTRs for $l_{\mathrm{min}} > 2$, and it is not included in Figure 4.1 for clarity. For l_{min} from 3 to 6 the value of the GTR

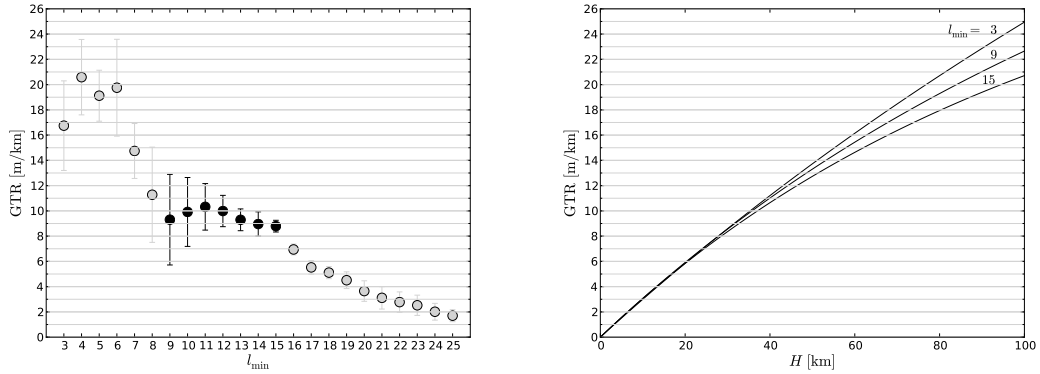

Figure 4.1: (Left) Geoid-to-topography ratio as a function of the high-pass filter cutoff $l_{\min}$ applied to the geoid and topography data. Values are obtained by regressing the two datasets within spherical caps of 2000 km radius and including only those regions compatible with the assumption of Airy isostasy. The signal interpreted as due to Airy-compensated crust is shown in black. (Right) Theoretical relation between GTR and crustal thickness for a crustal density of 2900 kg/m^3, and for different values of the high-pass filter cutoff $l_{\min}$.

is also high, with values between 16 and 21 m/km. The GTR decreases for $l_{\min}$ from 7 to 8, and then for greater values of $l_{\min}$ the GTR is relatively constant at a value of about 9 m/km. The GTRs steadily decrease with increasing $l_{\min}$ beyond 16, a figure that corresponds approximately to the degree strength of the gravitational field at the equator. Therefore, we interpret this decrease to be a reflection of the decrease in the quality and resolution of the gravity field with increasing degree above this cutoff.

We also calculated the GTR as a function of the high-pass filter cutoff $l_{\min}$ for regions initially excluded because of a possible incompatibility with the assumption of Airy isostasy (i.e., smooth plains and large craters in the northern hemisphere, Figure 4.4, SM). In contrast with Figure 4.1, the near-constant value

of GTR between degrees 9 and 15 is absent, whereas values of GTR for $l_{\min} < 9$ are compatible with those in Figure 4.1 (see Figure 4.5, SM). This difference in behavior for $l_{\min}$ from 9 to 15 justifies our assumption that the compensation state of basins and smooth plains differs from that for the surrounding heavily cratered terrain and intercrater plains. Under Airy isostasy, the predicted GTRs should be nearly uniform and independent of the value of $l_{\min}$. Therefore we regard the near-constancy of GTR values in Figure 2 between $l_{\min} = 9$ and 15 as a signal of Airy isostasy for those length scales.

A possible interpretation of the variation of GTR with $l_{\min} < 9$ is that the ratios at these long wavelengths include contributions from Mercury's mantle. Such variations could be the result of mantle convection, lateral variations in mantle composition (*Charlier et al.*, 2013), or lateral variations in temperature. To further investigate this possibility we explore the behavior of the parameter b_0 from equation (4.1). For increasing $l_{\min}$ the residual signal in b_0 is concentrated in the Caloris basin and the northern smooth plains, locations where non-Airy isostatic signals are expected (Figure 4.6, SM). In contrast, for those regions compatible with the assumption of Airy isostasy, b_0 is found to decrease with increasing $l_{\min}$, and for $l_{\min}$ greater than about 7–9, this value is close to zero. This outcome further supports our interpretation that the GTRs for $l_{\min} \geq 9$ are a result of Airy isostasy.

Although the mantle of Mercury is likely to be in a conductive state at present, a currently convecting mantle cannot be ruled out (*Michel et al.*, 2013; *Tosi et al.*, 2013). To test whether the GTR signal for $l_{\min} < 9$ might include a contribution from convection in the mantle, we compared the power spectra of the observed topography and geoid with those obtained from a representative simulation of the thermochemical evolution of Mercury in which the mantle is still convect-

ing today. These convection simulations were performed in a three-dimensional spherical shell with the code Gaia (*Hüttig and Stemmer*, 2008) following the methods of *Tosi et al.* (2013), but constrained by recently revised estimates of the global contraction of the planet (at least 5.8 km) since the end of the late heavy bombardment of the inner solar system (*Byrne et al.*, 2014). Calculation of the geoid and dynamic topography with Gaia has been validated against well-established semi-analytical solutions (*Hüttig et al.*, 2013).

The geoid and topography spectra from the simulations (Figure 4.7, SM) are orders of magnitude smaller than the observed spectra, indicating that even if the mantle were still convecting, this signal should not bias the observed GTR. We note that this result contrasts with previous convection simulations of *Redmond and King* (2007), who obtained variations in the geoid of tens of meters. *Michel et al.* (2013) showed that the current mode of heat transport in the mantle of Mercury depends on the thickness of the planet's silicate shell, with strong convection favored for greater values of the depth to the core-mantle boundary. *Redmond and King* (2007), using pre-MESSENGER information, assumed a value of 600 km for the thickness of the mantle, in contrast to the value of $\sim$ 400 km implied by MESSENGER observations (*Hauck et al.*, 2013; *Rivoldini and Van Hoolst*, 2013). This, along with their use of a Cartesian domain for their simulations, is the likely explanation for the difference between their results and the simulations presented here.

In addition to a signal derived from Airy isostasy, there may also be a contribution to the GTR at long wavelength from lateral variations in temperature within Mercury. Mercury has a very low obliquity (*Margot et al.*, 2012) and a highly eccentric orbit (*Correia and Laskar*, 2004) and is locked in a 3:2 spin–orbit resonance (*Colombo*, 1965; *Pettengill and Dyce*, 1965). As first pointed out by

Soter and Ulrichs (1967), the combination of these characteristics results in two equatorial locations that are sub-solar at perihelion (Mercury's "hot poles" at longitudes 0° and 180°E), and two equatorial locations that are sub-solar at aphelion (Mercury's "warm poles" at longitudes 90° and 270°E). The highest insolation occurs at the hot poles and results in an average temperature difference between hot and warm poles of about 130 K (*Soter and Ulrichs*, 1967). Mercury's "cold poles" are at the north and south rotational poles. *Phillips et al.* (2014) showed that the degree-2 gravity and topography signal is likely dominated by thermal effects resulting from subsurface temperature anomalies induced by the surface temperature pattern. A spherical harmonic expansion of the surface temperature shows that the greatest power is concentrated in degrees 2 ($\sim 90\%$) and 4 ($\sim 10\%$). It is thus probable that both the degree 2 and 4 signal in the GTR are affected by thermal anomalies associated with variations in surface insolation, so these degrees should be excluded from the GTR analysis. For all of the above reasons, we restrict the remaining discussion to GTR values obtained with $l_{\min}$ in the range 9 to 15 (black points in Figure 4.1).

The theoretical relation between GTR and crustal thickness, obtained from equations (4.2) and (4.5) with a crustal density $\rho_c = 2900$ kg/m^3, is shown in Figure 4.1 (right). From this relationship, the crustal thickness corresponding to each calculated GTR was estimated, and since the average elevation of each analysis region is not always equal to zero, we estimated the corresponding crustal thickness at zero elevation under the assumption of Airy isostasy from equation (4.4). For a mantle density $\rho_m = 3300$ kg/m^3, a histogram of the inferred zero-elevation crustal thickness H_0 is shown in Figure 4.2 for $l_{\min}$ from 9 to 15. As for the GTR, the error shown for each degree is taken to equal the standard deviation of the population of H_0 values obtained from the GTR values. The average value of H_0 is approximately independent of the value of the high-pass filter cutoff, and

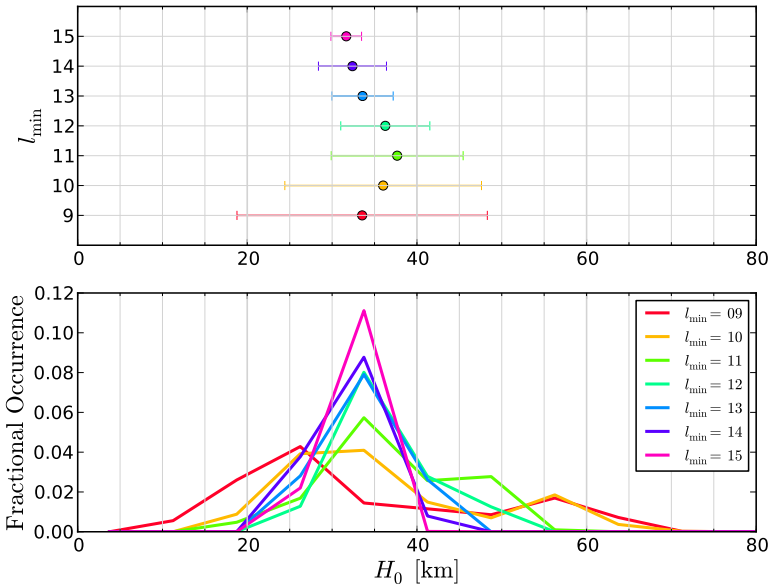

Figure 4.2: Average crustal thickness at zero elevation H_0 of Mercury obtained from the calculated GTR (black symbols in Figure 4.1, left) for a crustal density of 2900 kg/m^3 and a mantle density of 3300 kg/m^3. (Top) Average and standard deviation of H_0 as functions of the high-pass filter cutoff $l_{\min}$. (Bottom) Histograms of the calculated crustal thickness H_0.

the uncertainty decreases somewhat with increasing $l_{\min}$. A conservative estimate for the thickness of the crust of Mercury is obtained by combining the results for $l_{\min} = 9$, which has the largest uncertainty, with our calculated bounds on the crustal density of 2700 and 3100 kg/m^3. For our best-fit crustal thickness, we give the average obtained from the upper and lower bounds on crustal density for $l_{\min} = 9$, and for uncertainty we give the maximum of the corresponding one-standard-deviation limits. On this basis, we obtain an average crustal thickness of the planet of $H_0 = 35 \pm 18$ km.

4.4 Discussion and Implications

Our estimate for the average crustal thickness of Mercury is considerably less than previously reported values. The value obtained by *Anderson et al.* (1996) is seemingly in contradiction with ours, and we re-evaluate their estimate with updated MESSENGER-derived values of the gravitational and topographic C_{22} terms (*Smith et al.*, 2012; *Zuber et al.*, 2012). Using the same approach as *Anderson et al.* (1996), we revise their estimate downward from 200 to 171 km. If we were to have inferred the crustal thickness from our GTR analysis by setting the high-pass filter cutoff $l_{\min} = 2$, we would have obtained a similarly high crustal thickness $H_0 = 160 \pm 32$ km. With a silicate shell no more than ~ 400 km thick, however, it is highly improbable that the crustal thickness could be so large. The degree-2 gravity and topography are thus likely to reflect processes other than local Airy isostasy. Other studies provided only upper bounds on the crustal thickness (*Nimmo*, 2002; *Nimmo and Watters*, 2004), and they are consistent with our value of 35 ± 18 km.

The crust of Mercury has a thickness comparable to the thickness of the crust of the Moon ($H = 38.5 \pm 4.5$ km, *Wieczorek et al.*, 2013), Venus ($H = 16.5 \pm 8.5$ km, *James et al.*, 2013), and Mars ($H = 57 \pm 24$ km, *Wieczorek and Zuber*, 2004), as well as that of the continental crust on Earth ($H \sim 35$ km, e.g., *Turcotte and Schubert*, 2002). The relative size of the radius of the core of Mercury ($\sim 82.5\%$ of the radius of the planet, or 2014 km) (*Hauck et al.*, 2013; *Rivoldini and Van Hoolst*, 2013) is the largest among the terrestrial planets. As a result, the volume of the crust accounts for about 10% of the total volume of silicate materials in the planet. This value is the highest among the terrestrial planets and implies that Mercury had the highest efficiency of crustal production. (For comparison the fraction of silicates in the crust is about 7% for the Moon

and 5% for Mars, and for Venus the fraction is probably similar to Earth's value, i.e., less than 2%.) If the thickness of the northern plains ($\sim$ 2 km) (*Head et al.*, 2011) is representative of the contribution to the crust crust produced by the most recent widespread episodes of partial melting of the mantle, then a large fraction of Mercury's crust was produced early in its history.

Modeling the thermo-chemical evolution of the terrestrial planets requires knowledge of the amount of radioactive elements in both the mantle and the crust (e.g., *Schubert et al.*, 2001), which for Mercury can be evaluated with our estimate of crustal thickness. The abundances on the surface of Mercury of the heat-producing elements K, Th, and U have been measured with the Gamma-Ray Spectrometer on MESSENGER (*Peplowski et al.*, 2011, 2012). If the abundances of these elements are uniform within a surficial enriched layer, then the thickness of such a layer can be inferred to lie between about 2 km, the approximate thickness of the northern plains deposits (*Head et al.*, 2011), and 53 km, our upper bound on the crustal thickness. The non-enriched part of the crust is assumed to have the same abundances of incompatible elements as the mantle. With assumed values of bulk abundances of heat-producing elements in the silicate part of the planet, it is then possible, by mass balance, to estimate the current abundances of each of these elements in the mantle and their contribution to heat production as a function of time. Because the bulk silicate composition of Mercury is not known, we use two end-member models: the primitive Earth mantle model of *Lyubetskaya and Korenaga* (2007) and the CI chondrite model of *McDonough and Sun* (1995). For the mean density of the silicate shell of Mercury we use the value 3380 kg m^{-3} (*Hauck et al.*, 2013).

The current mantle heat production Q_{m} as a function of the thickness of the enriched layer is shown in Figure 4.3. The curves correspond to different

crustal densities and bulk abundance of heat-producing elements. Each curve is interrupted at the point at which the mass balance calculation returns a zero abundance for one of the three heat-producing elements. This set of calculations allows maximum and minimum values for Q_{m} at present to be determined, respectively, 4.55×10^{-12} and 1.88×10^{-12} W/kg (the abundances of each heat-producing element are reported in Table 4.1). From these two values, the mantle heat production as a function of time can then be calculated (Figure 4.3). A lower bound on the mantle heat production at a time following accretion and differentiation ($\sim$ 4.45 Ga, a value obtained by subtracting 100 Ma, a reference interval of time for the accretion and differentiation of terrestrial planets (e.g., *Jacobson et al.*, 2014), from the time of the formation of the Solar System, $\sim$ 4.55 Ga (*Bouvier and Wadhwa*, 2010)) is obtained under the assumption that the concentration of radioactive elements into the crust dates back to the earliest history of Mercury. Under such an assumption the mantle heat production would have been in the range 5.4×10^{-12} to 2.3×10^{-11} W/kg. This interval is consistent with, but slightly more restrictive than, the lower bound on initial mantle heat production of 3×10^{-12} W/kg adopted by *Redmond and King* (2007), and it partially overlaps the lower range of initial mantle heat production explored by *Michel et al.* (2013) (from 1×10^{-11} to 1.25×10^{-10} W/kg). Such a value for mantle heat production corresponds to a crustal enrichment factor between 3.4 and 14.5; for comparison, the range for this factor assumed by *Tosi et al.* (2013) was between 2 and 10.

Models for the formation of major impact basins on the Moon suggest that some may have excavated mantle material at the time of impact and left such material exposed on the modern lunar surface (*Miljković et al.*, 2015). The similarly thin crust of Mercury therefore opens the possibility of excavation of mantle material during the formation of the largest impact basins, such as Caloris. The

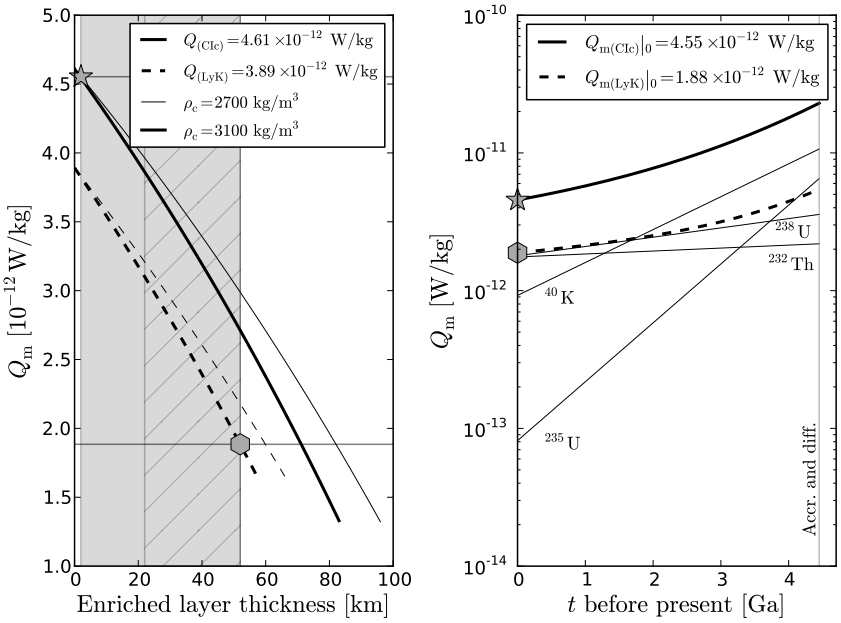

Figure 4.3: Heat production in the mantle Q_{m} from radioactive decay of K, Th, and U. (Left) Current heat production as a function of the thickness of an enriched surficial layer for two crustal densities (indicated by the line thickness) and two bulk silicate abundances derived from the primitive Earth mantle model of *Lyubetskaya and Korenaga* (2007) (LyK, dashed lines) and the CI chondrite model of *McDonough and Sun* (1995) (CIc, solid lines). The shaded area spans the interval 2−53 km; the lower limit corresponds to the estimated thickness of the northern plains deposits (*Head et al.*, 2011) and the higher limit to the maximum value of the crustal thickness as inferred from the GTR analysis (hashed area). The minimum and maximum values of Q_{m} are indicated by the hexagon and the star, respectively. (Right) Mantle heat production as a function of time for the minimum and maximum values obtained from the left panel. The bold lines show the total heat production for the CIc model (solid) and the LyK model (dashed). For the CIc model the contributions of individual isotopes are also shown. The vertical line indicates the approximate time of completion of accretion and differentiation of the planet (4.45 Ga).

identification and characterization of mantle material would provide valuable information on the composition of the bulk silicate portion of the planet, which in turn would be informative of the planet's formation (e.g., *Taylor and Scott*, 2005) and interior structure (*Hauck et al.*, 2013; *Rivoldini and Van Hoolst*, 2013; *Padovan et al.*, 2014a).

4.5 Conclusions

With gravity and topography data acquired by the MESSENGER spacecraft we have calculated geoid-to-topography ratios (GTRs) over the northern hemisphere of Mercury. Excluding the longest wavelengths, which are likely to be sensitive to long-wavelength variations in interior thermal structure associated with Mercury's low obliquity and 3:2 spin-orbit resonance, as well as possible lateral variations in the composition of Mercury's mantle, we assume that Airy isostasy is responsible for the remaining signal. This analysis implies that the average crustal thickness of Mercury is 35 ± 18 km.

This new mean value is substantially smaller than earlier estimates (*Anderson et al.*, 1996; *Nimmo*, 2002; *Nimmo and Watters*, 2004) and is broadly similar to the thickness of the crust of the other terrestrial planets and the Moon. Given the large core size of Mercury, the crust comprises about 10% of the silicate volume, a value that is the largest among the terrestrial planets and points to a high efficiency of crustal production. With such a thin crust, it is possible that the formation of the major impact basins may have excavated mantle material that is currently exposed on the surface. A search for such exposed mantle material is warranted in observations acquired by MESSENGER and future spacecraft missions at Mercury.

By combining our crustal thickness determination with the abundances of heat-producing elements on the surface of Mercury measured by MESSENGER (*Peplowski et al.*, 2011, 2012), we constrain the amount of heat produced in the mantle over time. Our results are broadly consistent with assumptions made in previous studies of the thermal evolution of the mantle of Mercury (*Redmond and King*, 2007; *Michel et al.*, 2013; *Tosi et al.*, 2013) and can inform future models of the thermo-chemical evolution of the planet.

4.6 Acknowledgments

We thank all the individuals who designed and operate the MESSENGER spacecraft. We are grateful to Brett Denevi for providing the locations of mapped smooth plains. This work was conducted while S.P. was visiting M.A.W. with the support of a Chateaubriand Fellowship. Part of the calculations used the freely available software SHTOOLS (*Wieczorek*, 2014), and the figures were created with the free software described by *Wessel and Smith* (1991) and *Hunter* (2007). S.P. and J.-L.M. were partially supported by MESSENGER Participating Scientist Program grant NNX09AR45G and by the UCLA Division of Physical Sciences. N.T. was partially supported by the DFG (project T0704/1-1) and by the Helmholtz Gemeinschaft (project VH-NG-1017). Computational time for the convection simulations was provided by the HLRN (project bep0041). The MESSENGER project is supported by the NASA Discovery Program under contracts NAS5-97271 to The Johns Hopkins University Applied Physics Laboratory and NASW-00002 to the Carnegie Institution of Washington.

4.7 SM: Supplementary Material

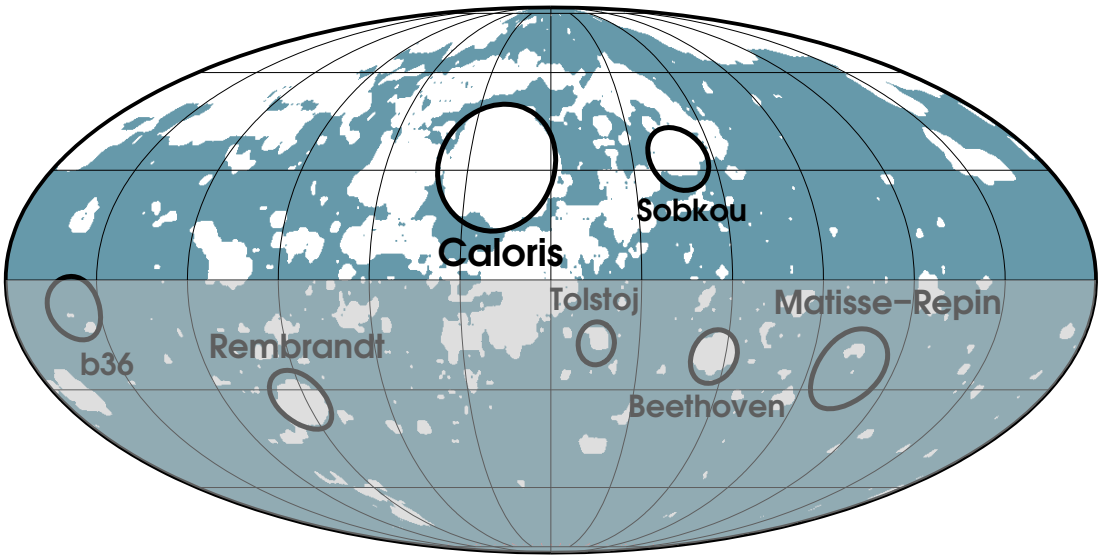

Figure 4.4: Distribution on Mercury of smooth plains (white areas) mapped by *Denevi et al.* (2013) and major impact basins having a diameter > 490 km (circles) identified by *Fassett et al.* (2012); Mollweide equal-area projection centered on the 180°E meridian. In the southern hemisphere (shaded gray) there is little altimetry data and the gravity field is known only at low resolution.

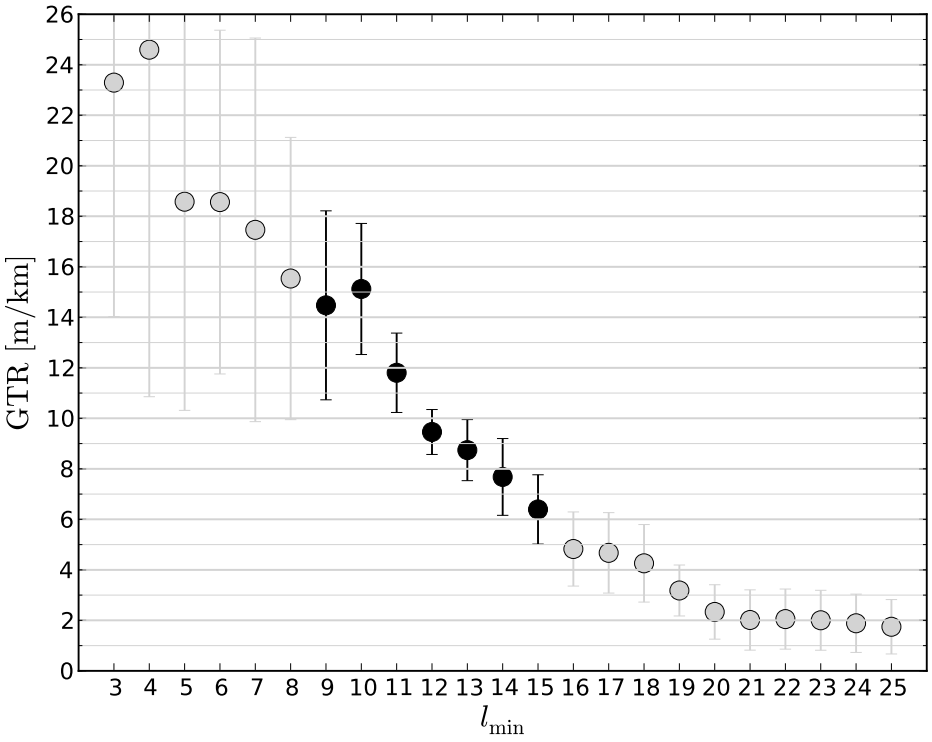

Figure 4.5: Geoid-to-topography ratio as a function of the high-pass filter cutoff $l_{\min}$ applied to geoid and topography data within caps of radius $r = 2000$ km, in northern hemisphere regions not compatible with the assumption of Airy isostasy (i.e., regions shown in white in Figure 4.4).

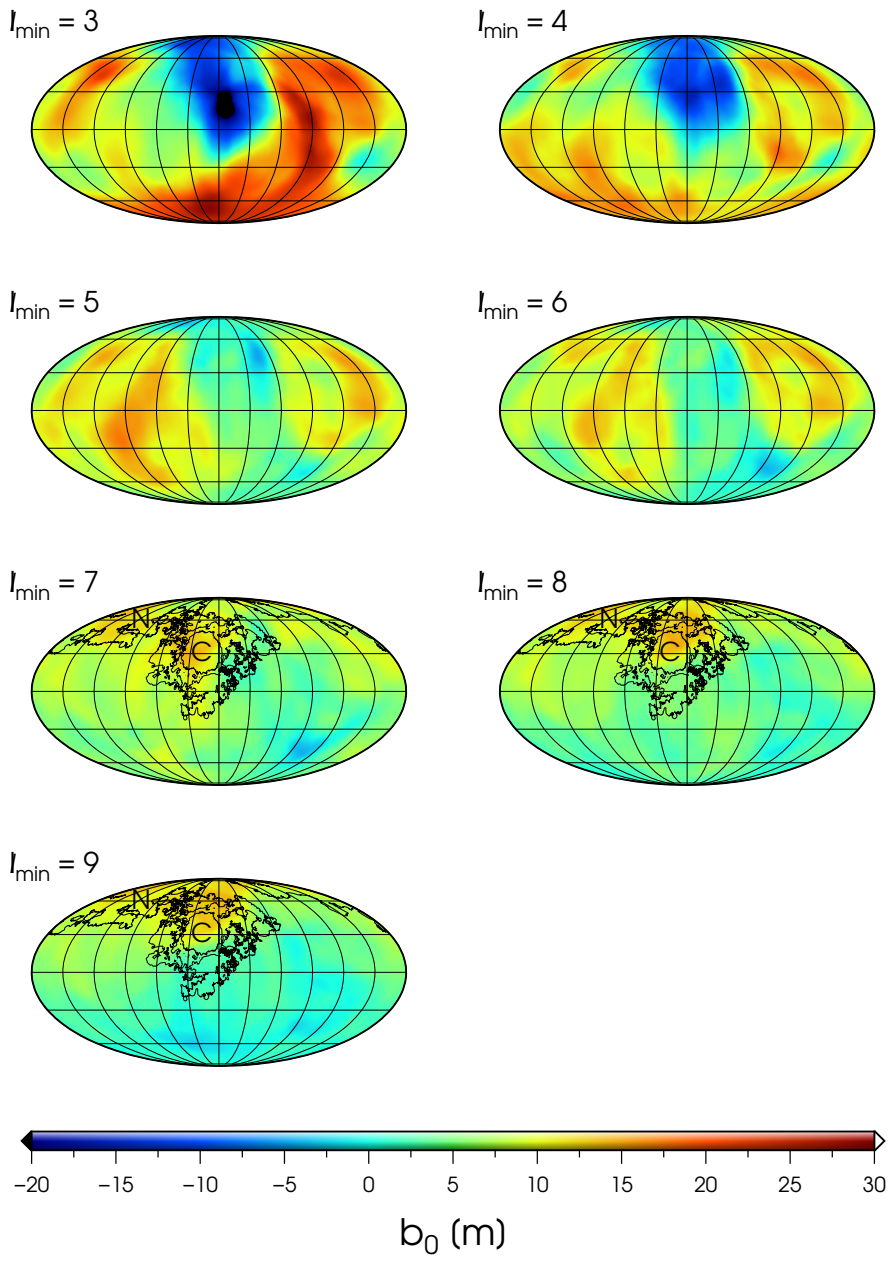

Figure 4.6: Maps of the parameter b_0 in equation (4.1) as a function of the high-pass filter cutoff $l_{\min}$; Mollweide projections, centered on the 180°E meridian. For $l_{\min} = 7$, 8, and 9 the smooth plains associated with the Caloris basin (C) and the northern volcanic plains (N) are delineated.

Table 4.1: Heat-producing Elements in the Silicate Portion of Mercury.

	U (ppb)	Th (ppb)	K (ppm)
Surface abundances (observed) (*Peplowski et al.*, 2011, 2012)	90	155	1288
Bulk silicate abundances (assumed)			
Model 1: (*McDonough and Sun*, 1995)	70	290	550
Model 2: (*Lyubetskaya and Korenaga*, 2007)	17	63	190
Current mantle abundances[a]			
Maximum [Model 1][b]	20	69	265
Miminum [Model 2][c]	6	49	22

[a] These abundances are calculated from mass balance and a silicate shell density of 3380 kg m^{-3} (*Hauck et al.*, 2013).

[b] This case corresponds to the star symbol in Figure 4.3.

[c] This case corresponds to the hexagon symbol in Figure 4.3.

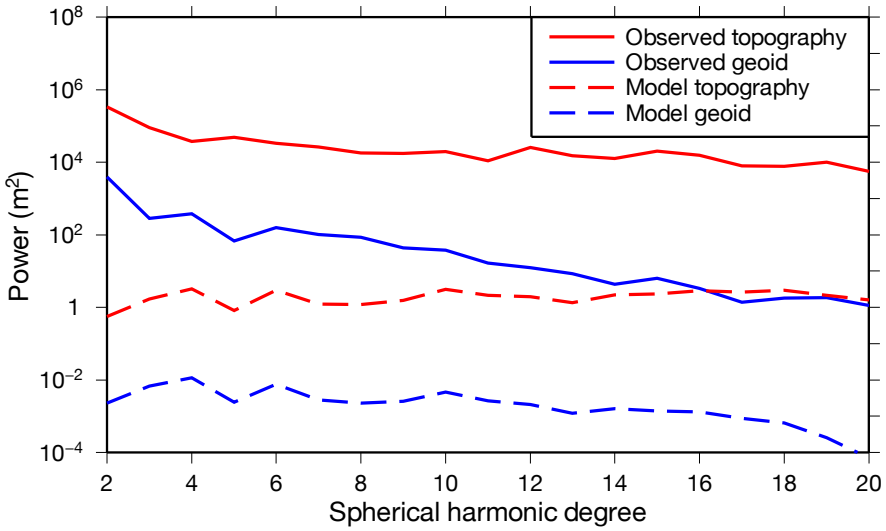

Figure 4.7: Power spectra for the geoid (blue) and topography (red). Solid lines represent the observed spectra; broken lines are for a thermo-chemical evolution model with mantle convection at present. The model spectra are orders of magnitude smaller than the observed spectra.

CHAPTER 5

Discussion, conclusions, and future work

5.1 Discussion and conclusions

The initial results of the MESSENGER team regarding the interior structure of Mercury indicated the possible existence of a solid FeS layer at the bottom of the mantle of the planet (*Smith et al.*, 2012). Such hypothesis was based both on the high density of the outer solid shell as inferred from geodetic and radar data (*Smith et al.*, 2012) and on the inference that the planet formed under highly reducing conditions (*Nittler et al.*, 2011). Of course more standard models with a silicate-only outer shell, characterized by a mantle and a crust, were perfectly compatible with the data (*Hauck et al.*, 2013; *Rivoldini and Van Hoolst*, 2013). Subsequent improvements in the estimate for the obliquity of Mercury from Earth-based radar data made the density argument for the presence of a solid FeS layer less compelling (*Margot et al.*, 2012). However, the geochemical argument is still valid and a recent paper reporting the results of laboratory experiments on Mercurian analogs seems to indicate that a solid FeS layer is indeed a possibility (*Malavergne et al.*, 2014).

From the point of view of the material properties the FeS layer is markedly different from the silicates that compose the mantle and the crust. We hypothesized that the measurement of the tidal response of the planet might provide some insights on the presence of this layer. The comparison of one estimate of

the tidal Love number k_2 of Mercury (*Mazarico et al.*, 2014a) with our models for the tidal deformation of the planet seems to indicate that the presence of a solid FeS layer at the bottom of the mantle is unlikely. Furthermore the same comparison seems to indicate that the temperature at the bottom of the mantle is around 1600 K, in the low range of possible basal mantle temperatures as independently inferred by *Tosi et al.* (2013) and *Rivoldini and Van Hoolst* (2013). The forthcoming BepiColombo mission to Mercury is expected to provide an improved estimate for the value of k_2 of Mercury which will allow to make more conclusive inferences regarding the temperature of the mantle and the presence of a FeS layer.

The first paper published by the MESSENGER team on the internal structure of Mercury included a map of the crustal thickness of the planet obtained from the joint analysis of the gravity and altimetry data returned by the spacecraft (*Smith et al.*, 2012). The crustal thickness map in *Smith et al.* (2012) was obtained by assuming a constant density of the crust, values for the density of the crust and the mantle, and a value for the average thickness of the crust. While an educated guess for the densities of crustal and mantle materials can be based on the measured surface composition, the assumed value for the average crustal thickness is rather arbitrary. The only real constraint is that in the resulting crustal thickness map the thickness is everywhere positive. In *Smith et al.* (2012) an average thickness of 50 km was assumed.

We approached the problem of estimating the crustal thickness using the same datasets as *Smith et al.* (2012), i.e., gravity and altimetry, but with a different method. We assumed that Airy isostasy is the mechanism of support for the long-wavelength topography of Mercury. By limiting the analysis to areas on the surface that are compatible with our assumed compensation model we

constrained the crustal thickness by interpreting the geoid-to-topography ratios with the spectrally weighted admittance model of *Wieczorek and Phillips* (1997). We obtained a conservative estimate of 35 ± 18 km. This estimate has three straightforward yet informative implications. First, a constraint on the value of the crustal thickness can be used to constrain the amount of heat producing elements in the mantle if their surface abundances have been measured. Using the abundances on the surface of Mercury of ^{40}K, ^{232}Th, ^{235}U, and ^{238}U as measured by MESSENGER (*Peplowski et al.*, 2011, 2012), we put a lower bound of 5.4×10^{-12} W/kg on the amount of heat produced in the mantle of Mercury after its primary differentiation. Second, by comparing the volume of the crust of Mercury with the volume of its mantle we inferred that Mercury produced crustal material more efficiently than the other terrestrial planets and the Moon. Third, the relatively thin crust of Mercury points to the possibility that during the formation of large impact basins mantle material might get exposed on the surface, as demonstrated in the case of the Moon (*Miljković et al.*, 2013, 2015). This material might be currently observable.

Summarizing, the main contributions of the work presented in this dissertation can be listed as follows:

- We pointed out that for Mercury, whose radius of the core is known to a remarkable precision from the measurement of the moment of inertia and the moment of inertia of the outer solid shell, the measurement of k_2 is informative of the rheology of the outer solid shell. This situation is currently unlike any other rocky body, since k_2 has been previously used only to infer the state (Mars and Venus) and size of the core (Mars). For Mercury the measured k_2 provides an independent evidence for a fluid core (already inferred from Earth-based radar measurements and from the interpretation

of the magnetic field detected by the MESSENGER magnetometer);

- The comparison of our modeled values for k_2 (between 0.45 and 0.52, depending on the interior structure and rheological properties of the outer solid shell) with the *Mazarico et al.* (2014a) estimate based on data obtained with the MESSENGER mission indicates that the presence of a solid FeS layer at the bottom of the mantle of Mercury is unlikely. Similarly, we infer that the basal mantle temperature is probably in the lower range of the interval from 1600 to 1900 K obtained from thermal history calculations and analysis of geodetic data;

- By analyzing gravity and altimetry data, we provide the first relatively well constrained estimate of the thickness of the crust of Mercury, 35 ± 18 km. This estimate is considerably smaller than earlier estimates;

- The estimate for the thickness of the crust is used to investigate implications about mantle heat production (at least 5.4×10^{-12} W/kg after the initial differentiation of the planet), efficiency of crustal production in Mercury (the highest among the rocky bodies of the inner solar system), and possibility of exposure of mantle material during major basin-forming events (mantle material might be currently exposed on the surface and thus it could be observable by MESSENGER and future missions at Mercury).

5.2 Future work

5.2.1 Possible subsurface structure of smooth plains

While investigating the thickness of the crust of Mercury we noted that there is a clear signal in the geoid associated with the northern volcanic plains and

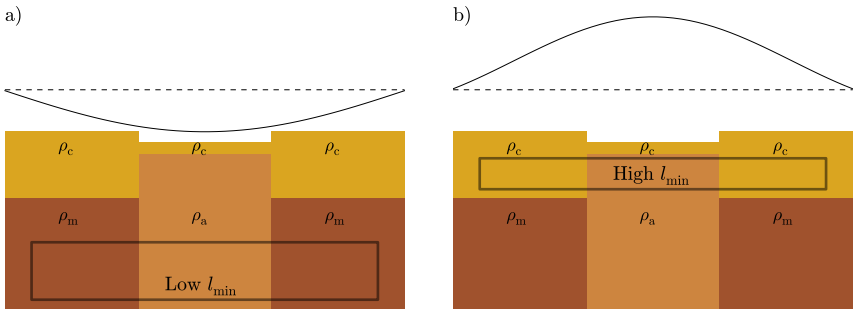

Figure 5.1: Possible subsurface structure under large areas of smooth plains, which in this cartoon correspond to the central columns. The light brown color indicates a mantle density anomaly with density $\rho_a < \rho_m$, where ρ_m indicates the density of mantle material surrounding the anomaly. The crust (mustard) has a density $\rho_c < \rho_a$. The broken lines indicate the geoid in the absence of the mantle anomaly and of the thinned crust above it. The solid lines indicate the geoid as modified by the subsurface structure. a) At low harmonic degrees the geoid is sensitive to the deep subsurface structure (qualitatively identified with the box), where the mantle anomaly depresses the geoid with respect to the reference geoid. b) At higher harmonic degrees the geoid is more sensitive to the shallow subsurface structure, where the thinned crust and denser material close to the surface correspond to a positive geoid offset.

the Caloris basin, areas that correspond to the largest swaths of smooth plains on Mercury. The signal is negative at low harmonic degrees and becomes positive with increasing harmonic degrees (Figure 4.6). One possible explanation for this finding is that the mantle material under the Caloris basin and the northern volcanic plains is less dense than the surrounding mantle material and the same regions correspond to a thinner than average crust. The cartoon in Figure 5.1 qualitatively describes this interpretation. The works of *Smith et al.* (2012) and *James et al.* (2014) indeed indicate that the Caloris region and the northern volcanic plains correspond to regions with a thinner than average crust. Fur-

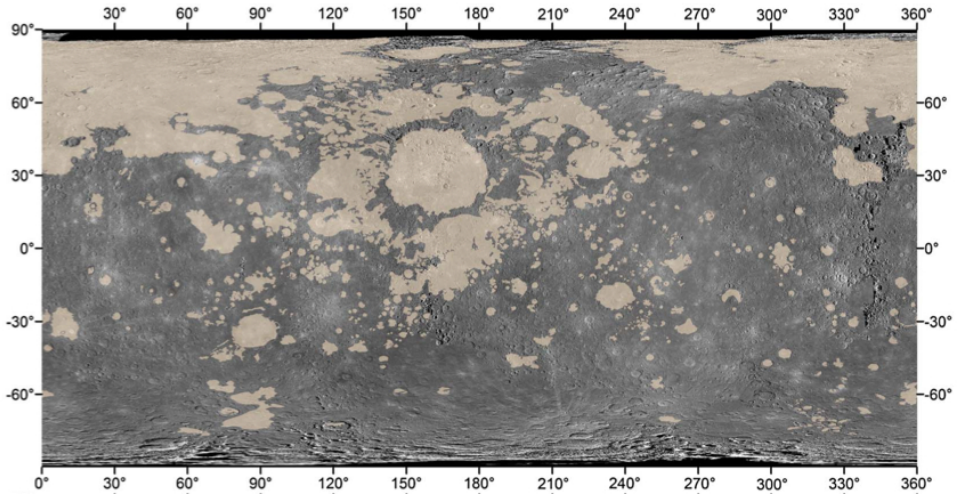

Figure 5.2: Smooth plains on the surface of Mercury (tan). Cylindrical projection; the central longitude is 180° E. Figure from *Denevi et al.* (2013).

thermore, *James et al.* (2014) show that the Caloris basin is associated with a negative mantle density anomaly.

5.2.2 A hypothesis for the emplacement of the smooth plains on Mercury

The distribution of the smooth plains of Mercury, the majority of which are thought to be volcanic in origin, is far from homogeneous (*Denevi et al.*, 2013). They are concentrated at high latitudes in the northern volcanic plains. At lower latitudes they are found roughly at longitudes around 180° E (i.e., within and around Caloris basin), and at longitudes around 0° (Figure 5.2).

In the modeling of the tides of Mercury we concentrated on the information contained in the magnitude of k_2. However, the k_2 of any planet is a complex quantity whose imaginary part is very small and usually not observable. Nonetheless it is this small imaginary part that encapsulates the energy dissipation in the

interior of the body (the same dissipation that is responsible for orbital evolution and that brought Mercury into its current 3:2 spin-orbit resonance). The power dissipated through tidal processes within a body has a distinct spatial pattern (e.g., *Beuthe*, 2013) that depends on the density stratification, temperature profile, and material properties within the body (e.g., *Segatz et al.*, 1988). The tidally-dissipated power is also dependent on the orbital configuration, as shown in *Běhounková et al.* (2010) by comparing the dissipation for a body in a 1:1 spin-orbit resonance with the dissipation in the case of a 3:2 spin-orbit resonance.

A relation between the northern volcanic plains and the plains associated with the Caloris basin seems implied by the similar age shared by the two regions (*Head et al.*, 2011). However, the northern plains are not related to any impact basin and *Head et al.* (2011) concluded that the emplacement of the smooth plains was independent of the largest cratering events. We put forward the hypothesis that the impact that formed the Caloris basin delivered an amount of energy that locally modified the temperature structure in the underlying mantle locally enhancing the tidal dissipation that was then focussed elsewhere through convective and tide-related processes. The possibility of high tidal dissipation is reasonable given that the mantle of Mercury is only about 400 km thick (*Hauck et al.*, 2013; *Rivoldini and Van Hoolst*, 2013) and the temperature at the core mantle boundary is relatively high (*Tosi et al.*, 2013; *Rivoldini and Van Hoolst*, 2013). As a consequence, a large fraction of the mantle is at high temperature and therefore highly dissipative. The addition of energy from the impact would locally increase the temperature and therefore the dissipation (since in general temperature correlates with dissipation, see, e.g., Figure A.6). The distinct distribution of the smooth plains, with their latitudinal dependence and concentration around the meridians of longitude 0° and 180° E is indicative of a spatially organized process

such as tidal dissipation (*Segatz et al.*, 1988; *Běhounková et al.*, 2010; *Beuthe*, 2013).

The possibility of a link between the event that formed the Caloris basin and the emplacement of the smooth plains associated with Caloris has been explored in *Roberts and Barnouin* (2012). The authors investigated how the effects of the energy delivered in the impact might affect mantle convection and melt production, but did not take into account tidal dissipation. We plan on extending the code we used for the calculation of the tides of Mercury to include the spatial-dependent tidal dissipation. The code will need to be merged with a convection code to treat both processes together, similarly to the approach developed in *Běhounková et al.* (2010). The goal is to test our hypothesis that the smooth plains associated with the Caloris basin and the northern volcanic plains are the result of processes related to the impact that formed the Caloris basin. Additionally we will test how our results are dependent on the spin-orbit configuration of Mercury at the time of impact. The findings of this project might be used to investigate the scenario described in *Wieczorek et al.* (2012), where the current 3:2 spin-orbit resonance of Mercury is inferred to be the result of an impact that unlocked the planet from an earlier retrograde 1:1 spin-orbit configuration.

APPENDIX A

Background materials for chapter 2.

A.1 Viscoelastic models for the interior of terrestrial planets

In this section we review the part of the theory of viscoelasticity which is relevant to the calculation of the tidal deformation of a planetary body. The section is not meant to be self-contained. We point to the relevant literature while giving the derivations where they are missing in the references cited. The source of the material is *Wolf* (1994), unless otherwise noted. The paper by *Wolf* (1994) deals with a homogeneous planet. Because we are interested in the response of a multi-layer planet, we will extend the theory presented in *Wolf* (1994) to the case of a multi-layer planet. The approach is the same as in *Moore and Schubert* (2000), where the tidal response of Europa was estimated. Some of the derivations presented here are only available in a document written in German (*Wieczerkowski*, 1999).

In terms of notation, the following conventions are adopted. Vectorial quantities are indicated with bold symbols (e.g., vector $\mathbf{u}$). The only exception is the differential operator ∇, which cannot induce confusion. Components of a vector are indicated by a subscript (e.g., vector component u_i). Unit vectors are indicated with a hat (e.g., $\hat{\boldsymbol{\epsilon}}$). Einstein convention is adopted, where repeated indexes imply summation (e.g., $\mathbf{u} = u_i \hat{\boldsymbol{\epsilon}}_i$ indicates the vector $\mathbf{u}$ in terms of its components

u_i in the basis with components $\hat{\boldsymbol{\epsilon}}_i$). A comma in the subscript indicates spatial derivative with respect to the quantities following the comma (e.g., $u_{i,j}$ is the derivative of the u_i component with respect to the j coordinate). Matrices are indicated with uppercase bold fonts (e.g., the matrix $\mathbf{A}$.)

A.1.1 Models for the planets

We consider a spherical planet whose physical properties (density, elastic parameters, viscosity) are assumed to be constant, except at spherical interfaces. The inclusion of the self gravitation in the elastic equations for a spherical body is due to *Love* (1911). The initial state is assumed to be that of a spherically symmetric hydrostatic body. The equations describing this state are introduced in section A.1.2. The tidal force acting on the planet is considered as an infinitesimal perturbation which modifies the initial hydrostatic state. In the presence of the perturbation the total fields (by field we mean all the relevant physical variables of the problem) are the sum of the initial fields and of the incremental fields resulting from the perturbation. The symmetry of the problem warrants the use of spherical coordinates.

A.1.2 Equations for the initial fields

The initial fields are those describing the hydrostatic equilibrium of a body under its own gravitational potential. This assumption implies that the initial state of the material is that of a fluid where deviatoric stresses vanish. Indicating with the superscript (0) quantities in the initial fields, with P the pressure, and with ρ the local density, the hydrostatic equilibrium equation reads

$$P_{,r} = -\rho\phi^{(0)}_{,r}. \tag{A.1}$$

The gravitational potential ϕ inside the body is described by Poisson's equation

$$\nabla^2\phi^{(0)} = \phi^{(0)}_{,ii} = -4\pi G\rho. \tag{A.2}$$

The gravitational field g is derived from the gravitational potential as

$$g^{(0)}_i = \phi^{(0)}_{,i}. \tag{A.3}$$

A.1.3 Solution for the initial fields

The unperturbed body is spherically symmetric and only the radial derivatives are different from zero. The solution for the gravity and the potential is obtained by dividing the planet into thin spherical shells and evaluating the contributions of the material above and below an empty shell defined by the radii $r' - \epsilon$ and $r'+\epsilon$. The solutions are then obtained by taking the limit for $\epsilon \to 0$ (e.g., *Ramsey*, 1949). For a homogeneous planet:

$$\phi^{(0)}(r < R) = \frac{2}{3}\pi G\rho R^2 \left(3 - \frac{r^2}{R^2}\right), \tag{A.4}$$

$$\phi^{(0)}(r > R) = \frac{GM}{r}, \tag{A.5}$$

$$g^{(0)}(r < R) = -\frac{4}{3}\pi\rho G r, \tag{A.6}$$

$$g^{(0)}(r > R) = -\frac{GM}{r^2}, \tag{A.7}$$

where r is the radial coordinate and R is the radius of the planet. The solution for the pressure $P^{(0)}$ is:

$$P^{(0)}(r < R) = \frac{2}{3}\pi G\rho^2 \left(R^2 - r^2\right). \tag{A.8}$$

A.1.4 Incremental fields and interface conditions

For the models described in section A.1.1, the material form[1] of the incremental fields is described by the following set of equations (the details of the derivation are given in *Wolf*, 1993)

$$u_{i,i} = 0, \tag{A.9}$$

$$t_{ij}^{(\delta)} = -\delta_{ij} P^{(\delta)} + \int_0^t m(t-t')\partial_{t'}[u_{i,j} + u_{j,i}]dt', \tag{A.10}$$

$$t_{ij,j}^{(\delta)} + P_{,j}^{(0)} u_{j,i} + \rho(\phi_{,i}^{(\delta)} - \phi_{,j}^{(0)} u_{j,i}) = 0, \tag{A.11}$$

$$g_i^{(\delta)} = \phi_{,i}^{(\delta)} - \phi_{,j}^{(0)} u_{j,i}, \tag{A.12}$$

$$\phi_{,ii}^{(\delta)} - 2\phi_{,ij}^{(0)} u_{i,j} - \phi_{,i}^{(0)} u_{i,jj} = 4\pi G\rho u_{i,jj}. \tag{A.13}$$

In the previous equations t indicates the time variable and the superscript (δ) indicates the material increment. Equations (A.9)-(A.13) represent the condition of incompressibility (with u_i the i-th component of the displacement), the constitutive relation (with $m(t-t')$ the stress-relaxation function), the equations of motion, the gravity perturbation, and the perturbation of the potential, respectively. Indicating with $n_i^{(0)}$ the outward unit normal, at each internal interface the continuity of the incremental fields is expressed as

$$[u_i]_-^+ = 0, \tag{A.14}$$

$$\left[n_j^{(0)} t_{ij}^{(\delta)}\right]_-^+ = 0, \tag{A.15}$$

$$\left[\phi^{(\delta)}\right]_-^+ = 0, \tag{A.16}$$

$$\left[n_i^{(0)}\left(\phi_{,i}^{(\delta)} - \phi_j^{(0)} u_{j,i}\right)\right]_-^+ = 0. \tag{A.17}$$

[1]The description of the deformation can be made in terms of the undeformed state (i.e., hydrostatic equilibrium) or of the deformed state. In the former case the independent variable is the spatial coordinate in the undeformed state and it is used to describe material points. This description is referred to as Lagrangian formulation. In the latter case the independent variable is the spatial coordinate of the deformed state and it is used to describe local points. This description is referred to as Eulerian formulation. In the problem of (visco-)elasticity, the Lagrangian formulation is preferred since the initial state is known (e.g., *Malvern*, 1969).

The notation $[f]_-^+$ indicates the difference between the quantity f evaluated on the two sides of the interface. Equations (A.14)–(A.17) represent the continuity of deformation, incremental stress, incremental potential, and incremental potential gradient, respectively.

To treat viscoelastic problems, the equations are Laplace transformed, since in the frequency domain the viscoelastic problem is formally equivalent to the elastic one, thanks to the correspondence principle (*Biot*, 1954). Indicating with s the frequency the Laplace transform of f is $\tilde{f} = \mathcal{L}[f] := \int_0^\infty f(t)\exp(-st)dt$. With the following relations (e.g., *LePage*, 1980)

$$\mathcal{L}\left[af(t) + bg(t)\right] = a\tilde{f}(s) + b\tilde{g}(s), \tag{A.18}$$

$$\mathcal{L}\left[f_{,t}(t)\right] = s\tilde{f}(s) - f(0), \tag{A.19}$$

$$\mathcal{L}\left[\int_0^t f(t-t')g(t')dt'\right] = \tilde{f}(s)\tilde{g}(s), \tag{A.20}$$

the set of equations (A.9)-(A.13) can be directly recast in the frequency domain.

To simplify the set of equations (A.9)–(A.13) *Wolf* (1994) introduced the Newtonian formulation, which is used to describe isopotential points. These points are defined as "points that can only move in the direction of the gradient of the gravitational potential... the potential at the point remains constant while the latter is being displaced" (*Wolf*, 1994). Expressing the pressure and the stress material increments in terms of their isopotential increments (i.e., using the Newtonian formulation with the superscript (∂) indicating the increment), and the gravity and potential material increments in terms of their local increments (i.e., using the Eulerian formulation with the superscript Δ indicating the increment), the set of equations (A.9)–(A.13) becomes in the frequency domain (the details

of this cumbersome transformation are found in Chapter 2 of *Wolf*, 1993):

$$\tilde{u}_{i,i} = 0, \tag{A.21}$$

$$\tilde{t}_{ij}^{(\partial)} = -\delta_{ij}\tilde{P}^{(\partial)} + s\tilde{m}(\tilde{u}_{i,j} + \tilde{u}_{j,i}), \tag{A.22}$$

$$\tilde{t}_{ij,j}^{(\partial)} = 0, \tag{A.23}$$

$$\tilde{g}_i^{(\Delta)} = \tilde{\phi}_{,i}^{(\Delta)}, \tag{A.24}$$

$$\tilde{\phi}_{,ii}^{(\Delta)} = 0. \tag{A.25}$$

This approach separates the mechanical quantities from the gravitational quantities (compare Eq. (A.11) and Eq. (A.23)). The coupling is shifted to the interface conditions, which become

$$[\tilde{u}_i]_-^+ = 0, \tag{A.26}$$

$$\left[n_j^{(0)}\tilde{t}_{ij}^{(\delta)} - \rho n_i^{(0)}\left(\tilde{\phi}^{(\Delta)} + \tilde{\phi}_{,j}^{(0)}\tilde{u}_j\right)\right]_-^+ = 0, \tag{A.27}$$

$$\left[\tilde{\phi}^{(\Delta)}\right]_-^+ = 0, \tag{A.28}$$

$$\left[n_i^{(0)}(\tilde{\phi}_{,i}^{(\Delta)} - 4\pi G\rho\tilde{u}_i)\right]_-^+ = 0. \tag{A.29}$$

Following *Wolf* (1994) and introducing the (Laplace transformed) rotation, defined by[2]

$$\tilde{\omega}_k = \frac{1}{2}\epsilon_{ijk}\tilde{u}_{k,j}, \tag{A.30}$$

eq. (A.23) becomes, with eq. (A.22)

$$\tilde{P}_{,i}^{(\partial)} + 2s\tilde{m}\epsilon_{ijk}\tilde{\omega}_{k,j} = 0, \tag{A.31}$$

since $\tilde{u}_{i,ji} = \tilde{u}_{i,ij} = [\tilde{u}_{i,i}]_{,j} = 0$. Correspondingly, the stress continuity condition, eq. (A.27), can be expressed in terms of the pressure by inserting eq. (A.22):

$$\left[n_i^{(0)}\tilde{P}^{(\partial)} - 2s\tilde{m}\tilde{\epsilon}_{ji} + \rho n_i^{(0)}\left(\tilde{\phi}^{(\Delta)} + \tilde{\phi}_{,j}^{(0)}\tilde{u}_j\right)\right]_-^+ = 0, \tag{A.32}$$

where $\tilde{\epsilon}$ is the Laplace transformed strain tensor $\tilde{\epsilon}_{ij} = \frac{1}{2}\left(\tilde{u}_{i,j} + \tilde{u}_{j,i}\right)$.

[2]The symbol ϵ indicates both the strain tensor, when it appears with two indexes as in eq. (A.32), and the Levi-Civita tensor, when appearing with three indexes as in eq. (A.31)

A.1.5 Incremental fields and interface conditions in spherical coordinates

To make the notation less cumbersome, in the following of this chapter the $\tilde{f}$ notation to indicate the Laplace transform of a quantitiy f will be dropped. Also, the product $s\tilde{m}$ will be substituted by q. The spherical equations of the system are more readily obtained if the vectorial equations are used first. The vectorial forms of the incompressibility condition, eq. (A.21), rotation, eq. (A.30), equations of motion (A.31), and Poisson's equation (A.25) are:

$$\begin{cases} \nabla \cdot \mathbf{u} = & 0, \\ \boldsymbol{\omega} - \dfrac{1}{2}\nabla \times \mathbf{u} = & 0, \\ \nabla P^{(\partial)} + 2q\nabla \times \boldsymbol{\omega} = & 0, \\ \nabla^2 \phi^{(\Delta)} = & 0. \end{cases} \tag{A.33}$$

By applying the differential operators in spherical coordinates from Appendix B the following system of equation is directly obtained:

$$\begin{cases} \sin\theta (r^2 u_r)_{,r} + r(u_\theta \sin\theta)_{,\theta} + \dfrac{u_{\phi,\phi}}{\sin\theta} = 0, \\ 2r\omega_\lambda - (r u_\theta)_{,r} + (u_r)_{,\theta} = 0, \\ r\sin\theta P^{(\partial)}_{,r} + 2q\left[\omega_{\theta,\lambda} - (\sin\theta\, \omega_\lambda)_{,\theta}\right] = 0, \\ P^{(\partial)}_{,\theta} + 2q\left[\dfrac{\omega_{r,\lambda}}{\sin\theta} - (r\,\omega_\lambda)_{,r}\right] = 0, \\ g_r^{(\Delta)} - \phi^{(\Delta)}_{,r} = 0, \\ \sin^2\theta \left(r^2\, g_r^{(\Delta)}\right)_{,r} + \left(\sin\theta\, \phi^{(\Delta)}_{,\theta}\right)_{,\theta} + \left(\phi^{(\Delta)}_{,\lambda\lambda}\right) = 0. \end{cases} \tag{A.34}$$

where the incremental radial gravity $g_r^{(\Delta)}$ is introduced.

The interface conditions in spherical coordinates are obtained as follows. The continuity of the displacement, eq. (A.26), simply translates into the continuity

of its components:

$$[u_r]^+_- = 0, \tag{A.35}$$

$$[u_\theta]^+_- = 0 \tag{A.36}$$

$$[u_\lambda]^+_- = 0. \tag{A.37}$$

The only non zero component of $n_i^{(0)}$ is n_r, according to the assumption of an initial hydrostatic state (section A.1.1). Accordingly, the condition for the continuity of the stress across interfaces, eq. (A.32), splits into two components. If $i = j = r$ eq. (A.32) gives:

$$\left[P^{(\partial)} - 2qu_{r,r} + \rho\left(\phi^{(\Delta)} + \phi^{(0)}_{,r}u_r\right)\right]^+_- = 0 \tag{A.38}$$

If $i \neq r$, and $j = r$, then from the same equation, the only component remaining is $[q\epsilon_{r\theta}]^+_- = 0$. Using eq. (B.9) with $i = r$ and $j = \theta$, this corresponds to the condition

$$\left[q\left(u_{r,\theta} + ru_{\theta,r} - u_\theta\right)\right]^+_- = 0. \tag{A.39}$$

The continuity of the potential, eq. (A.28), is not affected by the change of coordinates, i.e.,

$$\left[\phi^{(\Delta)}\right]^+_- = 0. \tag{A.40}$$

The interface condition for the potential gradient, eq. (A.29), becomes in spherical coordinates:

$$\left[\phi^{(\Delta)}_{,r} - 4\pi G\rho u_r\right]^+_- = 0. \tag{A.41}$$

The solution of the system of partial differential equations (A.34) must satisfy, at internal interfaces, the conditions represented by equations from (A.35) to (A.41). The boundary conditions at the center and at the surface are discussed in section A.1.9.

A.1.6 Integration of the system of equations (A.34)

The forcing is given by the tidal potential described in section 1.2.3. The harmonic forcing induces harmonic perturbations. Thus the variables are written in terms of spherical harmonics $Y_n^m(\cos\theta,\lambda) = P_{nm}(\cos\theta)\exp[im\lambda]$, with n and m the degree and order of the harmonic, respectively.

$$\begin{cases} u_r(r,\theta,\lambda,s) = & \sum_{nm} U_n^m(r,s)Y_n^m(\cos\theta,\lambda), \\ u_\theta(r,\theta,\lambda,s) = & \sum_{nm} V_n^m(r,s)\dfrac{\partial Y_n^m(\cos\theta,\lambda)}{\partial\theta}, \\ u_\lambda(r,\theta,\lambda,s) = & \sum_{nm} \dfrac{V_n^m(r,s)}{\sin\theta}\dfrac{\partial Y_n^m(\cos\theta,\lambda)}{\partial\theta}, \\ \omega_r(r,\theta,\lambda,s) = & \sum_{nm} \Lambda_n^m(r,s)Y_n^m(\cos\theta,\lambda), \\ \omega_\theta(r,\theta,\lambda,s) = & \sum_{nm} \dfrac{\Omega_n^m(r,s)}{\sin\theta}\dfrac{\partial Y_n^m(\cos\theta,\lambda)}{\partial\lambda}, \\ \omega_\lambda(r,\theta,\lambda,s) = & -\sum_{nm} \Omega_n^m(r,s)\dfrac{\partial Y_n^m(\cos\theta,\lambda)}{\partial\theta}, \\ P^{(\partial)}(r,\theta,\lambda,s) = & \sum_{nm} P_n^m(r,s)Y_n^m(\cos\theta,\lambda), \\ \phi^{(\Delta)}(r,\theta,\lambda,s) = & \sum_{nm} \Phi_n^m(r,s)Y_n^m(\cos\theta,\lambda), \\ g^{(\Delta)}(r,\theta,\lambda,s) = & \sum_{nm} G_n^m(r,s)Y_n^m(\cos\theta,\lambda), \end{cases} \tag{A.42}$$

With the associated Legendre differential equation

$$\frac{d^2}{d\theta^2}P_{nm}(\cos\theta) + \cot\theta\frac{d}{d\theta}P_{nm}(\cos\theta) + \left[n(n+1) - \frac{m}{\sin^2\theta}\right]P_{nm}(\cos\theta) = 0, \tag{A.43}$$

the substitution of expressions (A.42) in the system of equations (A.34) gives:

$$\begin{cases} 2U_n^m + rU_{n,r}^m - n(n+1)V_n^m = 0, \\ U_n^m - V_n^m - rV_{n,r}^m - 2r\Omega_n^m = 0, \\ rP_{n,r}^m + 2n(n+1)\mu\Omega_n^m = 0, \\ P_n^m + 2q(\Omega_n^m + r\Omega_{n,r}^m) = 0, \end{cases} \tag{A.44}$$

$$\begin{cases} G_n^m - \Phi_{n,r}^m = 0, \\ n(n+1)\Phi_n^m - 2rG_n^m - r^2G_{n,r}^m = 0. \end{cases} \tag{A.45}$$

The braces collect the equations for the mechanical quantities, (A.44), and for the gravitational quantities, (A.45). It is costumary to scale the functions introducing the set of variables $\mathtt{y}_i$'s defined as[3]:

$$\begin{aligned} U_n^m = R\,\mathtt{y}_1, \;\; V_n^m = R\,\mathtt{y}_2, \;\; \Omega_n^m = \frac{R}{r}\,\mathtt{y}_3, \\ P_n^m = 2q\,\frac{R}{r}\,\mathtt{y}_4, \;\; \Phi_n^m = R\,\mathtt{y}_5, \;\; G_n^m = \frac{R}{r}\,\mathtt{y}_6. \end{aligned} \tag{A.46}$$

Defining $\mathbf{y}_M = [\mathtt{y}_1, \mathtt{y}_2, \mathtt{y}_3, \mathtt{y}_4]^T$ as the vector for the mechanical quantities, with the definitions (A.46), the mechanical equations of the system (A.44) can be written as:

$$\frac{d\mathbf{y}_M}{dr} = \mathbf{M}\mathbf{y}_M, \text{ where } \mathbf{M} = \begin{bmatrix} -\frac{2}{r} & \frac{n(n+1)}{r} & 0 & 0 \\ \frac{1}{r} & -\frac{1}{r} & \frac{2}{r} & 0 \\ 0 & 0 & 0 & -\frac{1}{r} \\ 0 & 0 & -\frac{n(n+1)}{r} & \frac{1}{r} \end{bmatrix}. \tag{A.47}$$

[3]Note that the following definitions differs from those introduced by *Alterman et al.* (1959) where a similar approach was first developed.

Assume power solutions for the $\mathtt{y}_i$'s, $\mathtt{y}_i = r^{k^{(j)}}\mathtt{y}_i^{(j)}$, where j is an index, and $\mathtt{y}_i^{(j)}$ is a constant. With these definitions, eq. (A.47) becomes

$$\begin{bmatrix} 2+k^{(j)} & -n(n+1) & 0 & 0 \\ 1 & -k^{(j)}-1 & -2 & 0 \\ 0 & 0 & k^{(j)} & 1 \\ 0 & 0 & n(n+1) & k^{(j)}-1 \end{bmatrix} \begin{bmatrix} \mathtt{y}_1^{(j)} \\ \mathtt{y}_2^{(j)} \\ \mathtt{y}_3^{(j)} \\ \mathtt{y}_4^{(j)} \end{bmatrix} = \begin{bmatrix} 0 \\ 0 \\ 0 \\ 0 \end{bmatrix}. \tag{A.48}$$

The system so expressed has non-trivial solutions if the determinant vanishes, i.e., if

$$[-(2+k^{(j)})(k^{(j)}+1)+n(n+1)][k^{(j)}(k^{(j)}-1)-n(n+1)] = 0, \tag{A.49}$$

whose roots, which correspond to the eigenvalues, are:

$$\begin{aligned} k^{(1)} &= n-1, \quad k^{(3)} = -(n+2), \\ k^{(2)} &= n+1, \qquad k^{(4)} = -n. \end{aligned} \tag{A.50}$$

The mechanical quantities are defined only for $r \leq R$, and since in the tidal problem $n \geq 2$, two solutions are irregular at the origin. The boundary conditions at the center, $r = 0$, avoid this singularity (Sec. A.1.9). The general solution for each mechanical variable $\mathtt{y}_i$ of $\mathtt{y}_M$ is then a combination of the four solutions:

$$\mathtt{y}_i = \sum_{j=1}^{4} C^{(j)} r^{k^{(j)}} \mathtt{y}_i^{(j)}, \tag{A.51}$$

with $C^{(j)}$ representing the constants of integration and $\mathtt{y}_i^{(j)}$ the eigenvectors corresponding to the eigenvalues (A.50).

Similarly, defining for the gravitational quantities $\mathbf{y}_G = [\mathtt{y}_5, \mathtt{y}_6]^T$, the corresponding equations of the system (A.45) can be cast in matrix form:

$$\frac{d\mathbf{y}_G}{dr} = \mathbf{G}\mathbf{y}_G, \text{ where } \mathbf{G} = \begin{bmatrix} 0 & \frac{1}{r} \\ \frac{n(n+1)}{r} & -\frac{1}{r} \end{bmatrix}. \tag{A.52}$$

As done for the mechanical quantities, using power series solutions, $\mathtt{y}_i = r^{k^{(j)}}\mathtt{y}_i^{(j)}$, the system of equations reduces to the solution of the matrix equation:

$$\begin{bmatrix} k^{(j)} & -1 \\ n(n+1) & -k^{(j)}-1 \end{bmatrix} = \begin{bmatrix} \mathtt{y}_5^{(j)} \\ \mathtt{y}_6^{(j)} \end{bmatrix} = \begin{bmatrix} 0 \\ 0 \end{bmatrix}. \tag{A.53}$$

The corresponding eigenvalues are

$$k^{(5)} = n, \quad k^{(6)} = -(n+1). \tag{A.54}$$

The general solution for the gravitational variables $\mathtt{y}_i$ of $\mathtt{y}_G$ is then a combination of the two solutions:

$$\mathtt{y}_i = \sum_{j=5}^{6} C^{(j)} r^{k^{(j)}} \mathtt{y}_i^{(j)}, \tag{A.55}$$

with $C^{(j)}$ representing the constants of integration and $\mathtt{y}_i^{(j)}$ the eigenvectors corresponding to the eigenvalues (A.54).

For a homogeneous spherically symmetric layer, using equations (A.50), (A.51), (A.54), and (A.55), the solution can be written as:

$$\mathtt{y} = \mathbf{P}\mathbf{C}, \tag{A.56}$$

where

$$\mathtt{y} = \begin{bmatrix} \mathtt{y}_M \\ \mathtt{y}_G \end{bmatrix} = [\mathtt{y}_1, \mathtt{y}_2, \mathtt{y}_3, \mathtt{y}_4, \mathtt{y}_5, \mathtt{y}_6]^T, \tag{A.57}$$

$$\mathbf{P} = \begin{bmatrix} nr^{(n-1)} & n(n+1)r^{(n+1)} & n(n+1)r^{-n} & (n+1)r^{-(n+2)} & 0 & 0 \\ r^{(n-1)} & (n+3)r^{(n+1)} & (2-n)r^{-n} & -r^{-(n+2)} & 0 & 0 \\ 0 & -(2n+3)r^{(n+1)} & (2n-1)r^{-n} & 0 & 0 & 0 \\ 0 & (n+1)(2n+3)r^{(n+1)} & n(2n-1)r^{-n} & 0 & 0 & 0 \\ 0 & 0 & 0 & 0 & r^n & r^{-(n+1)} \\ 0 & 0 & 0 & 0 & nr^n & -(n+1)r^{-(n+1)} \end{bmatrix} \tag{A.58}$$

and

$$\mathbf{C} = [C^{(1)}, C^{(2)}, C^{(3)}, C^{(4)}, C^{(5)}, C^{(6)}]^T \tag{A.59}$$

is the vector of integration constants.

A.1.7 Interface conditions in matrix form

The same procedure used to derive the systems of equations (A.44) and (A.45) can be used to cast the internal interfaces conditions, eq. (A.35) to (A.41), as:

$$[U_n^m]_-^+ = 0, \tag{A.60}$$

$$[V_n^m]_-^+ = 0, \tag{A.61}$$

$$\left[P_n^m - 2qU_{n,r}^m + \rho\left(\Phi_n^m + g_r^{(0)}U_n^m\right)\right]_-^+ = 0, \tag{A.62}$$

$$\left[q\left(U_n^m + rV_{n,r}^m - V_n^m\right)\right]_-^+ = 0, \tag{A.63}$$

$$[\Phi_n^m]_-^+ = 0, \tag{A.64}$$

$$[G_n^m - 4\pi G\rho U_n^m]_-^+ = 0. \tag{A.65}$$

With the definitions given in (A.46), the continuity of the displacement, Eq. (A.60) and (A.61), of the potential, Eq. (A.64), and of the potential gradient, Eq. (A.65), simply translates into the conditions:

$$[\mathtt{y}_1]_-^+ = 0, \tag{A.66}$$

$$[\mathtt{y}_2]_-^+ = 0, \tag{A.67}$$

$$[\mathtt{y}_5]_-^+ = 0, \tag{A.68}$$

$$\left[\frac{\mathtt{y}_6}{r} - 4\pi\rho G\mathtt{y}_1\right]_-^+ = 0. \tag{A.69}$$

The terms $U_{n,r}$ and $V_{n,r}$ in the third and fourth interface conditions can be eliminated by using the first and second equation in (A.44). Thus Eq. (A.62) and

(A.63) become:

$$\left[\frac{2\mu}{r}\mathtt{y}_4+\frac{4\mu}{r}\mathtt{y}_1-\frac{2\mu}{r}n(n+1)\mathtt{y}_2+\rho\mathtt{y}_5+\rho g\mathtt{y}_1\right]_-^+=0, \tag{A.70}$$

$$\left[\mu\left(\mathtt{y}_1-\mathtt{y}_2-\mathtt{y}_3\right)\right]_-^+=0. \tag{A.71}$$

If $\mathtt{y}^+$ and $\mathtt{y}^-$ represent the solution vectors above and below the boundary at r^-, the interface conditions just derived allow to link $\mathtt{y}^+$ to $\mathtt{y}^-$ as:

$$\mathtt{y}^+(r^-)=\mathbf{B}(r^-)\mathtt{y}^-(r^-), \tag{A.72}$$

where the boundary matrix $\mathbf{B}$, using Eq. (A.66) to (A.71), is

$$\mathbf{B}=\begin{bmatrix} 1 & 0 & 0 & 0 & 0 & 0\\ 0 & 1 & 0 & 0 & 0 & 0\\ -\frac{\Delta q}{q^+} & \frac{\Delta q}{q^+} & \frac{q^-}{q^+} & 0 & 0 & 0\\ \left(\frac{2\Delta q}{q^+}+\frac{\Delta\rho r^- g^{(0)}_{r^-}}{2q^+}\right) & -n(n+1)\frac{\Delta q}{q^+} & 0 & \frac{q^-}{q^+} & \frac{\Delta\rho r^-}{2q^+} & 0\\ 0 & 0 & 0 & 0 & 1 & 0\\ -4\pi G r^-\Delta\rho & 0 & 0 & 0 & 0 & 1 \end{bmatrix}. \tag{A.73}$$

where the notation Δf indicates f^+-f^-.

A.1.8 Propagator matrix technique

According to the results of Sec. A.1.6, the system of equations for a spherically symmetric planet can be cast as:

$$\frac{d\mathbf{y}}{d\mathbf{r}}=\mathbf{A}\mathbf{y}. \tag{A.74}$$

The general solution is written, Eq. (A.56), as $\mathbf{y}(r)=\mathbf{P}(r,s)\mathbf{C}$, where the vector $\mathbf{C}$ represents the six constants of integration. The planetary models used in this study (section 2.4.1) are made of a series of constant property layers. The interface conditions, eq. (A.35) to (A.41), can be expressed through the

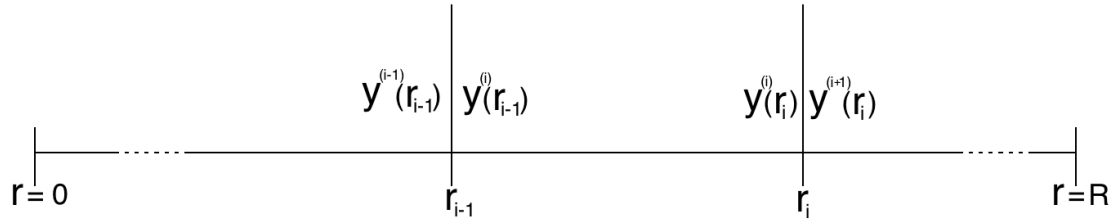

Figure A.1: Schematic structure of the vector of solution y and radius r for a planetary model. The center of the planet is at $r = 0$, the surface at $r = R$. Each homogeneous layer is indicated by the index corresponding to the outer boundary of the layer.

boundary matrix $\mathbf{B}$, Eq. (A.73), which connects the solutions on the two sides of a boundary. With reference to the interface at $r = r_{i-1}$ in Figure A.1, the two solutions to be matched are:

$$\mathbf{y}^{(i)}(r_{i-1}) = \mathbf{P_i}(r_{i-1}, s)\mathbf{C}^{(i)}, \tag{A.75}$$

$$\mathbf{y}^{(i-1)}(r_{i-1}) = \mathbf{P_{i-1}}(r_{i-1}, s)\mathbf{C}^{(i-1)}. \tag{A.76}$$

The interface matrix $\mathbf{B}(r_{i-1}, s)$ provides the connection between the two solutions:

$$\mathbf{y}^{(i)}(r_{i-1}) = \mathbf{B}(r_{i-1}, s)\mathbf{y}^{(i-1)}(r_{i-1}). \tag{A.77}$$

With the last three expressions the vector of constants $\mathbf{C}^{(i)}$ can be expressed in terms of the vector of constants $\mathbf{C}^{(i-1)}$:

$$\mathbf{C}^{(i)} = \left[\mathbf{P_i}(r_{i-1}, s)\right]^{-1} \mathbf{B}(r_{i-1}, s)\mathbf{P_{i-1}}(r_{i-1}, s)\mathbf{C}^{(i-1)}. \tag{A.78}$$

From eq. (A.75) and (A.78), the solution for $\mathbf{y}^{(i)}$ at $r = r_i$ is

$$\mathbf{y}^{(i)}(r_i, s) = \mathbf{P_i}(r_i, s)\left[\mathbf{P_i}(r_{i-1}, s)\right]^{-1} \mathbf{B}(r_{i-1}, s)\mathbf{P_{i-1}}(r_{i-1}, s)\mathbf{C}^{(i-1)}, \tag{A.79}$$

and the vector of integration constant $\mathbf{C}^{(i)}$ does not appear anymore. By extending this approach to each layer, the solution $\mathbf{y}^{(N)}$ at r_N can then be written as

the product of a sequence of terms and the vector of constants at the center of the planet:

$$\mathbf{y}^{(N)}(r_N) = \left\{ \prod_{k=2}^{N} \mathbf{P_k}(r_k) \left[\mathbf{P_k}(r_{k-1})\right]^{-1} \mathbf{B}(r_{k-1}) \right\} \mathbf{P_1}(r_1)\mathbf{C}^{(1)}. \tag{A.80}$$

A.1.9 Boundary conditions

Six constants of integration are required for a solution of the system of equations (A.74). Three are imposed at the center of the planet, where the displacement ($\mathbf{y}_1$ and $\mathbf{y}_2$) and the incremental potential ($\mathbf{y}_5$) are zero. Three are imposed at the surface, which is a free surface, and thus it has to be stress free ($\mathbf{y}_3$ and $\mathbf{y}_4$ are zero). The boundary condition on the gravity is obtained by the continuity of the gravitational potential across the surface. The variable y_5 is proportional to the radial part of $\phi^{(\Delta)}$, and it is the sum of the tidal component, $\mathrm{y}_5^{\mathrm{t}}$, and the deformation component, $\mathrm{y}_5^{\mathrm{d}}$. For $r < R$ the normalized potential of deformation is (*Takeuchi et al.*, 1962):

$$\mathrm{y}_5^{\mathrm{d}}(r \leq R) = \mathrm{y}_5 - \mathrm{y}_5^{\mathrm{t}} = \left[\mathrm{y}_5(r) - \left(\frac{r}{R}\right)^n\right]. \tag{A.81}$$

For $r > R$, the deformation potential is a harmonic function with general solution $\mathrm{y}_5(r > R) \propto A(r/R)^n + B(r/R)^{-(n+1)}$. The constant A has to be zero in order for the potential to go to zero for $(r/R) \to \infty$. The potential is a continuous function, and the constant B has to match the value of the potential at the surface, which from eq. (A.81) for $r = R$, is $\mathrm{y}_5^{\mathrm{d}} = [\mathrm{y}_5(R) - 1]$. Thus:

$$\mathrm{y}_5^{\mathrm{d}}(r > R) = [\mathrm{y}_5(R) - 1] \left(\frac{r}{R}\right)^{-(n+1)}. \tag{A.82}$$

The above descriptions of the potential above and below the surface of the planet allows to derive the continuity condition for the potential gradient. The difference between the potential gradient above and below the surface has to be equal to

$-4\pi G\rho u_r$ (from the Gauss law applied across the surface) The gradients are obtained from eq. (A.81) and eq. (A.82). The condition is thus:

$$\frac{d\mathtt{y}_5}{dr} - 4\pi\rho G u_r + \frac{n+1}{R}\mathtt{y}_5 = \frac{2n+1}{R}. \tag{A.83}$$

The previous expression in terms of $\mathtt{y}_6$ and $\mathtt{y}_1$ becomes[4] :

$$\mathtt{y}_6 - 4\pi\rho G R\mathtt{y}_1 + \frac{n+1}{R}\mathtt{y}_5 = \frac{2n+1}{R}. \tag{A.84}$$

A.2 Physical properties of terrestrial material

The material properties enter the solution of the viscoelastic models described in section A.1 through the stress-relaxation function $m(t-t')$ and the density ρ (see, e.g., eq. (A.10) and (A.11)). In general the rheological behavior is mostly controlled by thermally activated processes (e.g., *Karato*, 2008) and the rheological characterization of a planetary model requires the determination of a temperature profile. We obtain this temperature profile under the assumption that heat is transported via conduction in the mantle and in the crust. The assumption of conductive transport in the mantle of Mercury is further discussed in section 2.4.2.

In this section we report one particular solution for the heat conduction equation that is not readily available in the literature. We also discuss the Maxwell and the Andrade rheological models that will be used to model the tidal response of the subsurface materials of Mercury.

[4]Note that different authors have defined $\mathtt{y}_6$ in different ways. For example *Alterman et al.* (1959) defines $\mathtt{y}_6 = (d\mathtt{y}_5/dr) - 4\pi\rho G u_r$, while *Tobie et al.* (2005) define $\mathtt{y}_6$ as the left hand side of eq. (A.83).

A.2.1 Solution of the heat conduction equation in spherical coordinates with heat sources

We are interested in the conductive temperature profile in a spherical shell with the presence of heat sources. The equation to be solved is (e.g., *Turcotte and Schubert*, 2002):

$$k\frac{1}{r^2}\frac{d}{dr}\left(r^2\frac{dT}{dr}\right)+\rho H=0, \tag{A.85}$$

where k is the conductivity, ρ is the density, and H is the heat production rate. The solution of equation (A.85) for the case of constant H if found in the literature (e.g., *Turcotte and Schubert*, 2002):

$$T=c_2-\frac{c_1}{r}-\frac{1}{6}\frac{\rho H}{k}r^2, \tag{A.86}$$

where c_1 and c_2 are two constants of integration.

We report here the solution for the case of exponential profile for H, $H = H_0\exp\left[(r-R)/h\right]$, where H_0 is a constant, h is the length scale, and R is the outer radius of the shell. By defining $A=\frac{\rho H_0}{k}\exp\left[-\frac{R}{h}\right]$, equation (A.85) becomes:

$$\frac{d}{dr}\left(r^2\frac{dT}{dr}\right)+Ar^2\exp\left[\frac{r}{h}\right]=0. \tag{A.87}$$

A first integration gives

$$\frac{dT}{dr}+hA\exp\left[\frac{r}{h}\right]\left[1-2\left(\frac{h}{r}\right)+2\left(\frac{h}{r}\right)^2\right]=\frac{c_1}{r^2}, \tag{A.88}$$

with c_1 a constant of integration. The second term on the left hand side is obtained by twice applying integration by parts to the corresponding term in equation (A.87). Defining $x=r/h$, a second integration involves the solution of the following integrals:

$$\mathbb{I}_1 = \int\frac{1}{x}\exp(x)dx, \tag{A.89}$$

$$\mathbb{I}_2 = \int\frac{1}{x^2}\exp(x)dx=-\frac{1}{x}\exp(x)+\mathbb{I}_1. \tag{A.90}$$

$\mathbb{I}_1$ has no analytical solution, but the integration of (A.88) gives:

$$T + h^2 A \left\{ \int \exp(x) \left[1 - 2\left(\frac{1}{x}\right) + +2\left(\frac{1}{x}\right)^2 \right] d(x) \right\} = -\frac{c_1}{r} + c_2, \quad \text{(A.91)}$$

$$T + h^2 A \left[\exp(x) - 2\mathbb{I}_1 + 2\mathbb{I}_2 \right] = -\frac{c_1}{r} + c_2, \quad \text{(A.92)}$$

$$T + h^2 A \exp\left(\frac{h}{r}\right) \left[1 - 2\left(\frac{r}{h}\right) \right] = -\frac{c_1}{r} + c_2, \quad \text{(A.93)}$$

with c_2 a second constant of integration. The solution is analytical since the terms proportional to $\mathbb{I}_1$ cancel out.

A.2.2 Rheological models

The response of planetary materials to an applied forcing strongly depends on the timescale of the forcing, much like the case of the Silly Putty® (Figure A.2). The response is elastic-like at short timescales and fluid-like at long timescales. There are several models that capture this long- and short-timescale behavior. We describe below the Maxwell and the Andrade model, which we use in Chapter 2 to model the tidal response of Mercury.

A.2.3 Maxwell rheological model

In one dimension the Maxwell model is constructed by a series connection of an elastic element (Hookean spring) and a viscous element (dashpot). It is completely defined by two parameters, the unrelaxed (infinite-frequency) rigidity $\mu_{\rm U}$ of the spring, which has units of Pa, and the dynamic viscosity ν of the dashpot, which has units of Pa s. This implicitly introduces a timescale in the system, the Maxwell time, defined as

$$\tau_{\rm M} = \frac{\nu}{\mu_{\rm U}}, \quad \text{(A.94)}$$

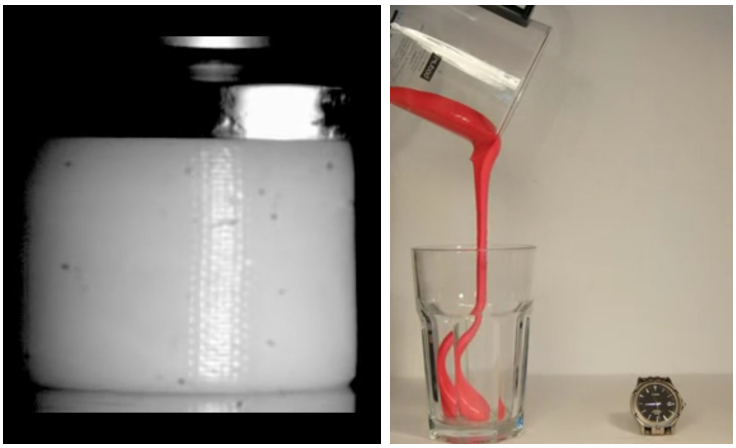

Figure A.2: Silly Putty® behaves as an elastic solid on short timescales (left, drop-weight impact test on a white cylinder of Silly Putty®) and as a fluid over long timescales (right). This timescale-dependent behavior is qualitatively similar to the response of mantle materials. Credit: http://youtu.be/ZShiIA30jXU and http://youtu.be/wrpgq7WHtgU

which is a timescale that separates the elastic regime (forcing period $\ll \tau_{\rm M}$) from the fluid regime (forcing period $\gg \tau_{\rm M}$).

We derive here the three-dimensional stress-strain relation for a Maxwell body. Even if we do not employ it for the results presented in Chapter 2, it is required for the calculation of the tidal dissipation in the interior of a planet (section 5.2). The three-dimensional stress-strain relation for a Maxwell body is obtained by combining the elastic response of the axial component with the viscoelastic response of the deviatoric component. From the relation:

$$\epsilon_{xx} = \frac{1}{E}\left[\sigma_{xx} - \nu\left(\sigma_{yy} + \sigma_{zz}\right)\right], \tag{A.95}$$

with E the Young's modulus and ν the Poisson's ratio, the stress-strain relationship for the average normal stress $\sigma_v = \sigma_{kk}/3$, is

$$\epsilon_v = \frac{1}{3K}\sigma_v, \tag{A.96}$$

where $K = E/[3(1-2\nu)]$ is the bulk modulus. For the shear component, the stress-strain relation is obtained under the condition that the total strain is the sum of the strain of the spring ($\epsilon = \sigma/2\mu$) and of the dashpot[5] ($\dot{\epsilon} = \sigma/2\eta$):

$$d_{ij,t} = \frac{1}{2\mu}\tau_{ij,t} + \frac{1}{2\eta}\tau_{ij}, \tag{A.97}$$

where the deviatoric strain and stress are $d_{ij} = \epsilon_{ij} - \epsilon_v\delta_{ij}$ and $\tau_{ij} = \sigma_{ij} - \sigma_v\delta_{ij}$. With these definitions equation (A.97) can be rewritten as:

$$\epsilon_{ij,t} - \frac{1}{3}\epsilon_{kk,t}\delta_{ij} = \frac{1}{2\mu}\left[\sigma_{ij,t} - \frac{1}{3}\sigma_{kk,t}\delta_{ij}\right] + \frac{1}{2\eta}\left[\sigma_{ij} - \frac{1}{3}\sigma_{kk}\delta_{ij}\right]. \tag{A.98}$$

Rearranging and using the time derivative of equation (A.96) gives:

$$\sigma_{ij,t} + \left(\frac{\mu}{\eta}\right)\left[\sigma_{ij} - \frac{1}{3}\sigma_{kk}\delta_{ij}\right] = 2\mu\epsilon_{ij,t} + \left[K - \frac{2}{3}\mu\right]\epsilon_{kk,t}\delta_{ij}, \tag{A.99}$$

which agrees with equation (11) in *Tobie et al.* (2005) and equation (2) in *Peltier* (1974).

A.2.4 Andrade rheological model

The Maxwell rheological model is in many cases unable to reproduce both laboratory and field data (see section 2.3.1), and alternative rheological models have been proposed. Using the work of *Jackson et al.* (2010) as a guide we considered the Extended Burgers (EB) model and the Andrade Pseudo-period (AP) model. The work of *Jackson et al.* (2010) focuses on the EB model because of its ability to fit laboratory data at both short and long timescales. However the fit at the long-timescale, more relevant to the tidal timescales, is similar for the two models and we choose the AP model for its smaller number of parameters (additional

[5]In many textbooks the factor 2 does not appear (e.g., *Findley et al.*, 1983), since only the one dimensional problem is treated. The factor 2 comes from the fact that the relation is valid for the angle change γ_{ij} induced by the shear, and $\gamma_{ij} = 2\epsilon_{ij}$.

motivations for this choice are described in section 2.3). In the following sections we describe how we tested the performance of the AP model against the fit obtained with the EB model described in the paper by *Jackson et al.* (2010).

A.2.4.1 Calculation of $J(\omega)$ with the Andrade-pseudoperiod model of *Jackson et al.* (2010)

Calculating the rheological properties of a material using the AP model requires the evaluation of the real and imaginary parts of the frequency-dependent complex compliance J, equations (2.5) and (2.6), and of the master variable X_B, equation (2.7). We report here their expressions for clarity:

$$J_{\mathrm{R}}(\omega) = \frac{1}{\mu_{\mathrm{U}}}\left\{1 + \beta^{*}\Gamma(1+n)\omega^{-\mathrm{n}}\cos\left(\frac{n\pi}{2}\right)\right\}, \tag{A.100}$$

$$J_{\mathrm{I}}(\omega) = \frac{1}{\mu_{\mathrm{U}}}\left\{\beta^{*}\Gamma(1+n)\omega^{-\mathrm{n}}\sin\left(\frac{n\pi}{2}\right) + \frac{1}{\omega\tau_{\mathrm{M}}}\right\}, \tag{A.101}$$

$$X_{\mathrm{B}} = T_0\left(\frac{d}{d_{\mathrm{R}}}\right)^{-\mathrm{m}}\exp\left[\left(\frac{-E_{\mathrm{B}}}{R}\right)\left(\frac{1}{T}-\frac{1}{T_{\mathrm{R}}}\right)\right]\times \\ \times\exp\left[\left(\frac{-V}{R}\right)\left(\frac{P}{T}-\frac{P_{\mathrm{R}}}{T_{\mathrm{R}}}\right)\right]. \tag{A.102}$$

The pseudo-period master variable X_B includes the rheological effects of temperature T, grainsize d, and pressure P. The frequency is indicated with ω, a subscript R indicates a reference value (they are listed in Table 2.1), T_0, E_{B}, and V are constants, and m characterize the dependence on the grain size, which in principle can be different for anelastic processes (m_{a}) and for viscous relaxation (m_{v}). In calculating the imaginary part of the compliance $J_{\mathrm{I}}(\omega)$, equation (A.101), we keep the value of τ_{M} equal to the reference value reported in Table 1 of *Jackson et al.* (2010) ($\log\tau_{\mathrm{MR}} = 5.3$). This approach allows us to reproduce accurately the fits shown in Figure 1 of *Jackson et al.* (2010), which are shown in Figure A.3.

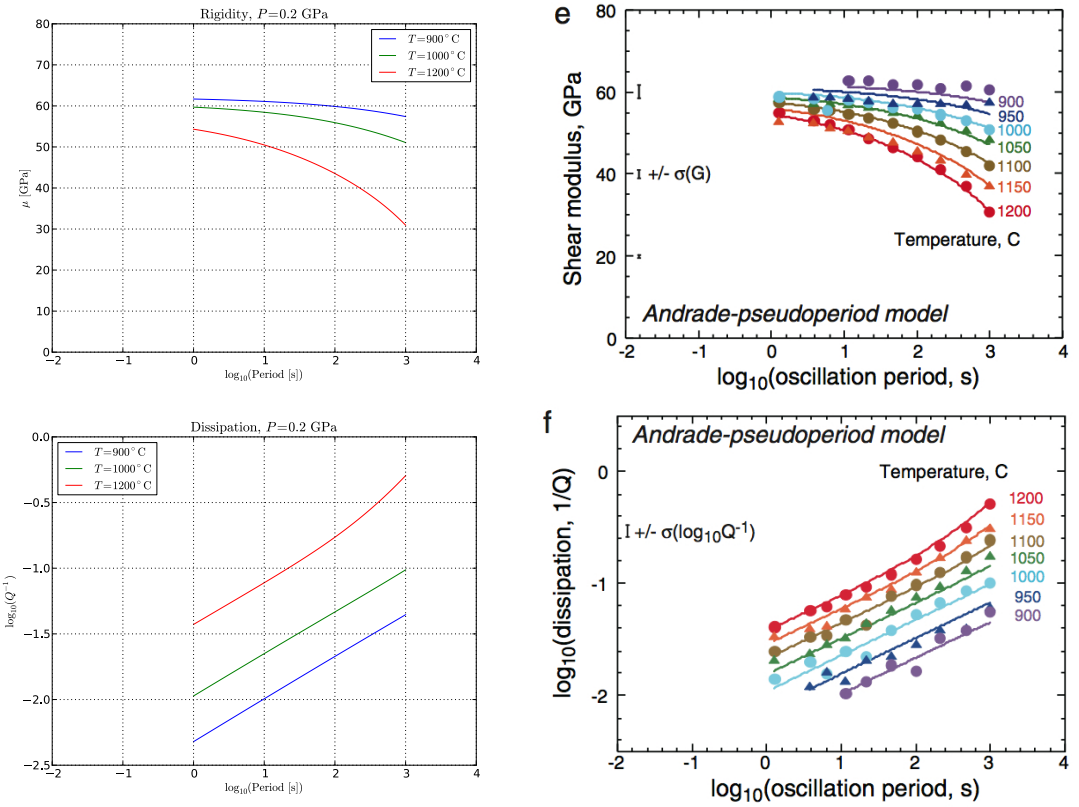

Figure A.3: Rigidity μ (top) and inverse quality factor Q^{-1} (bottom) as a function of the forcing period, obtained to test the agreement of our model (left) with panels *e* and *f* of Figure 1 of *Jackson et al.* (2010), (right). The "Shear modulus" in the figures of *Jackson et al.* (2010) corresponds to our "rigidity μ".

We also applied the AP model to the data shown in Figure 2 of *Jackson et al.* (2010), to compare the AP model with the EB model for different grain-sizes. In doing so we identified the parameter α in Table 2 of *Jackson et al.* (2010) with the parameter n of the Andrade model, as suggested in Sec 4.2 of *Jackson et al.* (2010). Figure A.4 shows the results for the two specimens #6381 (d=2.9μm) and #6328 (d=165.1μm). The prediction of the Andrade is comparable to the fit obtained with the EB model. For the specimen #6328 at $T = 1200$ °C the rigidity of the Andrade is a little higher than for the EB, but the data for $T = 1200$ °C

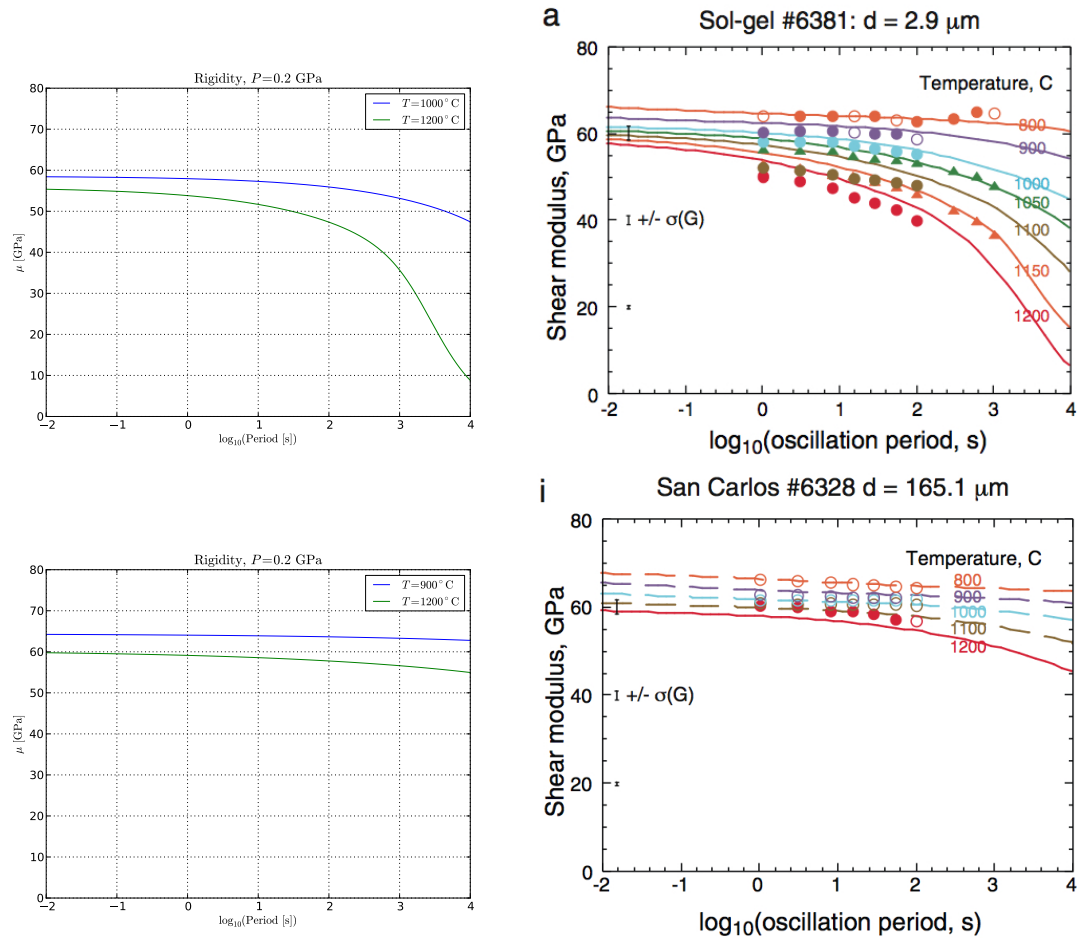

Figure A.4: Rigidity μ as a function of the forcing period for specimen 6381 (top) and 6328 (bottom), obtained to test the agreement of our model (left) with panels *a* and *i* of Figure 2 of *Jackson et al.* (2010) (right). The curves are obtained with the parameters in the top part of Table 2 of *Jackson et al.* (2010), where we identified α of the EB model with the parameter n of the AP model.

in panel *i* of Figure 2 in *Jackson et al.* (2010) show the same behavior.

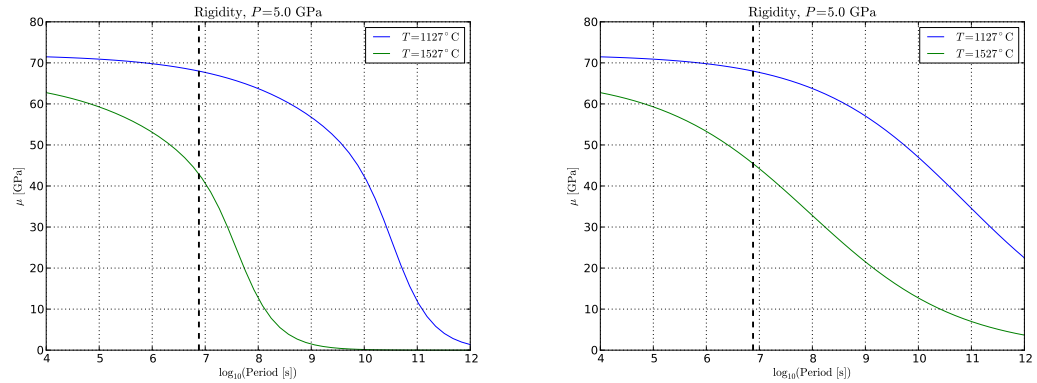

Figure A.5: Rigidity μ as a function of the forcing period. Effect of the grain size exponent m. (Left) $m_a = m_v = 1.31$. (Right) $m_a = 1.31$, $m_v = 3$. The dashed line indicates the forcing period of Mercury's tide.

A.2.4.2 Effects of the difference between $m_\mathbf{a}$ and $m_\mathbf{v}$

We include the effects of different grain-size dependence for anelastic and viscous relaxation by defining two pseudo-period master variables, one for anelastic processes, X_B^a, and one for viscous relaxation, X_B^v, with corresponding ω_a and ω_v. Thus equations (A.100) and (A.101) can be rewritten as

$$J_{\mathrm{R}}(\omega) = \frac{1}{\mu_{\mathrm{U}}}\left\{1 + \beta^*\Gamma(1+n)\omega_a^{-n}\cos\left(\frac{n\pi}{2}\right)\right\}, \tag{A.103}$$

$$J_{\mathrm{I}}(\omega) = \frac{1}{\mu_{\mathrm{U}}}\left\{\beta^*\Gamma(1+n)\omega_a^{-n}\sin\left(\frac{n\pi}{2}\right) + \frac{1}{\omega_v\tau_M}\right\} \tag{A.104}$$

Following the parameters explored in *Jackson et al.* (2010) we tested the case of $m_a = m_v = 1.31$ and the case of $m_a = 1.31$ and $m_v = 3$. Since m_v controls the transition to the viscous behavior, differences in these two cases appear at large periods. Nevertheless there is not much difference at the frequency considered for Mercury. This is shown in Figures A.5 and A.6 for the rigidity μ and Q^{-1}, respectively.

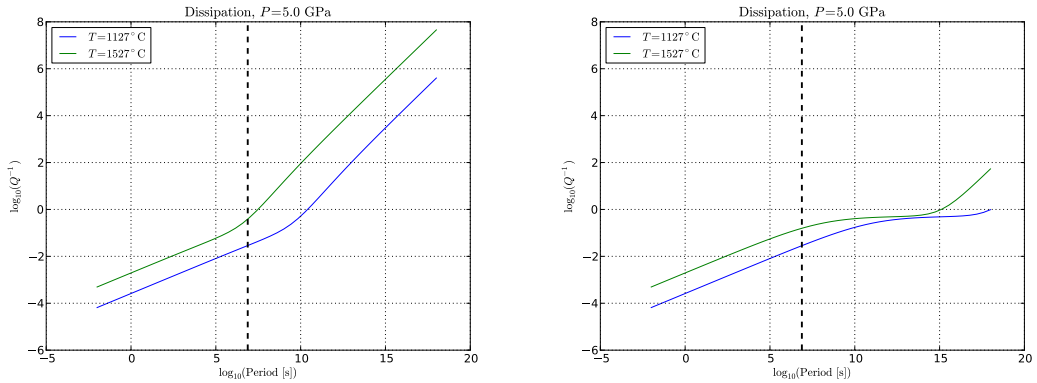

Figure A.6: Dissipation as a function of the forcing period. Effect of the grain size exponent m. (Left) $m_a = m_v = 1.31$. (Right) $m_a = 1.31$, $m_v = 3$. The dashed line indicates the forcing period of Mercury's tide.

A.2.4.3 The viscosity

Once the complex compliance is calculated, the rigidity is obtained from

$$\mu(\omega) = \left[J_{\rm R}^2(\omega) + J_{\rm I}^2(\omega)\right]^{-1/2}. \tag{A.105}$$

Since we keep $\tau_M = \tau_{MR}$ and include T, P, and d effects in the pseudo-period master variable, we do not need to make assumptions on the viscosity. We get the dynamic viscosity from the imaginary component of the compliance, $\nu = 1/(J_{\rm I}\omega)$, i.e., it is the viscosity of a Maxwell body with the same rheological response of the Andrade model. Note however that the viscosity mostly affects $\mathrm{Im}(k_2)$, not its real part. For example, we compared the values of k_2 for a model with a homogeneous elastic mantle ($\nu = 10^{21}$ Pa s) with a model where the mantle has a viscosity of 2×10^{18} Pa s. The relative difference in $\mathrm{Re}(k_2)$ is $< 10^{-3}$, but it is $\sim 5 \times 10^2$ in $\mathrm{Im}(k_2)$.

APPENDIX B

Useful operator and tensor expressions

The following list of useful relations is reproduced from *Malvern* (1969). In a orthogonal curvilinear coordinate system, the divergence of a vector $\mathbf{v}$ is defined as:

$$\nabla \cdot \mathbf{v} = \frac{1}{\sqrt{g}} \sum_n \frac{\partial}{\partial x_n} \left(\frac{\sqrt{g}}{h_n} v_n \right), \tag{B.1}$$

where h_n is the scale factor and $\sqrt{g} = h_1 h_2 h_3$. The gradient operator is defined as:

$$\nabla = \sum_n \hat{e}_n \frac{1}{h_n} \frac{\partial}{\partial x_n}. \tag{B.2}$$

The curl operator of a vector $\mathbf{v}$ is

$$\nabla \times \mathbf{v} = \sum_n \left[\sum_{p,q} \epsilon_{npq} \frac{1}{h_p h_q} \frac{\partial}{\partial x_p} \left(v_q h_q \right) \right] \hat{e}_n \tag{B.3}$$

To obtain these operators in spherical coordinates, only the scale factors are required, which are

$$h_r = 1, \quad h_\theta = r, \quad , h_\phi = r \sin\theta. \tag{B.4}$$

Spherical coordinates are defined as (radius, colatitude, longitude)$=(r, \theta, \lambda)$. The gradient is:

$$\nabla = \frac{1}{r^2} \frac{\partial}{\partial r} + \frac{1}{r \sin\theta} \frac{\partial}{\partial \theta} + \frac{1}{r \sin\theta} \frac{\partial}{\partial \lambda}. \tag{B.5}$$

The Laplacian is

$$\nabla^2 = \frac{1}{r^2} \frac{\partial}{\partial r} \left(r^2 \frac{\partial}{\partial r} \right) + \frac{1}{r^2 \sin^2\theta} \frac{\partial}{\partial \theta} \left(\sin\theta \frac{\partial}{\partial \theta} \right) + \frac{1}{r^2 \sin^2\theta} \frac{\partial^2}{\partial^2 \lambda}. \tag{B.6}$$

The curl of a vector $\mathbf{v}$ is

$$\begin{aligned}\nabla \times \mathbf{v} = \frac{1}{r\sin\theta} & \left[\frac{\partial}{\partial\theta}\left(\mathbf{v}_\lambda \sin\theta\right)\right]\hat{r} + \\ \frac{1}{r} & \left[\frac{1}{\sin\theta}\frac{\partial \mathbf{v}_r}{\partial\lambda} - \frac{\partial}{\partial r}\left(r\mathbf{v}_\lambda\right)\right]\hat{\theta} + \\ \frac{1}{r} & \left[\frac{\partial}{\partial r}\left(r\mathbf{v}_\theta\right) - \frac{\partial \mathbf{v}_r}{\partial\theta}\right]\hat{\lambda} \end{aligned} \tag{B.7}$$

In a general orthogonal curvilinear coordinate system, the general expression for the strain components (*Malvern*, 1969, p. 659) is

$$\epsilon_{ii} = \frac{1}{h_i}\frac{\partial u_i}{\partial x_i} + \frac{u_j}{h_j h_i}\frac{\partial h_i}{\partial x_j} + \frac{u_k}{h_k h_i}\frac{\partial h_i}{\partial x_k}, \tag{B.8}$$

$$\epsilon_{ij} = \frac{1}{2}\left[\frac{1}{h_j}\frac{\partial u_i}{\partial x_j} + \frac{1}{h_i}\frac{\partial u_j}{\partial x_i} - \frac{1}{h_i h_j}\left(u_i\frac{\partial h_i}{\partial x_j} + u_j\frac{\partial h_j}{\partial x_i}\right)\right]. \tag{B.9}$$

A similar expression holds for the rotation:

$$-\omega_k = \Omega_{ij} = \frac{1}{2}\left[\frac{1}{h_j}\frac{\partial u_i}{\partial x_j} - \frac{1}{h_i}\frac{\partial u_j}{\partial x_i} + \frac{1}{h_i h_j}\left(u_i\frac{\partial h_i}{\partial x_j} - u_j\frac{\partial h_j}{\partial x_i}\right)\right]. \tag{B.10}$$

APPENDIX C

Effect of the inner core on the tidal response

The effect of the inner core density on the magnitude of k_2 is shown in Figure C.1. The relatively weak trend indicates that the Love number k_2 is not very sensitive to the density of the inner core. A similar plot for k_2 as a function of the ratio of the inner core radius, $r_{\rm ic}$, to the radius of the outer core, $r_{\rm oc}$, is shown in the bottom panel of Figure C.2. The results show that k_2 is independent of the ratio of inner-core radius to outer-core radius as long as the inner core is sufficiently small. The lack of shear strength of the liquid of the outer core increases the tidal response and makes it independent of the size of the inner core, as long as the radius ratio is $\lesssim$0.6.

Similarly, variations in the viscosity and rigidity of the inner core affect the value of k_2 only for those models that have a large inner core. Less than 20% of the models have a large inner core with $r_{\rm ic}/r_{oc} > 0.6$ as shown by the cumulative histogram in the top panel of Figure C.2. A very large inner core may be detectable, because it would modify the libration of Mercury (*Van Hoolst et al.*, 2012) at a level that is comparable to the current observational accuracy of the libration measurements (*Margot et al.*, 2012).

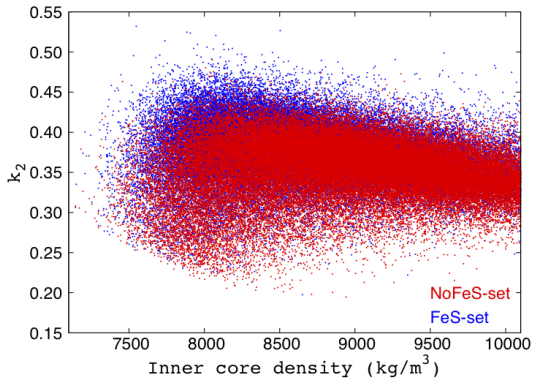

Figure C.1: Love number k_2 as a function of the inner core density. Blue and red points correspond to models with and without an FeS layer at the top of the core, respectively.

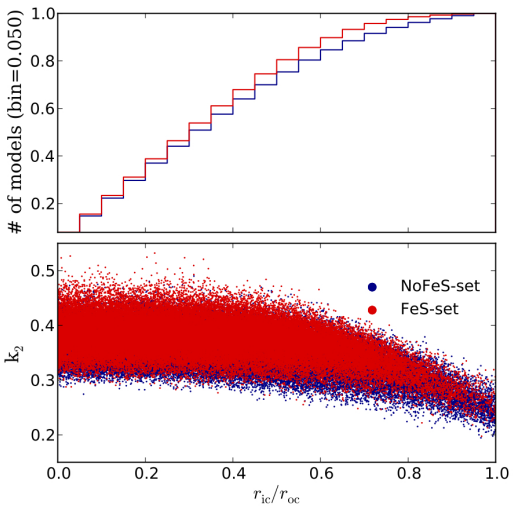

Figure C.2: (Top) Cumulative histogram of the ratio of the inner core radius $r_{\rm ic}$ to the liquid outer core radius $r_{\rm oc}$. More than 80% of the models have $r_{\rm ic}/r_{\rm oc} < 0.6$. (Bottom) k_2 as a function of the inner core radius expressed in units of outer core radius. Blue and red points correspond to models with and without an FeS layer at the top of the core, respectively. Points with an abscissa close to one correspond to models for which the outer liquid core is very thin. Models in which the core is completely solid have k_2 values that are smaller by approximately an order of magnitude (not shown).

APPENDIX D

Background materials for chapter 4

D.1 Airy isostasy on a spherical body

In the Airy isostatic compensation model for a flat crust, the weight of different columns is the same at some compensation depth. On a spherical body the convergence of the columns must be taken into account. With reference to figure D.1, H is the thickness of the crust at zero-elevation of a planet whose radius is R. The topography h is compensated at the crust-mantle boundary by the root h^*. At the compensation radius $R - \mathrm{H} - h^*$ the weight of the two columns is the same. For column 1 the contribution is

$$1: \quad \rho_\mathrm{m} \int_{R-\mathrm{H}-h^*}^{R-\mathrm{H}} r^2 dr = \rho_\mathrm{m} \left(R-\mathrm{H}\right)^2 h^* \left[1 - \left(\frac{h^*}{R-\mathrm{H}}\right) + \frac{1}{3}\left(\frac{h^*}{R-\mathrm{H}}\right)^2\right]. \quad \text{(D.1)}$$

For column 2 the contribution of the surface topography (2t) and its root (2r) has to be taken into account:

$$2\mathrm{t}: \quad \rho_\mathrm{c} \int_{R}^{R+h} r^2 dr = \rho_\mathrm{c} R^2 h \left[1 + \frac{h}{R} + \frac{1}{3}\left(\frac{h}{R}\right)^2\right], \quad \text{(D.2)}$$

$$2\mathrm{r}: \quad \rho_\mathrm{m} \int_{R-\mathrm{H}-h^*}^{R-\mathrm{H}} r^2 dr = \rho_\mathrm{m} \left(R-\mathrm{H}\right)^2 h^* \left[1 - \left(\frac{h^*}{R-\mathrm{H}}\right) + \frac{1}{3}\left(\frac{h^*}{R-\mathrm{H}}\right)^2\right]. \quad \text{(D.3)}$$

By equating the contributions of the two sectors, and under the assumption that h and h^* are much smaller than R, the relation between h^* and h for spherical

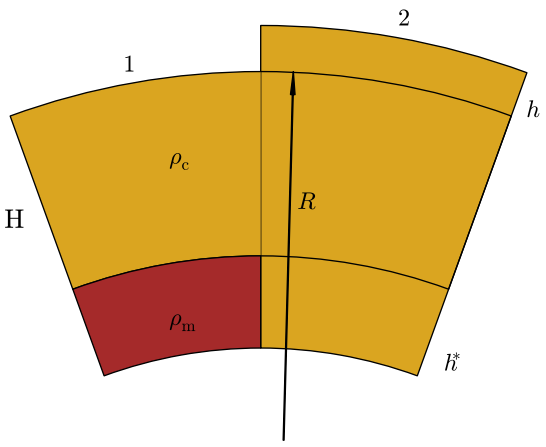

Figure D.1: Airy isostasy on a spherical planet. Golden: crustal material of density ρ_c. Brown: mantle material of density ρ_m. H is the crustal thickness at zero elevation. The topography and its root are indicated with h and h^*, respectively.

Airy isostasy is

$$h^* = \left(\frac{R}{R - \mathrm{H}}\right)^2 \frac{\rho_c}{\rho_m - \rho_c} h. \tag{D.4}$$

D.2 Potential of an irregularly shaped shell

The potential δV at a distance L from of point mass dM is

$$\delta V = \frac{G dM}{L}. \tag{D.5}$$

The factor $(1/L)$ can be expanded in spherical harmonics as[1] (e.g., *Arfken and Weber*, 2005):

$$\frac{1}{L} = \frac{1}{r}\sum_{\mathrm{n}}\left(\frac{r'}{r}\right)^{\mathrm{n}} P_{\mathrm{n}}\left(\cos\psi\right) \tag{D.6}$$

$$= \frac{1}{r}\sum_{\mathrm{inm}}\left(\frac{r'}{r}\right)^{\mathrm{n}} \frac{1}{(2n+1)} Y_{\mathrm{inm}}(\theta',\lambda') Y_{\mathrm{inm}}(\theta,\lambda), \tag{D.7}$$

where Ψ is the angle between r and r', the modules of the vectors connecting the center of the shell with the observation point and dM, respectively. In spherical coordinates the infinitesimal mass is

$$dM = (r')^2 dr' dS, \tag{D.8}$$

where dS is the solid angle. The radius of an irregularly shaped shell can be expressed as

$$r' = r_0\left[1 + \sum_{\mathrm{inm}} dr_{\mathrm{inm}} Y_{\mathrm{inm}}\right], \tag{D.9}$$

where dr_{inm} are spherical harmonics coefficients. The potential of an irregularly shaped shell can be obtained by substituting equations (D.7), (D.8), and (D.9) in equation (D.5) and integrating over the volume of the shell. Using the orthogonality properties of the spherical harmonics and at first order in dr_{inm} the potential of the shell is:

$$\Delta V = \int \delta V = \frac{4\pi G r_0^3}{r}\sum_{\mathrm{inm}} \Delta\rho \left(\frac{r_0}{r}\right)^n \frac{Y_{\mathrm{inm}}}{2n+1} dr_{\mathrm{inm}}, \tag{D.10}$$

where $\Delta\rho$ is the density contrast across the shell. By comparison with the potential written in the standard form

$$V = \frac{GM}{r}\sum_{\mathrm{inm}}\left(\frac{R}{r}\right)^n C_{\mathrm{inm}} Y_{\mathrm{inm}}, \tag{D.11}$$

[1]The convention for the coordinates is the same as in Chapter 1, therefore primed coordinates refers to the body, unprimed to the observation point. We use the compact notation Y_{inm} to indicate $P_{\mathrm{nm}}(\sin\theta)\cos\lambda$ for $i = 1$ and $P_{\mathrm{nm}}(\sin\theta)\sin\lambda$ for $i = 2$. Compare with equation 1.6.

the Stokes coefficients for the irregularly shaped shell are (*Lambeck*, 1988):

$$C_{\mathrm{inm}} = \frac{4\pi R^3}{M(2n+1)} \left(\frac{r_0}{R}\right)^{\mathrm{n}+3} \Delta\rho \, dr_{\mathrm{inm}}. \tag{D.12}$$

D.3 Admittance function for an Airy compensated crust

The topography and potential coefficients are related through the admittance function Z_{n} (e.g., *Wieczorek and Phillips*, 1997):

$$C_{\mathrm{nm}} = Z_{\mathrm{n}} h_{\mathrm{nm}}, \tag{D.13}$$

which depends on the harmonic degree n. An Airy compensated crust is characterized by a surface topography which is related to the crust-mantle interface through equation (D.4). The Stokes coefficients for the surface topography are obtained by setting $r_0 = R$ and $\Delta\rho = \rho_{\mathrm{c}}$ in equation (D.12). For the crust-mantle interface $r_0 = R - \mathrm{H}$ and $\Delta\rho = \rho_{\mathrm{m}} - \rho_{\mathrm{c}}$. By adding the contribution of surface topography and crust-mantle interface, and using the spherical Airy compensation relation, equation (D.4), the Stokes coefficients for an Airy compensated crust are

$$C_{\mathrm{nm}} = \frac{4\pi R^3}{M(2n+1)} \rho_{\mathrm{c}} \left[1 - \left(\frac{R-\mathrm{H}}{R}\right)^{\mathrm{n}}\right] h_{\mathrm{nm}}. \tag{D.14}$$

With equation (D.14) and indicating with ρ the mean density of the planet, the admittance function for Airy isostatic compensation is

$$Z_{\mathrm{n}} = \frac{3}{2n+1} \frac{\rho_{\mathrm{c}}}{\rho} \left[1 - \left(\frac{R-\mathrm{H}}{R}\right)^{\mathrm{n}}\right]. \tag{D.15}$$

This expression is necessary to infer the thickness of an Airy-compensated crust from the geoid-to-topography ratios (Chapter 4).

Bibliography

Aitta, A. (2012), Venus' internal structure, temperature and core composition, *Icarus*, *218*, 967–974, doi:10.1016/j.icarus.2012.01.007.

Alterman, Z., H. Jarosch, and C. L. Pekeris (1959), Oscillations of the Earth, *Proc. Roy. Soc. Lond., Ser. A*, *252*, 80–95, doi:10.1098/rspa.1959.0138.

Anderson, B. J., C. L. Johnson, H. Korth, R. M. Winslow, J. E. Borovsky, M. E. Purucker, J. A. Slavin, S. C. Solomon, M. T. Zuber, and R. L. McNutt Jr. (2012), Low-degree structure in Mercury's planetary magnetic field, *J. Geophys. Res. Planets*, *117*, doi:10.1029/2012JE004159.

Anderson, J. D., R. F. Jurgens, E. L. Lau, M. A. Slade, III, and G. Schubert (1996), Shape and orientation of Mercury from radar ranging data, *Icarus*, *124*, 690–697, doi:10.1006/icar.1996.0242.

Arfken, G. B., and H. J. Weber (2005), *Mathematical Methods for Physicists: A Comprehensive Guide*, 6^{th} ed., Academic Press.

Banerdt, W. B., S. Smrekar, P. Lognonné, T. Spohn, S. W. Asmar, D. Banfield, L. Boschi, U. Christensen, V. Dehant, W. Folkner, D. Giardini, W. Goetze, M. Golombek, M. Grott, T. Hudson, C. Johnson, G. Kargl, N. Kobayashi, J. Maki, D. Mimoun, A. Mocquet, P. Morgan, M. Panning, W. T. Pike, J. Tromp, T. van Zoest, R. Weber, M. A. Wieczorek, R. Garcia, and K. Hurst (2013), InSight: A Discovery mission to explore the interior of Mars, *Lunar Planet. Sci., 44, abstract 1915.*

Benz, W., W. L. Slattery, and A. G. W. Cameron (1988), Collisional stripping of Mercury's mantle, *Icarus*, *74*, 516–528, doi:10.1016/0019-1035(88)90118-2.

Beuthe, M. (2013), Spatial patterns of tidal heating, *Icarus*, *223*, 308–329, doi: 10.1016/j.icarus.2012.11.020.

Bills, B. G., and D. P. Rubincam (1995), Constraints on density models from radial moments: Applications to Earth, Moon, and Mars, *J. Geophys. Res.*, *100*, 26,305–26,316, doi:10.1029/95JE02776.

Bills, B. G., F. Nimmo, Ö. Karatekin, T. van Hoolst, N. Rambaux, B. Levrard, and J. Laskar (2009), Rotational Dynamics of Europa, in *Europa*, edited by R. T. Pappalardo, W. B. McKinnon, and K. K. Khurana, pp. 119–135, The University of Arizona Press, Tucson, Ariz.

Biot, M. A. (1954), Theory of stress-strain relations in anisotropic viscoelasticity and relaxation phenomena, *J. Appl. Phys.*, *25*, 1385–1391, doi:10.1063/1.1721573.

Borch, R. S., and H. W. Green II (1987), Dependence of creep in olivine on homologous temperature and its implications for flow in the mantle, *Nature*, *330*, 345–348, doi:10.1038/330345a0.

Bouvier, A., and M. Wadhwa (2010), The age of the Solar System redefined by the oldest Pb-Pb age of a meteoritic inclusion, *Nature Geosci.*, *3*, 637–641, doi:10.1038/ngeo941.

Běhounková, M., G. Tobie, G. Choblet, and O. Čadek (2010), Coupling mantle convection and tidal dissipation: Applications to Enceladus and Earth-like planets, *J. Geophys. Res. Planets*, *115*, E09011, doi:10.1029/2009JE003564.

Byrne, P. K., C. Klimczak, A. M. Celâl Şengör, S. C. Solomon, T. R. Watters, and S. A. Hauck, II (2014), Mercury's global contraction much greater than earlier estimates, *Nat. Geosci.*, *7*, 301–307, doi:10.1038/ngeo2097.

Cammarano, F., S. Goes, P. Vacher, and D. Giardini (2003), Inferring upper-mantle temperatures from seismic velocities, *Phys. Earth Planet. Inter.*, *138*, 197–222, doi:10.1016/S0031-9201(03)00156-0.

Charlier, B., T. L. Grove, and M. T. Zuber (2013), Phase equilibria of ultramafic compositions on Mercury and the origin of the compositional dichotomy, *Earth and Planet. Sci. Lett.*, *363*, 50–60, doi:10.1016/j.epsl.2012.12.021.

Christensen, U. R. (2006), A deep dynamo generating Mercury's magnetic field, *Nature*, *444*, 1056–1058, doi:10.1038/nature05342.

Colombo, G. (1965), Rotational Period of the Planet Mercury, *Nature*, *208*, 575, doi:10.1038/208575a0.

Colombo, G. (1966a), Cassini's second and third laws, *Astron. J.*, *71*, 891–896, doi:10.1086/109983.

Colombo, G. (1966b), Cassini's second and third laws, *Astron. J.*, *71*, 891–896, doi:10.1086/109983.

Correia, A. C. M., and J. Laskar (2004), Mercury's capture into the 3/2 spin-orbit resonance as a result of its chaotic dynamics, *Nature*, *429*, 848–850, doi:10.1038/nature02609.

Denevi, B. W., C. M. Ernst, H. M. Meyer, M. S. Robinson, S. L. Murchie, J. L. Whitten, J. W. Head, T. R. Watters, S. C. Solomon, L. R. Ostrach, C. R. Chapman, P. K. Byrne, C. Klimczak, and P. N. Peplowski (2013), The distribution and origin of smooth plains on Mercury, *J. Geophys. Res. Planets*, doi:10.1002/jgre.20075,inpress.

Efroimsky, M. (2012), Bodily tides near spin-orbit resonances, *Celestial Mechanics and Dynamical Astronomy*, *112*, 283–330, doi:10.1007/s10569-011-9397-4.

Efroimsky, M., and V. Lainey (2007), Physics of bodily tides in terrestrial planets and the appropriate scales of dynamical evolution, *J. Geophys. Res.*, *112*, E12003, doi:10.1029/2007JE002908.

Elkins-Tanton, L. T. (2012), Magma Oceans in the Inner Solar System, *Ann. Rev. Earth Pl. Sc.*, *40*, 113–139, doi:10.1146/annurev-earth-042711-105503.

Evans, L. G., P. N. Peplowski, E. A. Rhodes, D. J. Lawrence, T. J. McCoy, L. R. Nittler, S. C. Solomon, A. L. Sprague, K. R. Stockstill-Cahill, R. D. Starr, S. Z. Weider, W. V. Boynton, D. K. Hamara, and J. O. Goldsten (2012), Major-element abundances on the surface of Mercury: Results from the MESSENGER Gamma-Ray Spectrometer, *J. Geophys. Res.*, *117*, E00L07, doi:10.1029/2012JE004178.

Fassett, C. I., J. W. Head, D. M. H. Baker, M. T. Zuber, D. E. Smith, G. A. Neumann, S. C. Solomon, C. Klimczak, R. G. Strom, C. R. Chapman, L. M. Prockter, R. J. Phillips, J. Oberst, and F. Preusker (2012), Large impact basins on Mercury: Global distribution, characteristics, and modification history from MESSENGER orbital data, *J. Geophys. Res. Planets*, *117*, E00L08, doi:10.1029/2012JE004154.

Fegley, B., and A. G. W. Cameron (1987), A vaporization model for iron/silicate fractionation in the Mercury protoplanet, *Earth Planet. Sci. Lett.*, *82*, 207–222, doi:10.1016/0012-821X(87)90196-8.

Fei, Y., C. T. Prewitt, H.-K. Mao, and C. M. Bertka (1995), Structure and density of FeS at high pressure and high temperature and the internal structure of Mars, *Science*, *268*, 1892–1894, doi:10.1126/science.268.5219.1892.

Feigelson, E., and G. Babu (2012), *Modern Statistical Methods for Astronomy: With R Applications*, Cambridge University Press, Cambridge, UK.

Findley, W. N., J. S. Lai, and K. Onaran (1983), *Creep and Relaxation of Nonlinear Viscoelastic Materials*, Dover, Mineola, N. Y., 1989. 371 p.

Harder, H., and G. Schubert (2001), Sulfur in Mercury's Core?, *Icarus*, *151*, 118–122, doi:10.1006/icar.2001.6586.

Hauck, S. A., II, J.-L. Margot, S. C. Solomon, R. J. Phillips, C. L. Johnson, F. G. Lemoine, E. Mazarico, T. J. McCoy, S. Padovan, S. J. Peale, M. E. Perry, D. E. Smith, and M. T. Zuber (2013), The curious case of Mercury's internal structure, *J. Geophys. Res. Planets*, doi:10.1002/jgre.20091,inpress.

Head, J. W., C. R. Chapman, R. G. Strom, C. I. Fassett, B. W. Denevi, D. T. Blewett, C. M. Ernst, T. R. Watters, S. C. Solomon, S. L. Murchie, L. M. Prockter, N. L. Chabot, J. J. Gillis-Davis, J. L. Whitten, T. A. Goudge, D. M. H. Baker, D. M. Hurwitz, L. R. Ostrach, Z. Xiao, W. J. Merline, L. Kerber, J. L. Dickson, J. Oberst, P. K. Byrne, C. Klimczak, and L. R. Nittler (2011), Flood volcanism in the northern high latitudes of Mercury revealed by MESSENGER, *Science*, *333*, 1853–1856, doi:10.1126/science.1211997.

Hirschmann, M. M. (2000), Mantle solidus: Experimental constraints and the effects of peridotite composition, *Geochem. Geophys. Geosyst.*, *1*, 1042–1068, doi:10.1029/2000GC000070.

Hofmeister, A., and H. Mao (2003), Pressure derivatives of shear and bulk moduli from the thermal Gruneisen parameter and volume-pressure data, *Geochim. Cosmochim. Acta*, *67*, 1207–1227, doi:{10.1016/S0016-7037(02)01289-9}.

Hunter, J. D. (2007), Matplotlib: A 2d graphics environment, *Comput. Sci. Eng.*, *9*, 90–95.

Hüttig, C., and K. Stemmer (2008), Finite volume discretization for dynamic viscosities on Voronoi grids, *Phys. Earth Planet. In.*, *171*, 137–146, doi:10.1016/j.pepi.2008.07.007.

Hüttig, C., N. Tosi, and W. B. Moore (2013), An improved formulation of the incompressible Navier-Stokes equations with variable viscosity, *Phys. Earth Planet. In.*, *220*, 11–18, doi:10.1016/j.pepi.2013.04.002.

Iess, L., R. A. Jacobson, M. Ducci, D. J. Stevenson, J. I. Lunine, J. W. Armstrong, S. W. Asmar, P. Racioppa, N. J. Rappaport, and P. Tortora (2012), The tides of Titan, *Science*, *337*, 457–459, doi:10.1126/science.1219631.

Iess, L., D. J. Stevenson, M. Parisi, D. Hemingway, R. A. Jacobson, J. I. Lunine, F. Nimmo, J. W. Armstrong, S. W. Asmar, M. Ducci, and P. Tortora (2014), The gravity field and interior structure of enceladus, *Science*, *344* (6179), 78–80, doi:10.1126/science.1250551.

Jackson, I., U. H. Faul, D. Suetsugu, C. Bina, T. Inoue, and M. Jellinek (2010), Grainsize-sensitive viscoelastic relaxation in olivine: Towards a robust laboratory-based model for seismological application, *Phys. Earth Planet. In.*, *183*, 151–163, doi:10.1016/j.pepi.2010.09.005.

Jacobson, S. A., A. Morbidelli, S. N. Raymond, D. P. O'Brien, K. J. Walsh, and D. C. Rubie (2014), Highly siderophile elements in Earth's mantle as a clock for the Moon-forming impact, *Nature*, *508*, 84–87, doi:10.1038/nature13172.

James, P. B., M. T. Zuber, and R. J. Phillips (2013), Crustal thickness and support of topography on Venus, *J. Geophys. Res. Planets*, *118*, 859–875, doi:10.1029/2012JE004237.

James, P. B., M. T. Zuber, R. J. Phillips, and S. C. Solomon (2014), Support of long-wavelength topography on Mercury inferred from MESSENGER measurements of gravity and topography, *J. Geophys. Res. Planets*, Under revision.

Kampfmann, W., and H. Berckhemer (1985), High temperature experiments on the elastic and anelastic behaviour of magmatic rocks, *Phys. Earth Planet. In.*, *40*, 223–247, doi:10.1016/0031-9201(85)90132-3.

Karato, S. (2008), *Deformation of Earth Materials: An Introduction to the Rheology of Solid Earth*, Cambridge University Press, Cambridge, UK.

Kaula, W. M. (1966), *Theory of satellite geodesy. Applications of satellites to geodesy*, Dover, Waltham, Mass.: Blaisdell, 1966.

Kaula, W. M. (1968), *An introduction to planetary physics - The terrestrial planets*, Space Science Text Series, New York: Wiley.

Konopliv, A. S., and C. F. Yoder (1996), Venusian k_2 tidal Love number from Magellan and PVO tracking data, *Geophys. Res. Lett.*, *23*, 1857–1860.

Konopliv, A. S., W. B. Banerdt, and W. L. Sjogren (1999), Venus Gravity: 180th Degree and Order Model, *Icarus*, *139*, 3–18.

Konopliv, A. S., S. W. Asmar, W. M. Folkner, Ö. Karatekin, D. C. Nunes, S. E. Smrekar, C. F. Yoder, and M. T. Zuber (2011), Mars high resolution gravity fields from MRO, Mars seasonal gravity, and other dynamical parameters, *Icarus*, *211*, 401–428, doi:10.1016/j.icarus.2010.10.004.

Konopliv, A. S., R. S. Park, D.-N. Yuan, S. W. Asmar, M. M. Watkins, J. G. Williams, E. Fahnestock, G. Kruizinga, M. Paik, D. Strekalov, N. Harvey, D. E.

Smith, and M. T. Zuber (2013a), The JPL lunar gravity field to spherical harmonic degree 660 from the GRAIL Primary Mission, *J. Geophys. Res. Planets*, *118*, 1415–1434, doi:10.1002/jgre.20097.

Konopliv, A. S., R. S. Park, D.-N. Yuan, S. W. Asmar, M. M. Watkins, J. G. Williams, E. Fahnestock, G. Kruizinga, M. Paik, D. Strekalov, N. Harvey, D. E. Smith, and M. T. Zuber (2013b), The JPL lunar gravity field to spherical harmonic degree 660 from the GRAIL Primary Mission, *J. Geophys. Res. Planets*, *118*, 1415–1434, doi:10.1002/jgre.20097.

Lambeck, K. (1988), *Geophysical Geodesy: the Slow Deformations of the Earth*, Oxford science publications, Clarendon Press.

Lemoine, F. G., S. Goossens, T. J. Sabaka, J. B. Nicholas, E. Mazarico, D. D. Rowlands, B. D. Loomis, D. S. Chinn, D. S. Caprette, G. A. Neumann, D. E. Smith, and M. T. Zuber (2013), High-degree gravity models from GRAIL primary mission data, *J. Geophys. Res. Planets*, *118*, 1676–1698, doi: 10.1002/jgre.20118.

LePage, W. R. (1980), *Complex Variables and the Laplace Transform for Engineers*, Dover Books on Electrical Engineering Series, Dover Publications.

Love, A. E. H. (1911), *Some Problems of Geodynamics*, Cambridge University Press.

Love, A. E. H. (1927), *A Treatise on the Mathematical Theory of Elasticity*, Dover reprint, 1944 ed., Cambridge University Press, Cambridge.

Lyubetskaya, T., and J. Korenaga (2007), Chemical composition of Earth's primitive mantle and its variance: 1. Method and results, *J. Geophys. Res. Sol. Ea.*, *112*, B03211, doi:10.1029/2005JB004223.

Malavergne, V., M. J. Toplis, S. Berthet, and J. Jones (2010), Highly reducing conditions during core formation on Mercury: Implications for internal structure and the origin of a magnetic field, *Icarus*, *206*, 199–209, doi: 10.1016/j.icarus.2009.09.001.

Malavergne, V., P. Cordier, K. Righter, F. Brunet, B. Zanda, A. Addad, T. Smith, H. Bureau, S. Surblé, C. Raepsaet, E. Charon, and R. H. Hewins (2014), How Mercury can be the most reduced terrestrial planet and still store iron in its mantle, *Earth Planet. Sc. Lett.*, *394*, 186–197, doi:10.1016/j.epsl.2014.03.028.

Malvern, L. (1969), *Introduction to the Mechanics of a Continuous Medium*, Prentice-Hall series in engineering of the physical sciences, Prentice-Hall.

Margot, J. L., S. J. Peale, R. F. Jurgens, M. A. Slade, and I. V. Holin (2007), Large longitude libration of Mercury reveals a molten core, *Science*, *316*, 710–714, doi:10.1126/science.1140514.

Margot, J.-L., S. J. Peale, S. C. Solomon, S. A. Hauck, II, F. D. Ghigo, R. F. Jurgens, M. Yseboodt, J. D. Giorgini, S. Padovan, and D. B. Campbell (2012), Mercury's moment of inertia from spin and gravity data, *J. Geophys. Res.*, *117*, E00L09, doi:10.1029/2012JE004161.

Mazarico, E., A. Genova, S. J. Goossens, F. G. Lemoine, G. A. Neumann, M. T. Zuber, D. E. Smith, and S. C. Solomon (2014a), The gravity field, orientation, and ephemeris of Mercury from MESSENGER observations after 3 years in orbit, *J. Geophys. Res. Planets*, doi:10.1002/2014JE004675, in press.

Mazarico, E., A. Genova, S. J. Goossens, F. G. Lemoine, G. A. Neumann, M. T. Zuber, D. E. Smith, and S. C. Solomon (2014b), The gravity field of Mercury from MESSENGER, *Lunar Planet. Sci., 45*, abstract 1863.

McCoy, T. J., T. L. Dickinson, and G. E. Lofgren (1999), Partial melting of the Indarch (EH4) meteorite: A textural, chemical and phase relations view of melting and melt migration, *Meteorit. Planet. Sci.*, *34*, 735–746, doi:10.1111/j.1945-5100.1999.tb01386.x.

McDonough, W. F., and S. S. Sun (1995), The composition of the earth, *Chem. Geol.*, *120*, 223 – 253, doi:http://dx.doi.org/10.1016/0009-2541(94)00140-4.

Melosh, H. J., A. M. Freed, B. C. Johnson, D. M. Blair, J. C. Andrews-Hanna, G. A. Neumann, R. J. Phillips, D. E. Smith, S. C. Solomon, M. A. Wieczorek, and M. T. Zuber (2013), The Origin of Lunar Mascon Basins, *Science*, *340*, 1552–1555, doi:10.1126/science.1235768.

Michel, N. C., S. A. Hauck, II, S. C. Solomon, R. J. Phillips, J. H. Roberts, and M. T. Zuber (2013), Thermal evolution of Mercury as constrained by MESSENGER observations, *J. Geophys. Res. Planets*, doi:10.1002/jgre.20049, inpress.

Milani, A., A. Rossi, D. Vokrouhlický, D. Villani, and C. Bonanno (2001), Gravity field and rotation state of Mercury from the BepiColombo Radio Science Experiments, *Planet. Space Sci.*, *49*, 1579–1596, doi:10.1016/S0032-0633(01)00095-2.

Miljković, K., M. A. Wieczorek, G. S. Collins, M. Laneuville, G. A. Neumann, H. J. Melosh, S. C. Solomon, R. J. Phillips, D. E. Smith, and M. T. Zuber (2013), Asymmetric distribution of lunar impact basins caused by variations in target properties, *Science*, *342*, 724–726, doi:10.1126/science.1243224.

Miljković, K., M. A. Wieczorek, G. S. Collins, S. C. Solomon, D. E. Smith, and M. T. Zuber (2015), Excavation of the lunar mantle by basin-forming impact events on the Moon, *Earth Planet. Sci. Lett.*, *409*, 243–251, doi:10.1016/j.epsl.2014.10.041.

Moore, W. B., and G. Schubert (2000), Note: The tidal response of Europa, *Icarus*, *147*, 317–319, doi:10.1006/icar.2000.6460.

Morgan, J. W., and E. Anders (1980), Chemical composition of Earth, Venus, and Mercury, *Proc. Nat. Acad. Sci.*, *77*, 6973–6977, doi:10.1073/pnas.77.12.6973.

Murray, C. D., and S. F. Dermott (1999), *Solar System Dynamics*, Cambridge University Press.

Neumann, G. A. (2014), Spherical harmonic expansion for the topography of Mercury, `GTMES_120V02_SHA`, NASA Planetary Data System.

Nimmo, F. (2002), Constraining the crustal thickness on Mercury from viscous topographic relaxation, *Geophys. Res. Lett.*, *29*, 1063, doi:10.1029/2001GL013883.

Nimmo, F., and U. H. Faul (2013), Dissipation at tidal and seismic frequencies in a melt-free, anhydrous Mars, *J. Geophys. Res. Planets*, *118*, 2558–2569, doi:10.1002/2013JE004499.

Nimmo, F., and T. R. Watters (2004), Depth of faulting on Mercury: Implications for heat flux and crustal and effective elastic thickness, *Geophys. Res. Lett.*, *31*, L02701, doi:10.1029/2003GL018847.

Nimmo, F., U. H. Faul, and E. J. Garnero (2012), Dissipation at tidal and seismic frequencies in a melt-free Moon, *J. Geophys. Res. Planets*, *117*, E09005, doi:10.1029/2012JE004160.

Nittler, L. R., R. D. Starr, S. Z. Weider, T. J. McCoy, W. V. Boynton, D. S. Ebel, C. M. Ernst, L. G. Evans, J. O. Goldsten, D. K. Hamara, D. J. Lawrence, R. L. McNutt Jr., C. E. Schlemm, S. C. Solomon, and A. L. Sprague (2011),

The major-element composition of Mercury's surface from MESSENGER X-ray spectrometry, *Science*, *333*, 1847–1850, doi:10.1126/science.1211567.

Padovan, S., J.-L. Margot, S. A. Hauck, W. B. Moore, and S. C. Solomon (2014a), The tides of Mercury and possible implications for its interior structure, *J. Geophys. Res. Planets*, *119*, 850–866, doi:10.1002/2013JE004459.

Padovan, S., M. A. Wieczorek, J.-L. Margot, N. Tosi, and S. C. Solomon (2014b), Thickness of the crust of Mercury from geoid-to-topography ratios, *Geophys. Res. Lett.*, under revision.

Peale, S. J. (1969), Generalized Cassini's laws, *Astron. J.*, *74*, 483–489, doi:10.1086/110825.

Peale, S. J. (1976), Does Mercury have a molten core?, *Nature*, *262*, 765–766, doi:10.1038/262765a0.

Peltier, W. R. (1974), The impulse response of a Maxwell earth., *Rev. Geophys. Space Phys.*, *12*, 649–669, doi:10.1029/RG012i004p00649.

Peplowski, P. N., L. G. Evans, S. A. Hauck II, T. J. McCoy, W. V. Boynton, J. J. Gillis-Davis, D. S. Ebel, J. O. Goldsten, D. K. Hamara, D. J. Lawrence, R. L. McNutt Jr., L. R. Nittler, S. C. Solomon, E. A. Rhodes, A. L. Sprague, R. D. Starr, and K. R. Stockstill-Cahill (2011), Radioactive elements on Mercury's surface from MESSENGER: Implications for the planet's formation and evolution, *Science*, *333*, 1850–1852, doi:10.1126/science.1211576.

Peplowski, P. N., D. J. Lawrence, E. A. Rhodes, A. L. Sprague, T. J. McCoy, B. W. Denevi, L. G. Evans, J. W. Head, L. R. Nittler, S. C. Solomon, K. R. Stockstill-Cahill, and S. Z. Weider (2012), Variations in the abundances of

potassium and thorium on the surface of Mercury: Results from the MESSENGER Gamma-Ray Spectrometer, *J. Geophys. Res.*, *117*, E00L04, doi: 10.1029/2012JE004141.

Petit, G. and Luzum, B. (2010), IERS Conventions (2010), *Tech. rep.*, Frankfurt am Main: Verlag des Bundesamts für Kartographie und Geodäsie.

Pettengill, G. H., and R. B. Dyce (1965), A Radar Determination of the Rotation of the Planet Mercury, *Nature*, *206*, 1240, doi:10.1038/2061240a0.

Phillips, R. J., C. L. Johnson, M. E. Perry, S. A. Hauck, P. B. James, E. Mazarico, F. G. Lemoine, G. Neumann, S. J. Peale, M. A. Siegler, D. E. Smith, S. C. Solomon, and M. T. Zuber (2014), Mercury's 2nd-Degree Shape and Geoid: Lunar Comparisons and Thermal Anomalies, *Lunar Planet. Sci., 45*, abstract 2634.

Porco, C. C., P. Helfenstein, P. C. Thomas, A. P. Ingersoll, J. Wisdom, R. West, G. Neukum, T. Denk, R. Wagner, T. Roatsch, S. Kieffer, E. Turtle, A. McEwen, T. V. Johnson, J. Rathbun, J. Veverka, D. Wilson, J. Perry, J. Spitale, A. Brahic, J. A. Burns, A. D. Del Genio, L. Dones, C. D. Murray, and S. Squyres (2006), Cassini Observes the Active South Pole of Enceladus, *Science*, *311*, 1393–1401, doi:10.1126/science.1123013.

Ramsey, A. (1949), *An Introduction to the Theory of Newtonian Attraction*, The University Press.

Redmond, H. L., and S. D. King (2007), Does mantle convection currently exist on Mercury?, *Phys. Earth Planet. In.*, *164*, 221–231, doi:10.1016/j.pepi.2007.07.004.

Rivoldini, A., and T. Van Hoolst (2013), The interior structure of Mercury constrained by the low-degree gravity field and the rotation of Mercury, *Earth Planet. Sci. Lett.*, *377*, 62–72, doi:10.1016/j.epsl.2013.07.021.

Rivoldini, A., T. van Hoolst, and O. Verhoeven (2009), The interior structure of Mercury and its core sulfur content, *Icarus*, *201*, 12–30, doi:10.1016/j.icarus.2008.12.020.

Roberts, J. H., and O. S. Barnouin (2012), The effect of the Caloris impact on the mantle dynamics and volcanism of Mercury, *J. Geophys. Res. Planets*, *117*, E02007, doi:10.1029/2011JE003876.

Schubert, G., D. L. Turcotte, and P. Olson (2001), *Mantle Convection in the Earth and Planets*, Cambridge University Press, doi:10.1017/CBO9780511612879.

Schubert, G., J. D. Anderson, B. J. Travis, and J. Palguta (2007), Enceladus: Present internal structure and differentiation by early and long-term radiogenic heating, *Icaurs*, *188*, 345–355, doi:10.1016/j.icarus.2006.12.012.

Segatz, M., T. Spohn, M. N. Ross, and G. Schubert (1988), Tidal dissipation, surface heat flow, and figure of viscoelastic models of Io, *Icarus*, *75*, 187–206, doi:10.1016/0019-1035(88)90001-2.

Siivola, J., and R. Schmid (2007), List of mineral abbreviations, Recommendations by the IUGS Subcommission on the Systematics of Metamorphic Rocks, *Electronic Source: http://www.bgs.ac.uk/scmr/docs/papers/paper_12.pdf.*

Smith, D. E., M. T. Zuber, R. J. Phillips, S. C. Solomon, S. A. Hauck, II, F. G. Lemoine, E. Mazarico, G. A. Neumann, S. J. Peale, J. L. Margot, C. L. Johnson, M. H. Torrence, M. E. Perry, D. D. Rowlands, S. Goossens, J. W.

Head, and A. H. Taylor (2012), Gravity field and internal structure of Mercury from MESSENGER, *Science*, *336*, 214–217, doi:10.1126/science.1218809.

Sobolev, S. V., and A. Y. Babeyko (1994), Modeling of mineralogical composition, density and elastic wave velocities in anhydrous magmatic rocks, *Surv. Geophys.*, *15*, 515–544, doi:10.1007/BF00690173.

Sohl, F., and T. Spohn (1997), The interior structure of Mars: Implications from SNC meteorites, *J. Geophys. Res.*, *102*, 1613–1636, doi:10.1029/96JE03419.

Soter, S., and J. Ulrichs (1967), Rotation and Heating of the Planet Mercury, *Nature*, *214*, 1315–1316, doi:10.1038/2141315a0.

Stockstill-Cahill, K. R., T. J. McCoy, L. R. Nittler, S. Z. Weider, and S. A. Hauck, II (2012), Magnesium-rich crustal compositions on Mercury: Implications for magmatism from petrologic modeling, *J. Geophys. Res.*, *117*, E00L15, doi:10.1029/2012JE004140.

Strom, R. G., N. J. Trask, and J. E. Guest (1975), Tectonism and volcanism on Mercury, *J. Geophys. Res.*, *80*, 2478–2507, doi:10.1029/JB080i017p02478.

Takeuchi, H., M. Saito, and N. Kobayashi (1962), Statical Deformations and Free Oscillations of a Model Earth, *J. Geophys. Res.*, *67*, 1141–1154, doi:10.1029/JZ067i003p01141.

Taylor, G. J., and E. R. D. Scott (2005), Mercury, in *Meteorites, Comets and Planets: Treatise on Geochemistry, Volume 1*, edited by A. M. Davis., pp. 477–485, Elsevier, Amsterdam, The Netherlands.

Tobie, G., A. Mocquet, and C. Sotin (2005), Tidal dissipation within large icy satellites: Applications to Europa and Titan, *Icarus*, *177*, 534–549, doi:10.1016/j.icarus.2005.04.006.

Tosi, N., M. Grott, A.-C. Plesa, and D. Breuer (2013), Thermochemical evolution of Mercury's interior, *J. Geophys. Res. Planets*, *118*, 2474–2487, doi:10.1002/jgre.20168.

Turcotte, D. L., and G. Schubert (2002), *Geodynamics*, 2nd ed., Cambridge University Press,Cambridge, UK, doi:10.2277/0521661862.

Turcotte, D. L., R. J. Willemann, W. F. Haxby, and J. Norberry (1981), Role of membrane stresses in the support of planetary topography, *J. Geophys. Res.*, *86*, 3951–3959, doi:10.1029/JB086iB05p03951.

Urakawa, S., K. Someya, H. Terasaki, T. Katsura, S. Yokoshi, K.-I. Funakoshi, W. Utsumi, Y. Katayama, Y.-I. Sueda, and T. Irifune (2004), Phase relationships and equations of state for FeS at high pressures and temperatures and implications for the internal structure of Mars, *Phys. Earth Planet. Inter.*, *143*, 469–479, doi:10.1016/j.pepi.2003.12.015.

Vacher, P., A. Mocquet, and C. Sotin (1998), Computation of seismic profiles from mineral physics: The importance of the non-olivine components for explaining the 660 km depth discontinuity, *Phys. Earth Planet. Inter.*, *106*, 277–300.

Van Hoolst, T., and C. Jacobs (2003), Mercury's tides and interior structure, *J. Geophys. Res.*, *108*, 5121, doi:10.1029/2003JE002126.

Van Hoolst, T., A. Rivoldini, R.-M. Baland, and M. Yseboodt (2012), The effect of tides and an inner core on the forced longitudinal libration of Mercury, *Earth Planet. Sci. Lett.*, *333*, 83–90, doi:10.1016/j.epsl.2012.04.014.

Verhoeven, O., A. Rivoldini, P. Vacher, A. Mocquet, G. Choblet, M. Menvielle, V. Dehant, T. Van Hoolst, J. Sleewaegen, J.-P. Barriot, and P. Lognonné (2005), Interior structure of terrestrial planets: Modeling Mars' mantle and

its electromagnetic, geodetic, and seismic properties, *J. Geophys. Res.*, *110*, E04/009, doi:10.1029/2004JE002271.

Wasson, J. T. (1988), The building stones of the planets, in *Mercury*, edited by F. Vilas, C. R. Chapman, and M. S. Matthews, pp. 622–650, University of Arizona Press, Tucson, Arizona.

Watt, J. P., G. F. Davies, and R. J. O'Connell (1976), The elastic properties of composite materials, *Rev. Geophys. Space Phys.*, *14*, 541–563, doi:10.1029/RG014i004p00541.

Watters, T. R., R. A. Schultz, M. S. Robinson, and A. C. Cook (2002), The mechanical and thermal structure of Mercury's early lithosphere, *Geophys. Res. Lett.*, *29*, 1542, doi:10.1029/2001GL014308.

Weber, R. C., P.-Y. Lin, E. J. Garnero, Q. Williams, and P. Lognonné (2011), Seismic detection of the lunar core, *Science*, *331*, 309–312, doi:10.1126/science.1199375.

Weider, S. Z., L. R. Nittler, R. D. Starr, T. J. McCoy, K. R. Stockstill-Cahill, P. K. Byrne, B. W. Denevi, J. W. Head, and S. C. Solomon (2012), Chemical heterogeneity on Mercury's surface revealed by the MESSENGER X-Ray Spectrometer, *J. Geophys. Res.*, *117*, E00L05, doi:10.1029/2012JE004153.

Wessel, P., and W. H. F. Smith (1991), Free software helps map and display data, *Eos Trans. AGU*, *72*, 441–446, doi:10.1029/90EO00319.

Wieczerkowski, K. (1999), Gravito-Viskoelastodynamik für verallgemeinerte Rheologien mit Anwendungen auf den Jupitermond Io und die Erde, Ph.D. thesis, Westfälischen Wilhelms-Universität Münster, Münster, Germany.

Wieczorek, M. A. (2007), Gravity and topography of the terrestrial planets, in *Treatise on Geophysics, Volume 10.*, edited by J. Schubert and T. Spohn, pp. 165–, Elsevier.

Wieczorek, M. A. (2014), SHTOOLS – Tools for working with spherical harmonics (v2.9.1), Zenodo, doi:10.5281/zenodo.12158.

Wieczorek, M. A. (2015), Gravity and topography of the terrestrial planets, in *Planets and Moons, edited by T. Spohn, Treatise on Geophysics, Vol. 10*, edited by J. Schubert, 2nd ed., Elsevier, Amsterdam, The Netherlands.

Wieczorek, M. A., and R. J. Phillips (1997), The structure and compensation of the lunar highland crust, *J. Geophys. Res.*, *102*, 10,933–10,944, doi:10.1029/97JE00666.

Wieczorek, M. A., and M. T. Zuber (2004), Thickness of the Martian crust: Improved constraints from geoid-to-topography ratios, *J. Geophys. Res. Planets*, *109*, E01009, doi:10.1029/2003JE002153.

Wieczorek, M. A., B. L. Jolliff, A. Khan, M. E. Pritchard, B. P. Weiss, J. G. Williams, L. L. Hood, K. Righter, C. R. Neal, C. K. Shearer, I. S. McCallum, S. Tompkins, B. R. Hawke, C. Peterson, J. J. GIllis, and B. Bussey (2006), The constitution and structure of the lunar interior, *Rev. Mineral. Geochem.*, *60*, 221–364, doi:10.2138/rmg.2006.60.3.

Wieczorek, M. A., A. C. M. Correia, M. Le Feuvre, J. Laskar, and N. Rambaux (2012), Mercury's spin-orbit resonance explained by initial retrograde and subsequent synchronous rotation, *Nature Geosci.*, *5*, 18–21, doi:10.1038/ngeo1350.

Wieczorek, M. A., G. A. Neumann, F. Nimmo, W. S. Kiefer, G. J. Taylor, H. J. Melosh, R. J. Phillips, S. C. Solomon, J. C. Andrews-Hanna, S. W. Asmar,

A. S. Konopliv, F. G. Lemoine, D. E. Smith, M. M. Watkins, J. G. Williams, and M. T. Zuber (2013), The Crust of the Moon as Seen by GRAIL, *Science*, *339*, 671–675, doi:10.1126/science.1231530.

Williams, J. G., A. S. Konopliv, D. H. Boggs, R. S. Park, D.-N. Yuan, F. G. Lemoine, S. Goossens, E. Mazarico, F. Nimmo, R. C. Weber, S. W. Asmar, H. J. Melosh, G. A. Neumann, R. J. Phillips, D. E. Smith, S. C. Solomon, M. M. Watkins, M. A. Wieczorek, J. C. Andrews-Hanna, J. W. Head, W. S. Kiefer, I. Matsuyama, P. J. McGovern, G. J. Taylor, and M. T. Zuber (2014), Lunar interior properties from the grail mission, *J. Geophys. Res. Planets*, doi:10.1002/2013JE004559.

Wolf, D. (1993), Gravitational viscoelastodynamics for a hydrostatic planet, http://elib.uni-stuttgart.de/opus/volltexte/2010/5095/pdf/wol24.pdf, Habilitationsschrift, Münster, Germany.

Wolf, D. (1994), Lame's problem of gravitational viscoelasticity - The isochemical, incompressible planet, *Geophys. J. Int.*, *116*, 321, doi:10.1111/j.1365-246X.1994.tb01801.x.

Yoder, C. F., A. S. Konopliv, D. N. Yuan, E. M. Standish, and W. M. Folkner (2003), Fluid core size of Mars from detection of the solar tide, *Science*, *300*, 299–303, doi:10.1126/science.1079645.

Zhao, Y.-H., M. E. Zimmerman, and D. L. Kohlstedt (2009), Effect of iron content on the creep behavior of olivine: 1. Anhydrous conditions, *Earth Planet. Sci. Lett.*, *287*, 229–240, doi:10.1016/j.epsl.2009.08.006.

Zolotov, M. Y., A. L. Sprague, S. A. Hauck, II, L. R. Nittler, S. C. Solomon, and S. Z. Weider (2013), The redox state, FeO content, and origin of sulfur-

rich magmas on Mercury, *J. Geophys. Res. Planets*, *118*, 138–146, doi:10.1029/2012JE004274.

Zuber, M. T., D. E. Smith, R. J. Phillips, S. C. Solomon, G. A. Neumann, S. A. Hauck, S. J. Peale, O. S. Barnouin, J. W. Head, C. L. Johnson, F. G. Lemoine, E. Mazarico, X. Sun, M. H. Torrence, A. M. Freed, C. Klimczak, J.-L. Margot, J. Oberst, M. E. Perry, R. L. McNutt, J. A. Balcerski, N. Michel, M. J. Talpe, and D. Yang (2012), Topography of the Northern Hemisphere of Mercury from MESSENGER Laser Altimetry, *Science*, *336*, 217–220, doi:10.1126/science.1218805.

Zuber, M. T., D. E. Smith, D. H. Lehman, T. L. Hoffman, S. W. Asmar, and M. M. Watkins (2013), Gravity Recovery and Interior Laboratory (GRAIL): Mapping the lunar interior from crust to core, *Space Sci. Rev.*, *178*, 3–24, doi:10.1007/s11214-012-9952-7.